6-28-2017

3-D Dynamic Analysis of High-Speed Railroad Track

Mohammad Fesharaki
mfesh001@fiu.edu

DOI: 10.25148/etd.FIDC001968

FLORIDA INTERNATIONAL UNIVERSITY

Miami, Florida

3-D DYNAMIC ANALYSIS OF HIGH-SPEED RAILROAD TRACK

A dissertation submitted in partial fulfillment of the
requirements for the degree of

DOCTOR OF PHILOSOPHY

in

CIVIL ENGINEERING

by

Mohammad Fesharaki

2017

To: Interim Dean Ranu Jung
College of Engineering and Computing

This dissertation, written by Mohammad Fesharaki, and entitled 3D Dynamic Analysis of High-Speed Railroad Track, having been approved in respect to style and intellectual content, is referred to you for judgment.

We have read this dissertation and recommend that it be approved.

_____
Atorod Azizinamini

_____
Ioannis Zisis

_____
Seung Jae Lee

_____
Ali Mostafavi

_____
Ton-Lo Wang, Major Professor

Date of Defense: June 28, 2017

The dissertation of Mohammad Fesharaki is approved.

_____
Interim Dean Ranu Jung
College of Engineering and Computing

_____
Andrés G. Gil
Vice President for Research and Economic Development
and Dean of the University Graduate School

Florida International University, 2017

ABSTRACT OF THE DISSERTATION

3D DYNAMIC ANALYSIS OF HIGH-SPEED RAILROAD TRACK

by

Mohammad Fesharaki

Florida International University, 2017

Miami, Florida

Professor Ton-Lo Wang, Major Professor

High-Speed Rail (HSR) as a fast, reliable and environmentally friendly mode of transportation has received a lot of attention in recent decades. The International Union of Railways reported that there are more than 18600 miles of HSR in operation and about 1.6 billion passengers per year are carried by them. Although there are plans for HSR in many states including Florida, the United States, however, is still hesitant to develop its own HSR network. One of the main barriers to developing high-speed rail is excessive vibration propagation to the media which may cause annoyance to people who live in the track neighborhood. Train induced vibration also contributes to track settlement, developing track flaws, and increasing life cycle cost of track and supporting structures.

The aim of this research is to address this problem by conducting a comprehensive investigation into track dynamics. For this purpose, three-dimensional mass-spring-damper models of vehicle, track and supporting structures were developed and matrices of mass, stiffness and damping of each subsystem were formed. The response of the whole system was, then, determined by coupling the subsystems using Hertz contact theory. The differential equations of the coupled system were solved by the Newmark integration method and the results including vertical and lateral displacements and forces were

presented in the time domain. Since the purpose of this dissertation is to quantify the effect of track and vehicle condition on vibration level, rail defects were also taken into account and rail random irregularities for vertical profile, Gauge, alignment and cross level (super elevation) were incorporated into a numerical solution. The results of the study show the effect of track and vehicle parameters on the response of the vehicle, track and substructures.

Since Florida and some other states in the United States are very prone to hurricanes, an investigation was conducted into the effect of wind speed on vehicle stability. For this purpose, a curved beam was modeled to consider the influence of track curvature, cant deficiency, wind speed and train speed simultaneously. The results from the study show the maximum allowable values of train speed and axle load for different wind speeds. The findings can be used to decide under what circumstances there is a risk of vehicle overturning and how to avoid it.

TABLE OF CONTENTS

CHAPTER PAGE

LIST OF TABLES

TABLE PAGE

LIST OF FIGURES

FIGURE PAGE

1. Introduction

This short chapter provides as an overview of the dissertation and its contents and demonstrates the current problem that this research will address, the objectives of the project and the necessity of doing the dissertation. The method employed to conduct this study and also the organization of the project are the last parts of this chapter.

1. 1. Problem statement

The recent worldwide demand for construction of high-speed rails and increase of axle loads and traffic volumes is evidence of a need for structural improvement or modification of the conventional railroad track system. This requires a better understanding of railroad track system behavior and then improvement of the current codes of practice. Despite considerable developments in understanding of the mechanical behavior of the track, there are still several areas in the railroad field which need further studies. Due to lack of such studies, there have been many examples of incidents and complaints in different countries (Straszak & Tuch 1977).

In recent years, after considerable increase in ground vibration from X2000 trains in Sweden, many researchers started to investigate high-speed rail vibration and the possibility of trains' instability. Hence, considerable research has been conducted to investigate the dynamics of the rail track subjected to moving load during the last two decades (Krylov 2001).

A large volume of papers have been written on analyzing track and ground vibrations utilizing methods ranging from mathematical analyses to finite element (FEM) and boundary element methods (BEM). Recently Connolly et al, reviewed more than 200 scientific papers on track dynamics, it is evident that since the dynamics of railway track

is a complicated problem, no model has been able to successfully address the vibration problem of high-speed tracks (Connolly et al. 2015). A review of literature also shows that some important aspects of the track dynamics are still overlooked. The effect of track geometry on vibration level and operation safety has not been sufficiently addressed in the literature and very little attention has also been paid to the parameters influencing train operation including track defects such as vertical and lateral inflection angles at rail gaps and track geometry such as curve parameters.

The importance of track system geometry necessitates more investigation into track system to reduce vibration level and improve train safety. A study at the University of Illinois at Urbana-Champaign shows that after broken rails, track geometry is the main reason for derailments of freight trains (Liu et al. 2012). Increasing train speed increases vulnerability of trains to track geometry flaws.

Track deficiencies also generate vibration over a wide range of frequencies and amplitudes. Large amplitude vibration can cause damage to track components such as cracking, settlement of foundations, destabilization of embankments, and damage to nearby structures. So probe into safer and more reliable track is of great importance.

In this research, the possibility of derailment and vibration amplification due to track geometric deficiencies will be discussed and recommendations will be made for different track conditions and train speeds.

1. 2. Research Objective

The objective of the research is to improve high-speed rail track systems to reduce vibration and increase operation safety. It is also the purpose of the research to find the maximum safe speed for different track conditions.

1. 3. Research Methodology

This research develops a 3D train and track model and investigates the effective parameters on track and train vibrations and safety. It encompasses the following stages;

- Development of a vehicle model using a mass-spring-damper model,
- Development of vertical and lateral rail irregularities using appropriate power spectral density functions,
- Development of track and bridge models,
- Coupling the subsystems as an interaction model,

1. 4. Structure of the dissertation

This research includes eight parts which describe the process of numerical modeling of vehicle and railroad track. This section briefly introduced each part and its purpose:

Chapter 2 investigates the current practice in railroad track analysis to choose the best method for solving the current problem. The method must be able to model vehicle and track both in vertical and lateral directions.

Chapter 3 shows the process of vehicle modeling. Rail vehicle is simulated using a 31-degree-of-freedom mass–spring–dashpot system including a car body, two bogies and four wheelsets. Vehicle response in both vertical and lateral directions are considered.

Chapter 4 covers the process of rail irregularities modeling. Four types of track irregularities i.e., vertical profile, alignment, cross level and gauge are considered and characterized by the one-sided Power Spectral Density (PSD) functions.

Chapter 5 discusses the modeling of track and bridge. Rail and bridge are modeled by Euler-Bernoulli beams and a series of mass-spring-dampers, representing the rail pad, sleepers, ballast, and embankment form the track system. To address dynamic interaction

between rail and vehicle, Hertz contact theory will be used.

Chapter 6 discusses the results obtained from chapter 5 and probes into the effect of rail flaws on track and vehicle response.

Chapter 7 shows the process of curved beam modeling and the effects of wind forces on lateral stability of rail vehicle.

Chapter 8 summarizes the result of the study and provides recommendations for future works.

2. Literature Review

The dynamic analysis of railroad track is a complicated problem with numerous degrees of freedom. A detailed analysis of track consists of interaction between different components of track's superstructure and substructure, as well as vehicle-track interaction. On the other hand, the magnitude of loading from vehicle depends on different factors including rail irregularities, subgrade quality, axle load and train speed. As a result, an accurate track and vehicle models and loading pattern that account for every excitation sources is still a challenge and there is no exact solution for analysis of railroad track. The approximate solutions can be achieved by idealizing loading, material properties and track-vehicle interaction. However, some acceptable results can be obtained from such models. The efforts that have been made to simulate track, vehicle and nearby structures can be mainly divided into two groups: numerical and analytical methods. This chapter discusses the different methods and solutions that have been used thus far for analysis of railroad track and introduces the methodology that will be utilized in this dissertation.

2. 1. Analytical solutions

To avoid complex formulations, analytical solutions usually simplify track structure as much as possible, as a result, analytical methods cannot be used for detailed analysis of track under different conditions. These methods are based on analysis of beam as rail on track foundation. In most studies, two types of beams have been modeled: Euler-Bernoulli beam for simple analyses neglecting shear deformations and Timoshenko beam to take into account shear deformations and rotational bending effects. In most cases, the track substructure are considered to be elastic.

2. 1. 1. Beam on Winkler Foundation

The most popular method of track analysis is called beam on elastic foundation. It was first proposed by Winkler in 1867 and later developed by Zimmermann in 1887 (Esveld 2001). As Figure 2.1 shows it is assumed that deflection at each point is a function of under rail pressure. Using free body diagram of the beam shown in Figure 2.1**,** differential equation of rail displacement can be written as follows

$$q dx + \frac{dD}{dx} dx = p(x) dx \qquad 2.1$$

In which "p(x)" is the contact pressure between sleeper and ballast in unit width. "D" is the shear force of an element.(Sadeghi 2009)

Assuming a linear relationship between p(x) and displacement of each point, i.e. $p(x) = u.y(x)$ and applying boundary conditions, one can obtain

$$y(x) = \frac{P\beta e^{-\beta x}}{2u}(\cos\beta x + \sin\beta x) \qquad 2.2$$

Where $\beta = \left(\frac{u}{4EI}\right)^{0.25}$ and "u" is coefficient of stiffness or elastic modulus of track bed.

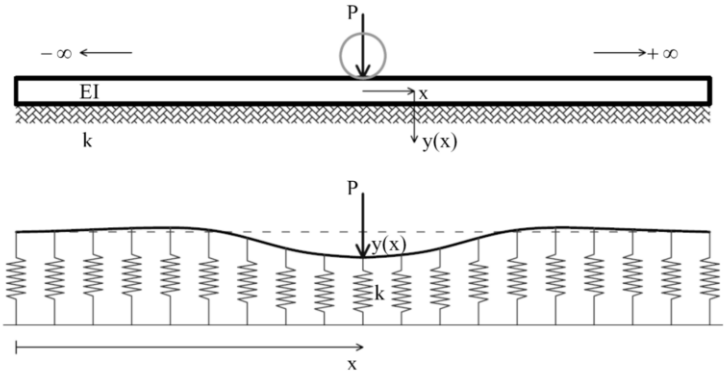

Figure 2.1 Beam on elastic foundation (Sadeghi 2009)

Although, beam on elastic foundation makes the solution easy by reasonable assumptions, however, this method has the following disadvantages

- The model does not consider ballast layer and rail supporting system. Track geometry including the effect of the distance between sleepers (cross ties), ballast depth and subgrade condition cannot be taken into account in the Winkler formulations.
- The longitudinal forces due to thermal stresses cannot be considered.
- Inertia and damping forces are not included in the model.

2. 1. 2. Beam on discrete support

To obtain Winkler's equations, track bed support was assumed to be continuous, but in real track, rail is supported in a certain distances (the distance between sleepers). Beam on discrete support model, considers rail supports only at the position of sleepers. The stiffness of each spring is equal to the stiffness of track. The solution was proposed by Boresi and Schmidt (2003) using Castigliano theorem (Boresi & Schmidt 2003). Kerr compared the method with Winkler solution and concluded that the results from both approaches are very close (Kerr 2003).

Kerr, also assuming rigid rail-tie connection and continuous moment at rail support, solve the following equations of motion

$$EI\frac{d^4y}{dx^4} - s\frac{d^2y}{dx^2} + ky = q \qquad 2.3$$

where "s" is a parameter show the relation between rail rotation and moment at rail support. "k_y" indicates the vertical pressure of rail support (Kerr 2003).

$$y(x) = \frac{P\beta e^{-\alpha|x|}}{2\alpha\kappa}(\kappa\cos(\beta|x|) + \alpha\sin(\kappa|x|)) \qquad 2.4$$

$$\alpha = \sqrt{\left(\beta^2 + \frac{s}{4EI}\right)} \text{ and } \kappa = \sqrt{-\left(\beta^2 - \frac{s}{4EI}\right)}$$

As the derived equation shows, rail displacement depends on track bed parameters “k” and “s” which can be determined from field measurements of rail displacements.

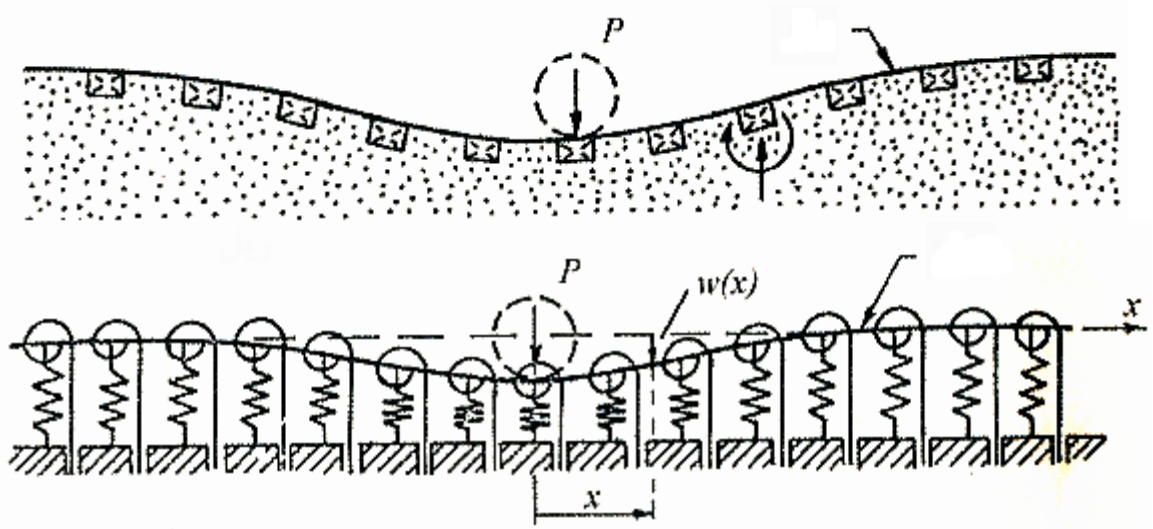

Figure 2.2 Analytical model including bending of rail support (up) physical problem (down) track model(Kerr 2003)

2. 1. 3. Pasternak foundation

Pasternak foundation can be considered as a modification to the beam on elastic foundation model. In this model, shear interaction between elastic supports have been taken into account. In other words, contrary to Winkler foundation, spring supports do not act independently. To incorporate shear effect on beam response, Pasternak used a vertical shear element between springs and rails. In the absence of external forces, free body diagram of Pasternak foundation is shown in Figure 2.3 (Esveld 2001).

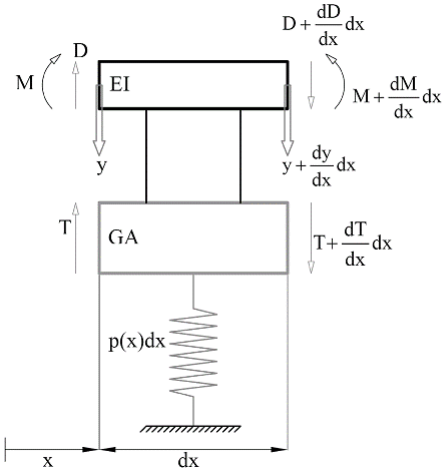

Figure 2.3 Free body diagram of Pasternak model (Sadeghi 2009)

The differential equation of vertical displacement of rail can be formulated as follows

$$EI\frac{d^4y}{dx^4} - GA\frac{d^2y}{dx^2} + ky = 0 \qquad 2.5$$

Applying a concentrated load "P" to rail, displacement and bending moment of rail can be calculated

$$y(x) = \frac{P}{8EIab\beta^2}e^{-bx}(a\cos ax + b\sin ax) \qquad 2.6$$

$$M(x) = \frac{P}{4ab}e^{-bx}(a\cos ax - b\sin ax) \qquad 2.7$$

where

$$a = \frac{1}{2}\sqrt{4\beta^2 - \gamma}$$

$$b = \frac{1}{2}\sqrt{4\beta^2 + \gamma}$$

$$\gamma = \frac{GA}{EI}$$

Kargarnovin and Younesian (Kargarnovin & Younesian 2004), using Hamilton principle, developed the Pasternak equations for Timoshenko beam under dynamic moving loads and

solved by complex Fourier transformation in conjunction with the residue and the convolution integral theorem. They found the deflections, bending moments, and shear forces along the beam length, as well as the effects of velocity and frequency variation of the load on the beam response.

Younesian and Kargarnovin (Younesian & Kargarnovin 2009) also investigated the response of the beams on random Pasternak foundations subjected to harmonic moving loads. Based on the results obtained from numerical analysis, the maximum deflection of a Timoshenko beam is larger than that of an Euler beam and inversely the maximum bending moment obtained from Timoshenko beam is lower than that of Euler-Bernoulli beam.

2. 1. 4. Double beam model

Although beam on elastic foundation and similar models successfully provide a good approximation of track response to train loads, in some cases more detailed models are required. Slab track as an alternative to conventional ballasted track is a well-known example of double beam model application. As Figure 2.4 demonstrates, this model consists of two beams: upper beam represents rail and lower beam shows track substructure such as slab or bridge. Many researchers analyzed slab track using this model. Hussein and Hunt (Hussein & Hunt 2006), employing this model, considered the effect of floating slab on vibration attenuation and identified the critical load velocity using the direct solution of the dispersion equation.

Kuo et al (Kuo et al. 2008) used double beam model to analyze the vehicle-track interaction problem under dynamic loads. They concluded that the rail deflections increase significantly as train speed increases. Although large slab mass may lower tuning

frequency, it could also result in higher wheel–rail contact forces and rail deflections. Correlation between wheel–rail resonance and train speed was also discussed in the paper.

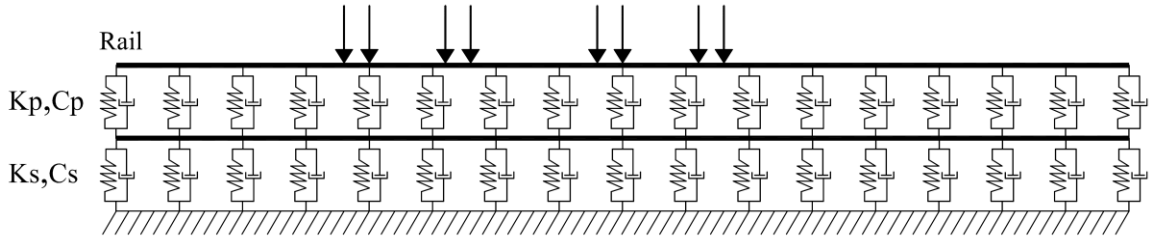

Figure 2.4 Double beam model

Another example of double beam modeling is presented by Lombaert (Lombaert et al. 2006) which investigated the effect of double beam track on far field vibrations.

The differential equations of Euler-Bernoulli double-beam model in case oscillating moving loads have the following form

$$\begin{aligned} &EI_r \frac{\partial^4 \mathrm{w_r}(x,t)}{\partial x^4} + m_r \frac{\partial^2 \mathrm{w_r}(x,t)}{\partial t^2} + k_p\left(\mathrm{w_r}(x,t) - \mathrm{w_s}(x,t)\right) + c_p\left(\frac{\partial \mathrm{w_r}(x,t)}{\partial t} - \frac{\partial \mathrm{w_s}(x,t)}{\partial t}\right) = P_0 \exp(i\bar{\omega}t)\delta(x - vt) \\ &EI_s \frac{\partial^4 \mathrm{w_s}(x,t)}{\partial x^4} + m_s \frac{\partial^2 \mathrm{w_s}(x,t)}{\partial t^2} + k_p\left(\mathrm{w_s}(x,t) - \mathrm{w_r}(x,t)\right) + k_s \mathrm{w_s}(x,t) + c_s \frac{\partial \mathrm{w_s}(x,t)}{\partial t} - c_p\left(\frac{\partial \mathrm{w_r}(x,t)}{\partial t} - \frac{\partial \mathrm{w_s}(x,t)}{\partial t}\right) = 0 \end{aligned} \quad 2.8$$

Where"$\delta(x - vt)$" is Dirac delta function and "$\mathrm{w_r}(x,t)$"and "$\mathrm{w_s}(x,t)$" indicate rail and slab displacements. "c_s" and "k_s"are also damping and stiffness of slab, respectively. An easy way to solve the above differential equations is to use Fourier transform. In other words, the problem should be transformed from time-space domain to wavenumber-frequency domain.

Double Fourier transform results in

$$\begin{aligned} &EI_r\zeta^4\tilde{w}_r - m_r\omega^2\tilde{w}_r + k_p\left(\tilde{w}_r - \tilde{w}_s\right) + c_p i\omega\left(\tilde{w}_r - \tilde{w}_s\right) = 2\pi\delta\left(\omega + \zeta v - \tilde{\omega}\right) \\ &EI_s\zeta^4\tilde{w}_s - m_s\omega^2\tilde{w}_s - k_p\left(\tilde{w}_r - \tilde{w}_s\right) - c_p i\omega\left(\tilde{w}_r - \tilde{w}_s\right) + k_s\tilde{w}_s + c_s i\omega\tilde{w}_s = 0 \end{aligned} \quad 2.9$$

The solution in time-space domain can be demonstrated in the following form

$$w_r(x,t)=\frac{\exp(i\bar{\omega}t)}{2\pi}\int_{-\infty}^{\infty}\frac{f_2(\zeta,\omega=\bar{\omega}-\zeta v)}{f_1(\zeta,\omega=\bar{\omega}-\zeta v)}\exp(i\zeta(x-vt))d\zeta \qquad 2.10$$

$$w_s(x,t)=\frac{\exp(i\bar{\omega}t)}{2\pi}\int_{-\infty}^{\infty}\frac{f_3(\zeta,\omega=\bar{\omega}-\zeta v)}{f_1(\zeta,\omega=\bar{\omega}-\zeta v)}\exp(i\zeta(x-vt))d\zeta \qquad 2.11$$

Where $f_1(\zeta,\omega)=|A|$, $f_2(\zeta,\omega)=EI_s\zeta^4-m_s\omega^2+k_p+k_s+i\omega(c_p-c_s)$ and $f_3(\zeta,\omega)=k_p+c_p i\omega$

"$|A|$" is the determinant of matrix "A". "$\tilde{w}_r$" and "$\tilde{w}_s$"are transformed displacement of rail and slab in wavenumber-frequency domain.

2. 1. 5. Other solutions

Fryba (Frýba 1999) in his book, " Vibration of Solids and Structures under Moving Loads" reviewed a number of mass-spring-damper models and presented solutions for different conditions. Table 2.1 shows a summary of these models. Incorporating vehicle into dynamic equations of motion makes the solution fairly difficult. For example, for a beam under moving vehicle with two degrees of freedom the following differential equation applies

$$EI_r\frac{\partial^4 w(x,t)}{\partial x^4}+m_r\frac{\partial^2 w(x,t)}{\partial t^2}+2\mu\omega_b\left(\frac{\partial w(x,t)}{\partial t}\right)=\delta(x-vt)\left[P-m_r\frac{\partial^2 w(x,t)}{\partial t^2}\right] \qquad 2.12$$

The second derivative on the right-hand side of equation makes the solution difficult compared to "moving loads" models. The complexity of problem increases with using more elaborate models in Table 2.1. In this case, where detailed analysis of rail or vehicle is necessary, numerical solution should be used instead.

2. 2. Numerical methods

Although analytical solutions can successfully predict the response of 2D track models, they are not reliable methods for problems including multi-body vehicles, track irregularities and train and track lateral stability analysis. To overcome these limitations

and analyze more realistic models including wheelflat, track irregularities, rail joints defects, track settlement, and ballast-slab transition zone, numerical methods have been utilized. There are several numerical approaches to track analysis including finite element method, boundary element method, and finite difference method which are briefly described.

2. 2. 1. Finite Element method

Finite Element Method (FEM) is the most popular numerical method for track analysis. Depending on the required level of complexity, a wide range of FE models have been developed. The basic FE model consists of Euler-Bernoulli beam on elastic foundation. Beam is modeled by Hermitian shape functions with two Degrees of Freedom (DOF) at each node of the beam elements (Lou & Zeng 2006).

The track components such as rail pads, sleepers (cross ties), ballast, subballast and subgrade have been modeled by mass-spring-dashpot systems. The number of sub-track layers depends on the purpose of analysis. If rail or vehicle response is of interest, the track sublayers can be reduces to one or two. (Lou et al. 2006), (Lou & Zeng 2005), but in case of substructure analysis a detail modeling of track components is usually required (Esmaeili et al. 2014).

Numerous studies have been conducted on track flaws using FE method. (Lei & Noda 2002), (Sun & Dhanasekar 2002), (Zhai et al. 2004).

Table 2.1 Track and vehicle models(Frýba 1999)

Model description	figure
Beam subjected to a moving system with 2 DOF	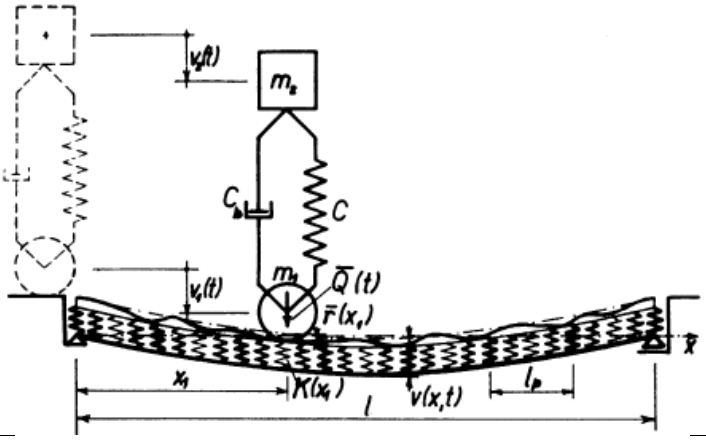
Beam subjected to a moving two-axle system	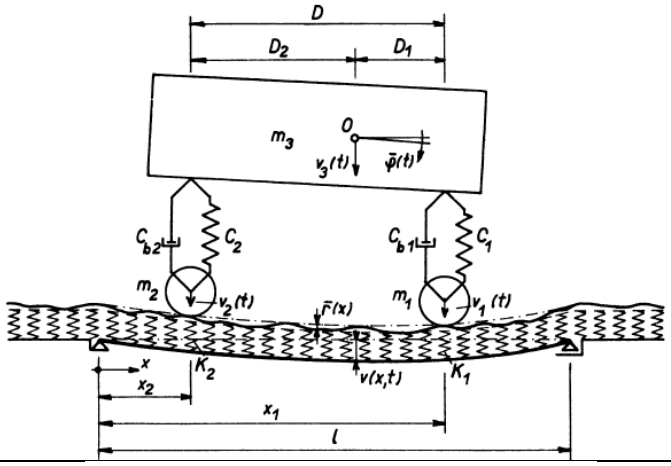
Beam subjected to a moving multi-axle system	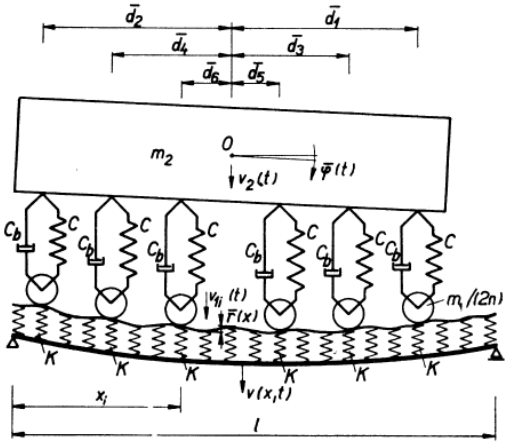

Most of the above-mentioned investigations considered a multi-body vehicle for vehicle-track interactions. There are generally two different ways to approach the interaction problems: first, it is assumed that wheels and rail are always in contact, (Lou et al. 2006), (Lei & Noda 2002) and second, the models consider the displacement between rail and wheels. The most famous model to include wheel-rail interaction in modeling is Hertz theory. Based on the shape and elastic properties of wheel and rail, the stiffness constant between rail and wheel can be determined (Esveld 2001). Other investigations proposed numerical methods to take into account friction force and creepage between wheel and rail (Zhao & Li 2011).

As Figure 2.5 shows vehicle models vary from a simple moving load to detailed 3D models. The first attempt to include the vehicle in track analysis was made by Winkler using single moving mass on Euler-Bernoulli beam. More realistic vehicle models were then used by introducing the multiple moving mass. The models, including car body bogie frames and wheelsets, are very popular for vehicle-track interaction analysis. In order to consider lateral response of track and vehicle, three-dimensional models of vehicles developed. These models are able to successfully simulate the unsymmetrical flaws, lateral rail irregularities and vehicle stability.

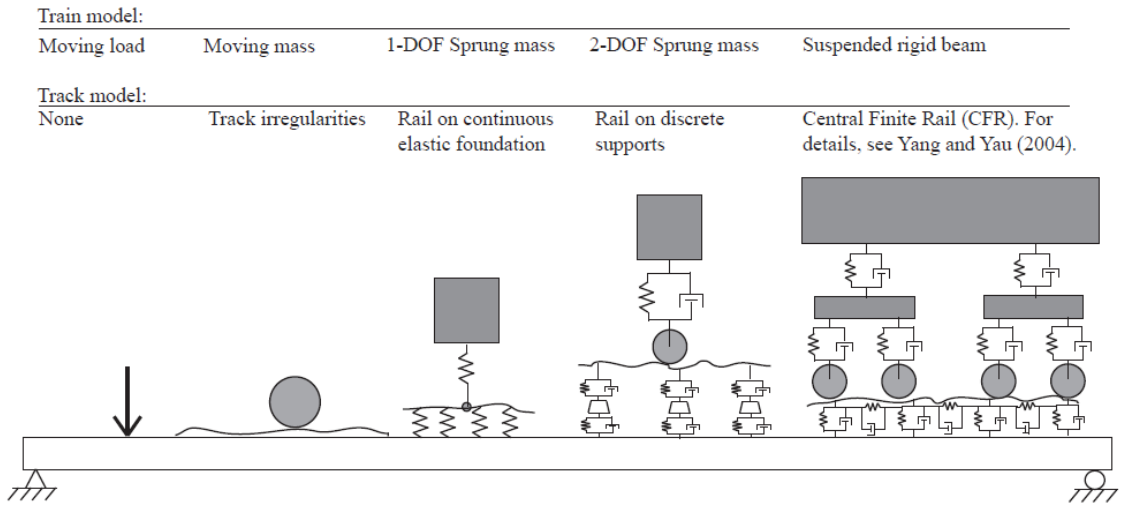

Figure 2.5 Evolution of railway vehicle models(Johansson 2013)

To investigate wave propagation to surrounding structures a number of three-dimensional FE models developed. These models mainly focus on track bed and consider wave propagation in the soil. As a result, the vibration level in far-field can be investigated. This approach can be used either by commercial FE codes such as ABAQUS (Hall 2003) or using theory of wave propagation in half-space (Krylov 1995), (Steenbergen & Metrikine 2007). The object of such analyses is usually to investigate the response of track to high-speed vehicles traveling faster than Rayleigh wave velocity in the subsoil. In this case, it is shown that high vibration level is expected. Figure 2.6 shows the effect of train traveling at the speed exceeding Rayleigh wave velocity on subsoil vibrations. The effect of embankment, ground geometry, and trench geometry were also investigated by some researchers. (Fu & Zheng 2014) , (Younesian & Sadri 2012).

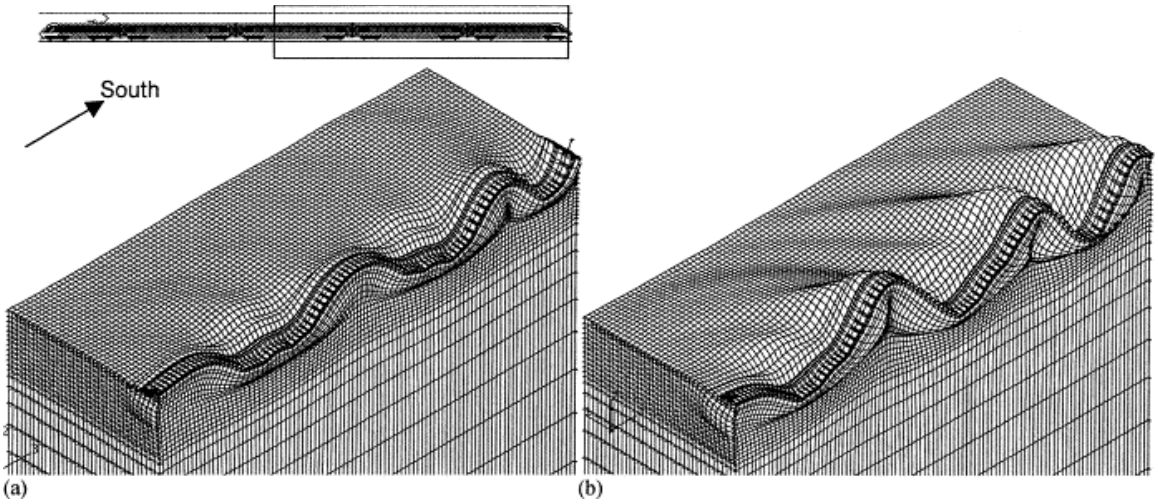

Figure 2.6 Deformed mesh from finite element analyses for different train speeds (a) 142 km/h and (b) 204 km/h (Hall 2003)

2. 2. 2. Boundary Element Method

Finite Element method is widely used in analysis of railroad track vibration. The matrices produced by FE analysis are symmetric, banded and positive definite and consequently programming this method is straightforward. However, in case of railroad track or other problems involving infinite boundaries, classical FE procedures cannot accurately simulate the infinite boundaries and treatments are required. As reported by Rizos and Wang (Rizos & Wang 2002), to solve this problem, many types of radiating, transmitting or absorbing elements have been developed. For example, as it is used by some FE codes such as ABAQUS, during dynamic steps, the infinite elements introduce additional normal and shear tractions on the finite element boundaries that are proportional to the normal and shear components at the boundary. These boundary damping constants are chosen to minimize the reflection of dilatational and shear wave energy back into the finite element mesh (Dassault Systèmes Simulia Corp 2012).

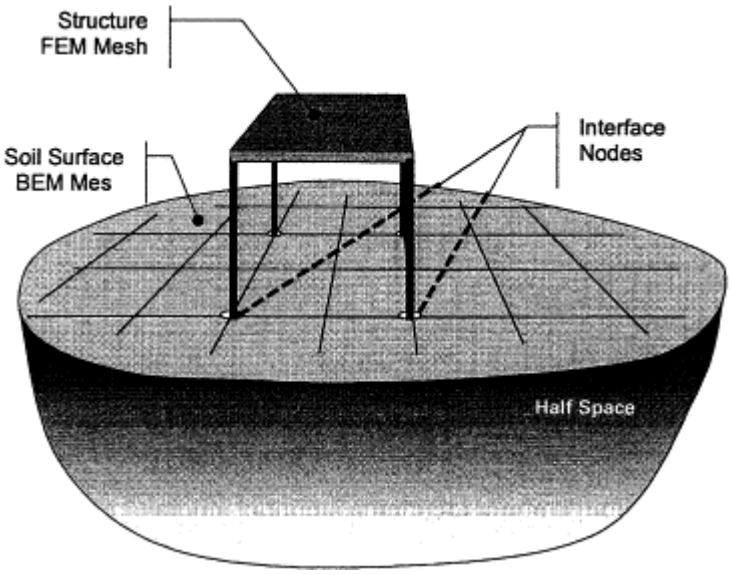

Figure 2.7 Finite Element and Boundary Element domains (Rizos & Wang 2002)

An alternative solution, is Boundary Element Method (BEM) where the radiation and wave propagation from boundary is considered in the associated Boundary Integral Equations (Brien & Rizos 2005). Another popular approach is FEM-BEM approach that uses the advantages of both methods and avoids the shortcomings of selecting one procedure. For example, O'Brien and Rizos (Brien & Rizos 2005) used BEM for the modeling of the soil-tie system within the framework of impulse response techniques and the FEM for modeling the rail system then the two methods was coupled at the tie-rail interface.

This approach has been used to model track and surrounding media for underground railways. Andersen and Jones (Andersen & Jones 2006), using coupled boundary and finite element method analyzed vibration from railway tunnels. They also compared two and three-dimensional models and recommended 2D or 3D analysis for different conditions. Vasilev et al (Vasilev et al. 2015) used the same approach to investigate soil-structure interaction using coupled BEM–FEM through finite element software ANSYS.

2. 2. 3. Finite Difference Method

Finite Difference Method (FDM) is an alternative to FEM used by some researchers. Based on the results of the study by Katou et al. (Katou et al. 2008), FDM has some advantages over FEM. They concluded that FDM programing are quite simple, and the FDM performs much faster and with lower memory usage compared to FEM. FDM has been utilized to find ground vibrations from wheel forces of high-speed trains, (Katou et al. 2008) and to predict ground-borne and structure-radiated noise from railroad track (Thornely-Taylor 2004).

2. 3. Other methods

Although FEM and BEM can model almost every geometry, discontinuity and boundary conditions, but in some cases, it would be easier and more accurate to use semi empirical or empirical approaches especially where the geometry of the model becomes too complicated or some hard-to-model components such as ground water should be included in the simulation. Hence, some researchers tried to develop other approaches to investigate track and surrounding structures.

2. 3. 1. Pipe-in-pipe models

The Pipe-in-Pipe (PiP) is a software package developed by Mohammed Hussein and Hugh Hunt at University of Cambridge. It is a semi-analytical three-dimensional model that accounts for the dynamic interaction between the track, the tunnel and the soil. As shown in Figure 2.8, the continuum theory of elasticity in cylindrical coordinates is used to model two concentric pipes: an inner pipe to represent the tunnel wall and an outer pipe to represent the surrounding soil. The tunnel and soil are coupled accounting for equilibrium of stresses and compatibility of displacements at the tunnel–soil interface. This method

assumes that the tunnel is invariant in the longitudinal direction and the problem is formulated in the frequency–wavenumber domain using a Fourier transformation. A track, formulated as an Euler–Bernoulli beam, is then coupled to this model. Results can be transformed to the space domain using the inverse Fourier transform.(Gupta et al. 2007)

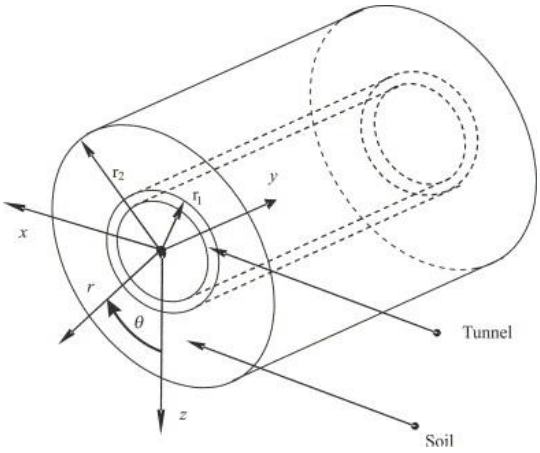

Figure 2.8 The PiP model (Gupta et al. 2007)

2. 3. 2. Empirical approach

Concern for excessive noise and vibration from trains has led to developing vibration assessment studies which are either preliminary or detailed. The purpose is to estimate track and nearby structures response due to passage of trains with different configurations. Federal Transit Administration (FTA), considering the previous studies conducted in different countries, quantified human response to ground-borne vibration and then developed some Adjustment Factors for predictions of vibration from track. Based on the type of track and vehicle, track defects, vehicle speed and geologic conditions, the response of track and neighboring structure can be determined. (Carl E. Hanson; David A. Towers; and Lance D. Meister 2006)

Other studies also developed preliminary or scoping vibration assessments. For example, Connolly et al. (Connolly et al. 2014) emphasizing on soil conditions, developed an initial

assessment prediction tool for high speed lines. The model developed by simulating track using three-dimensional FE analysis. A Neural Network (NN) approach was then used to establish relationships between key track parameters. The accuracy of the model was tested against the field measurements from high-speed track test results.

2. 4. Current approach

As it is discussed, many different approaches have been used to analyze track response to moving loads ranging from beam on Winkler foundation to complicated three dimensional vehicle-track interaction models. Choosing the most efficient method depends on the purpose of the analysis and the required level of precision. In some cases, a combination of different solutions produces more accurate results and makes the analysis easier.

The aim of this research is to gain a better understanding of track behavior under high-speed train loading and delve into track defects and their tolerance to guarantee the smooth traveling of vehicles. This dissertation also investigates the effect of curved beam and lateral loadings on the train stability. As a result, the model must be capable of the modeling of train, track and their interaction. Both vertical and lateral loadings are of interest and track components including sleepers and ballast should be modeled. To take into account the damping effect of vehicle, it should have the primary and secondary suspension systems.

The requirements of such model to get satisfactory results dictates using a three dimensional vehicle and track simulation. A mass-spring-damper model can be successfully employed to model such system. It would also be more convenient to solve the governing differential equations using finite element method. So, the process of solving the vehicle-track differential equations of motion is to form the matrices of mass, stiffness

and damping of the coupled system and then to apply sources of excitation including rail irregularities and wind forces. The response of the whole system can be determined by solving the differential equations employing the Newmark integration method in time domain.

3. Vehicle Model

3. 1. Introduction

The early models, developed to analyze railroad track, considered the vehicle as a series of concentrated loads. Although, these models were successful to predict track response for ideal situations, more complicated "real" track and vehicle conditions could not be modeled by such idealizations. Moreover, in such models, the interaction between track and the moving vehicle is ignored. For this reasons, moving load model produces acceptable results only where the mass of train is small compared to that of the track substructure. In other cases, where vehicle response is of interest or track defects considerably affect the vehicle-track interaction forces, more elaborate models are required. To address this issue, different vehicle models have been proposed. The simplest one is moving mass model which is able to take into account vehicle inertia. Akin and Mofid (1989) solved the problem for different boundary conditions by analytical-numerical approach (Akin & Mofid 1989).

While moving on track with irregularities, the bouncing effect of vehicle must be considered to accurately calculate track response especially for high-speed trains. Hence, the vehicle models have been further improved by considering the effects of the suspension systems. This has been done by modeling moving mass supported by a spring-dashpot unit, the so-called sprung mass model (Biggs 1964), (Pesterev, A. V., Yang, B., Bergman, L. A., and Tan 2001). The more advanced models apply the properties of different components of vehicle proposed by different researchers. Depending on the required level of precision, two and three dimensional vehicle models developed (Wang et al. 1991), (Zhang et al. 2001). Figure 3.1 shows a three dimensional model for analysis of railway-bridge interaction proposed by Wang et al (Wang et al. 1991).

In this study, the lateral and vertical response of track to high-speed train loading is investigated. As a part of study, the influence of track defects such as rail irregularities on track impact factors and stability of train under different conditions will be examined. As a results, a three dimensional model which is able to simulate motions and rotations in different directions is required. The model should be able to simulate primary and secondary suspension system and wheel-rail interactions.

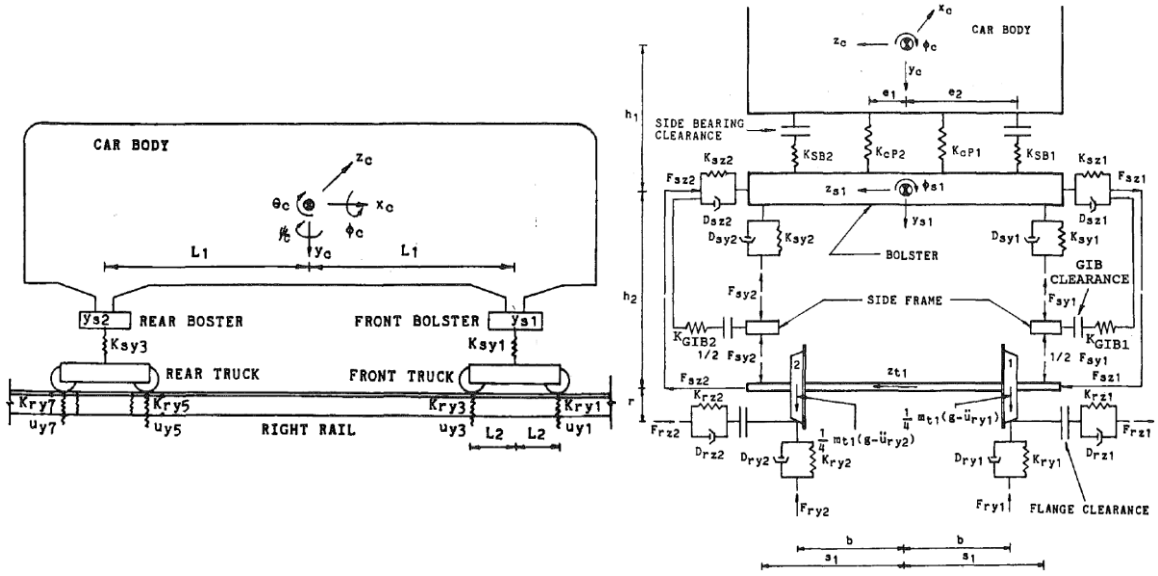

Figure 3.1 Three dimensional model of the vehicle (left) side view (right) front view (Wang et al. 1991)

3. 2. Vehicle Model

In the present research, a railway vehicle is simulated using a 31-DOF mass–spring–dashpot system including a car body, two bogies, four wheelsets and secondary and primary suspension systems. Note that primary suspension connects wheelsets to bogie frames and secondary suspension is a set of spring and dashpots that join bogie frames to car body. A schematic model of vehicle is shown in Figure 3.2. According to the figure, the car body is able to simulate vertical and lateral displacements, as well as roll and pitch motions in the vertical planes. Note that rotation around “x”, “y” and “z” axis is called

rolling, yawing and pitching, respectively. Figure 3.3 shows the rotation of a rigid body. The assumptions of vehicle model are summarized as:

- The secondary suspension that links the car-body and bogies is idealized by two similar linear springs and two viscous dashpots in both horizontal direction and vertical direction.
- The primary suspension connecting a bogie and a wheelset is characterized by the similar way described for the secondary suspension.
- The movement of the car-body and bogie frames are represented by five degrees of freedom (DOFs) in lateral, rolling, yawing, vertical and pitching directions. The mass and mass moments of a car-body, bogie and wheelset are lumped at their mass centers.
- Four DOFs in lateral, rolling, yawing and vertical directions characterize the movement of the wheelsets;
- Local deformations in the wheelset under contact forces are allowed.

Total DOFs of vehicle, consisting of one car-body, two bogies and four wheelsets are 31.

3. 3. Equilibrium equations of vehicle

There are a number of methods to find the equilibrium equations of a mass-spring-damper model. Selecting the most convenient method depends on the problem's configuration and model's level of complexity. The energy method has been used by most researchers to find equilibrium equations. For example, Lagrange's equations used by Tarighi and Wang (Tarighi & Wang 2015) to form the differential equations of different single truck and Tractor Semitrailers. By forming the expressions for the "Kinetic Energy", "Potential Energy" and "Damping Energy" and using the Lagrange's formulation, equations of

motion will be obtained.

$$\frac{d}{dt}\left(\frac{\partial T}{\partial \dot{q}_i}\right) - \frac{\partial T}{\partial q_i} + \frac{\partial V}{\partial q_i} + \frac{\partial D}{\partial \dot{q}_i} = 0 \qquad 3.1$$

Where "T", "V", and "D" are the Kinetic, Potential and Damping Energy of the system, respectively and "q" is the degree of freedom.

Another energy methods used for modeling of rail vehicle is principle of a stationary value of total potential energy of a dynamic system. It is assumed that the total potential energy of dynamic system is composed of the potential energy of the gravity (Π_g), the elastic strain energy (Π_e), the potential energy of the damping force(Π_d), the potential energy of the inertia force (Π_i), the potential energy of the Coulomb friction force (Π_c), the potential energy of the applied load of the system (Π_p), etc. at instant of time "t". The principle of virtual work can be expressed as (Lou & Zeng 2005)

$$\delta_\epsilon \Pi = 0$$
$$\Pi = \Pi_g + \Pi_e + \Pi_d + \Pi_i + \Pi_c + \Pi_p \qquad 3.2$$

The above formulation have been used to obtain the differential equations of the whole vehicle-track interaction system (Lou & Zeng 2005 and Lou 2005).

In the present study, the dynamic equilibrium method has been used to find the differential equations of the vehicle. To obtain the equations of motion, for each DOF, let the rigid body undergo a unit displacement (velocity or acceleration), and then considering the dynamic equilibrium of the body, the corresponding force in all DOF calculates.

For example, as Figure 3.4 shows, to derive car body equation of motion in "y" direction, a unit displacement is applied and generated forces in all DOFs must be determined.

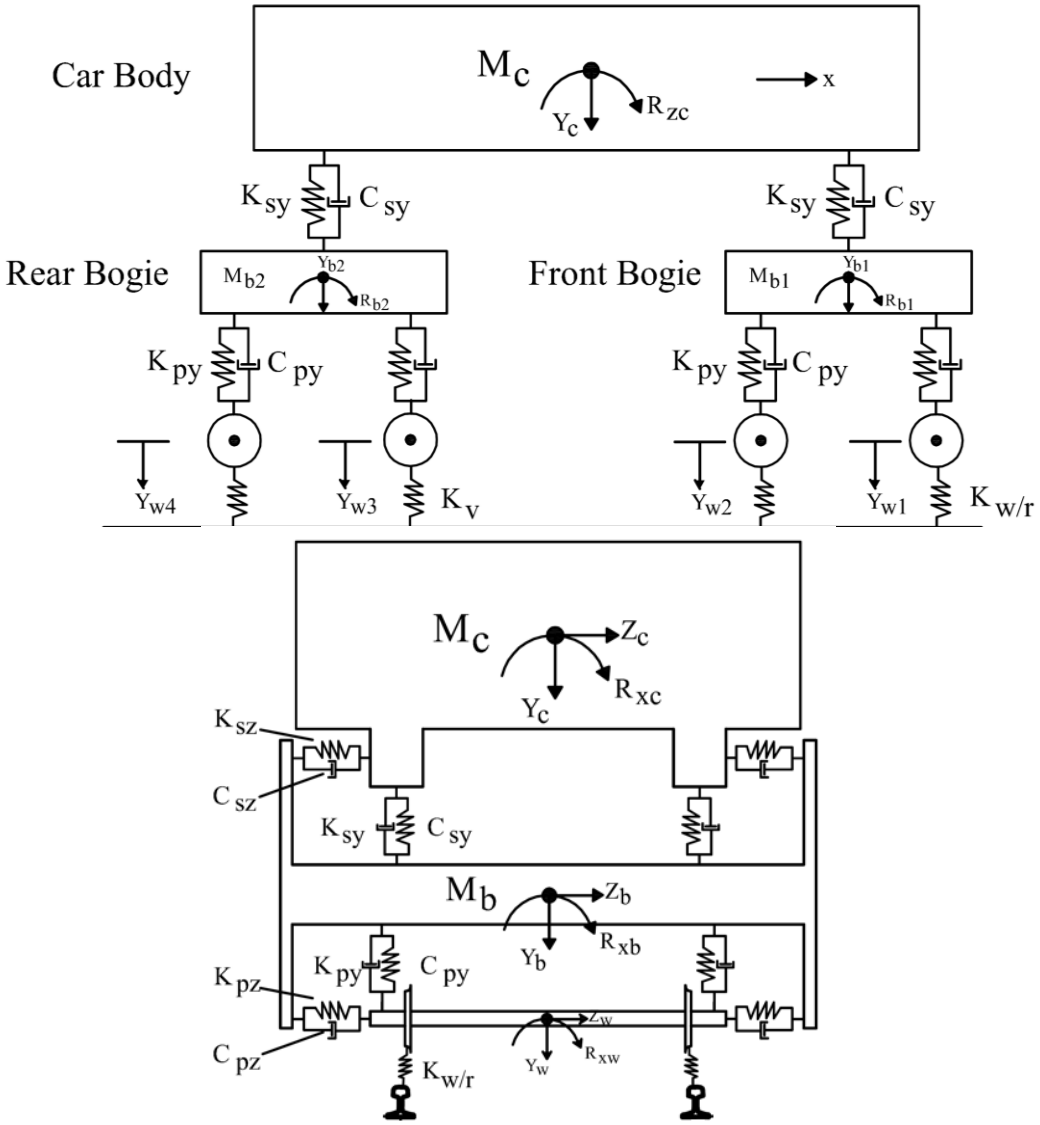

Figure 3.2 Vehicle model, (up) side view, (down) front view

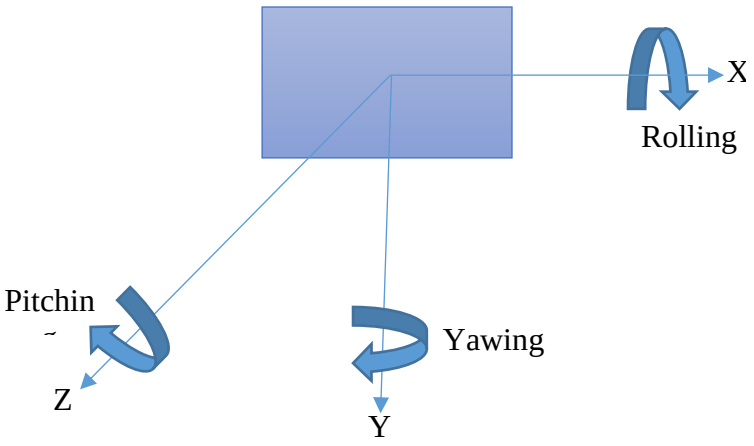

Figure 3.3 Degrees of freedom of a rigid body in x,y and z directions

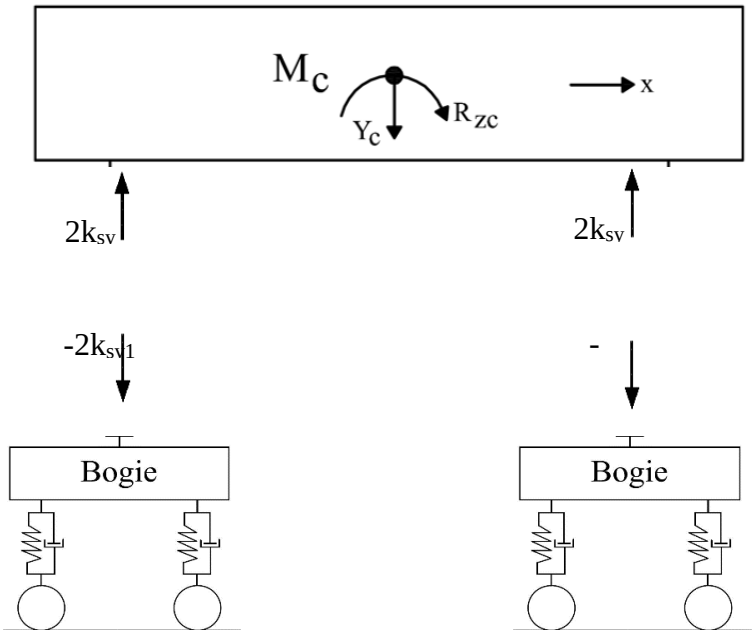

Figure 3.4 Forces on vehicle bodies due to car body unit displacement

$2(k_{sy1} + k_{sy2})$ is the force generated in car body in "y" direction due to a unit displacement of car body in "y" direction.

$k_{49} = -2k_{sy1}$ is the force generated in first bogie in "y" direction due to a unit displacement of car body in "y" direction.

$k_{4(14)} = -2k_{sy2}$ is the force generated in second bogie in "y" direction due to a unit

displacement of car body in “y” direction.

No force generates in other DOFs. Since viscous damper is used in the model, by replacing stiffness coefficients by damping coefficients, damping forces will be determined. So the equation of motion of car body motion in y direction would be:

$$M_y^c \ddot{y}^c + 2(C_{sy1} + C_{sy2})\,\dot{y}^c - 2C_{sy1}\,\dot{y}^{b1} - 2C_{sy2}\,\dot{y}^{b2} + 2\left(k_{sy1} + k_{sy2}\right) y^c - 2k_{sy1} y^{b1} - 2k_{sy2} y^{b2} = 0$$

The lateral, rolling, yawing, vertical and pitching directions are represented by the letters “z”, “R_x” , “R_y” , “y” and “R_z” , respectively, while “k” and “c” stand for stiffness and damping coefficients. The car-body, bogies and wheelsets are shown by the superscripts “c”, “b” and “w”, respectively. The parameters of vehicle and the values used for the simulation were tabulated in Table 3.1.

The dynamic equations of motion of 31 DOFs of vehicle then can be derived as follows:

Equations of car-body:

$$M_y^c \ddot{z}^c + 2(C_{sz1} + C_{sz2})\dot{z}^c - 2h_1(C_{sz1} + C_{sz2})\dot{R}_x^c - 2C_{sz1}\dot{z}^{b1} - 2C_{sz2}\dot{z}^{b2} - 2h_2(C_{sz1}\dot{R}_x^{b1} + C_{sz2}\dot{R}_x^{b2}) + 2(k_{sz1} + k_{sz2})z^c - 2h_1(k_{sz1} + k_{sz2})R_x^c - 2k_{sz1}z^{b1} - 2k_{sz2}z^{b2} - 2h_2(k_{sz1}R_x^{b1} + k_{sz2}R_x^{b2}) = 0 \qquad 3.3$$

$$J_x^c \ddot{R}_x^c + 2\left(b_2^2 C_{syj} + h_1^2 C_{szj}\right)\dot{R}_x^c - 2C_{szj}h_1\dot{z}^c + 2C_{szj}h_1\dot{z}^{bj} + \left(2C_{2zj}h_1h_2 - 2C_{syj}b_2^2\right)\dot{R}_x^{bj} + 2\left(b_2^2 k_{syj} + h_1^2 k_{szj}\right)R_x^c - 2k_{szj}h_1 z^c + 2k_{szj}h_1 z^{bj} + \left(2k_{szj}h_1h_2 - 2k_{syj}b_2^2\right)R_x^{bj} = 0 \qquad \text{j=1, 2} \qquad 3.4$$

$$J_y^c \ddot{R}_y^c + 2S_j^2 C_{szj}\dot{R}_y^c + (-1)^{j+1}2s_j C_{szj}\left(\dot{z}^{bj} + h_2\dot{R}_x^{bj}\right) + 2S_j^2 k_{szj}R_z^c + (-1)^{j+1}2S_j k_{szj}\left(Z_1^b + h_2 R_x^{bj}\right) = 0 \qquad \text{j=1, 2} \qquad 3.5$$

$$M_y^c \ddot{y}^c + 2C_{syj}\dot{y}^c - 2C_{syj}\dot{y}^{bj} + 2k_{syj}y^c - 2k_{syj}y^{bj} = 0 \qquad \text{j=1, 2} \tag{3.6}$$

$$J_z^c \ddot{R}_z^c + 2s_j^2 c_{syj}\dot{R}_z^c + (-1)^j 2s_j c_{syj}\dot{z}^{bj} + 2s_j^2 k_{syj}R_z^c + (-1)^j 2s_j k_{syj}z^{bj} = 0 \qquad \text{j=1, 2} \tag{3.7}$$

Dynamic equilibrium of the jth bogie:

$$M_z^{bj}\ddot{z}^{bj} + 2\left(C_{szj} + 4C_{pzj}\right)\dot{z}^{bj} + \left(2C_{szj}h_2 - 4C_{pzj}h_3\right)\dot{R}_x^{bj} - 2C_{szj}\dot{z}^c + 2C_{szj}h_1\dot{R}_x^c + 2C_{szj}h_1\dot{R}_x^c + (-1)^{j+1}2c_{szj}S_j\dot{R}_y^c - 2C_{pzj}\dot{Z}_k^{wj} + \left(2k_{szj} + 4k_{pzj}\right)z^{bj} + \left(2k_{szj}h_2 - 4k_{pzj}h_3\right)R_x^{bj} - 2k_{szj}z^c + 2k_{szj}h_1R_x^c + (-1)^{j+1}2k_{szj}S_jR_y^c - 2k_{pzj}z_k^{wj} = 0 \text{ k=1, 2} \tag{3.8}$$

$$J_{xj}^b \ddot{R}_x^{bj} + \left(2h_2C_{szj} - 4h_3C_{pzj}\right)\dot{z}^{bj} + \left(2b_2^2C_{syj} + 2h_2^2C_{szj} + 4h_3^2C_{pzj} + 4b_1^2C_{pyj}\right)\dot{R}_x^{bj} - 2h_2C_{szj}\dot{z}^c + 2\left(h_1h_2C_{szj} - b_2^2C_{syj}\right)\dot{R}_x^c + (-1)^{j+1}2h_2S_jc_{szj}\dot{R}_y^c + 2h_3c_{pzj}\dot{Z}_k^{wj} - 2b_1^2C_{pyj}\dot{R}_x^{wj} + \left(2h_2k_{szj} - 4h_3k_{pzj}\right)z^{bj} + \left(2b_2^2k_{syj} + 2h_2^2k_{szj} + 4h_3^2k_{pzj} + 4b_1^2k_{pyj}\right)R_x^{bj} - 2h_2k_{szj}z^c + 2\left(h_1h_2k_{szj} - b_2^2k_{syj}\right)R_x^c + (-1)^{j+1}2h_2S_nk_{szj}R_y^c + 2h_3k_{pzj}Z_k^{wj} - 2b_1^2k_{pyj}R_{xk}^{wj} = 0 \qquad \text{k=1, 2} \tag{3.9}$$

$$J_y^{bj}\ddot{R}_{Ynj}^b + 4t_j^2C_{pzj}\dot{R}_y^{bj} + (-1)^{k+1}2t_jC_{pzj}\dot{Z}_{njk}^w + 4t_j^2k_{pzj}R_y^{bj} + (-1)^{k+1}2t_jk_{pzj}Z_k^{wj} = 0 \quad \text{k=1, 2} \tag{3.10}$$

$$M_y^{bj}\ddot{y}^{bj} + \left(2C_{syj} + 4C_{pyj}\right)\dot{y}^{bj} - 2C_{syj}\dot{y}^c + (-1)^j 2S_jc_{syj}\dot{R}_z^c - 2C_{pyj}\dot{y}_k^{wj} + \left(2k_{syj} + 4k_{pyj}\right)y^{bj} - 2k_{syj}y^c + (-1)^j 2S_jk_{syj}R_z^c - 2k_{pyj}Z_k^{wj} = 0 \tag{3.11}$$

$$J_{zj}^b \ddot{R}_z^{bj} + 4t_j^2C_{pyj}\dot{R}_{zj}^b + (-1)^k 2t_jC_{pyj}\dot{y}_k^{wj} + 4t_j^2k_{pyj}R_{zj}^b + (-1)^k 2t_jk_{pyj}y_k^{wj} = 0 \tag{3.12}$$

Dynamic equilibrium of the kth wheelset of the jth bogie:

$$M_{z,k}^{wj}\ddot{Z}_{jk}^{wj} + 2C_{pz}\dot{Z}_{k}^{wj} - 2C_{pz}\dot{z}^{bj} + 2C_{pz}h_3\dot{R}_{x}^{bj} + (-1)^{k+1}2C_{pz}t\dot{R}_{y}^{bj} + 2k_{pz}Z_{k}^{wj} - 2k_{pz}z^{bj} + 2k_{pz}h_3R_{x}^{bj} + (-1)^{k+1}2k_{pz}tR_{y}^{bj} = F_{z,jk}^{w-r} \quad 3.13$$

$$J_{x}^{w}\ddot{R}_{xk}^{wj} + 2C_{py}b_1^2\dot{R}_{xk}^{wj} - 2C_{py}b_1^2\dot{R}_{x}^{bj} + 2k_{py}b_1^2R_{xk}^{wj} - 2k_{py}b_1^2R_{x}^{bj} = M_{x,jk}^{w-r} \quad 3.14$$

$$J_{y}^{w}\ddot{R}_{yk}^{wj} + 2C_{px}b_1^2\dot{R}_{yk}^{wj} - 2C_{px}b_1^2\dot{R}_{y}^{bj} + 2(k_{px}b_1^2 + k_{Ry})R_{yk}^{wj} - 2(k_{px}b_1^2 + k_{Ry})R_{x}^{bj} = M_{y,jk}^{w-r} \quad 3.15$$

$$M_{y,k}^{wj}\ddot{y}_{k}^{wj} + 2C_{py}\dot{y}_{k}^{wj} - 2C_{py}\dot{y}^{bj} + (-1)^{k}2C_{py}t_{jk}\dot{R}_{z}^{bj} + 2k_{py}Y_{k}^{wj} - 2k_{py}Y_{nj}^{b} + (-1)^{k}2k_{py}t_{jk}R_{z}^{bj} = F_{y,jk}^{w-r} \quad 3.16$$

Where

h1: the distance between secondary suspension and cab body' centroid

h2: the distance between secondary suspension and bogie frames' centroid

h3: the distance between primary suspension and bogie frames' centroid

t: the distance between two wheels of the same bogie

s: the distance between car body and bogie centers

F_{y}^{w-r}: wheel-rail contact force in "y" direction

F_{z}^{w-r}: wheel-rail contact force in "z" direction

M_{y}^{w-r}: wheel-rail moment around "y" axis (yawing)

M_{x}^{w-r}: wheel-rail moment around "x" axis (rolling)

Note that no axial forces are considered in the analysis, as a result, wheel-rail contact force in "x" direction is zero.

3. 4. Verification

Verification of vehicle models consists of two parts. First, it is shown that springs and dashpots of vehicle work properly and the proposed formulations could successfully model damping and stiffness of each component into the formulas; and second, lateral and vertical displacements of each degrees of freedom can be recorded by using the derived formulations.

To check the dashpots of the vehicle, displacements of car body, bogie frames and wheelsets in vertical direction is monitored for a sine shape bump with amplitude of 0.05 meter.

$y(t) = abs(0.05\cos(10t)) \quad 0<t<3.3$

The results are shown for 10 seconds. As Figure 3.5 shows, after 3.3 seconds (10/3) vehicle vibrates freely so the applied displacement after this time would be zero. As a result, forced and free vibration of vehicle can be observed. Figure 3.6 to Figure 3.11 show displacement history of wheel, bogie frames and car body for two cases of damped and undamped systems. The figures demonstrate that the model can successfully simulate the effect of damping on vehicle and free vibration. The values of primary and secondary suspension damping coefficients are presented in Table 3.1

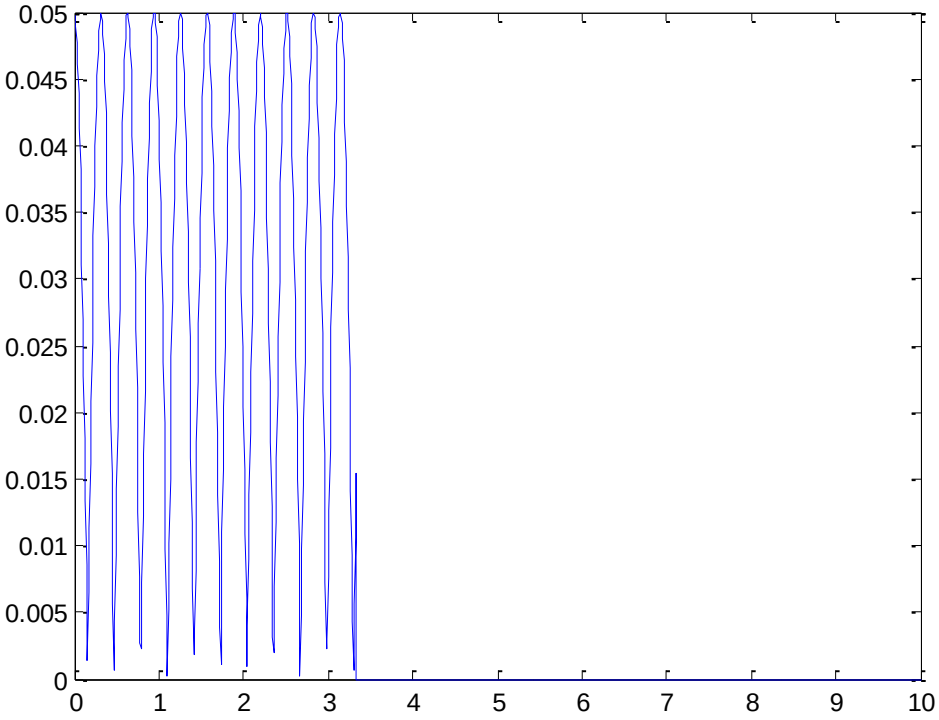

Figure 3.5 Applied displacement to rail

Table 3.1 Vehicle parameters

Notation	Parameter	Value	Unit
M_c	Mass of car body	47	ton
$J^c_{x,y,z}$	Car body inertia moments about x, y and z	49.50, 1950 ,2210	Ton.m^2
M_b	Mass of bogie	3.1	ton
$J^b_{x,y,z}$	Bogie inertia moments about x, y and z	1.55, 2.34, 5.1	Ton.m^2
K_{sy}	Vertical stiffness of secondary suspension	2.15×10^5	N/m
K_{sz}	Lateral stiffness of secondary suspension	2.75×10^5	N/m
C_s	Damping of secondary suspension	10^4	N.s/m
K_{py}	Vertical stiffness of primary suspension	6.55×10^5	N/m
K_{pz}	Lateral stiffness of primary suspension	2.35×10^6	N/m
C_p	Damping of primary suspension	10^4	N.s/m
M_w	Mass of wheel axle	1.7	ton
$J^w_{x,y,z}$	Wheel axle inertia moments about x, y and z	1.5, 1.2, 0.005	Ton.m^2
L_c	Length of car body	6.3	m
R_{wheel}	Wheel radius	0.5	m
E	Wheel's modulus of elasticity	2×1011	N/ m^2
ν	Wheel's Poisson ratio	0.3	-
h1	the distance between secondary suspension and cab body' centroid	0.6	m
h2	the distance between secondary suspension and bogie frames' centroid	0.35	m
h3	the distance between primary suspension and bogie frames' centroid	0.2	m
t	the distance between two wheels of the same bogie	1.2	m
s	the distance between car body and bogie centers	2.25	m

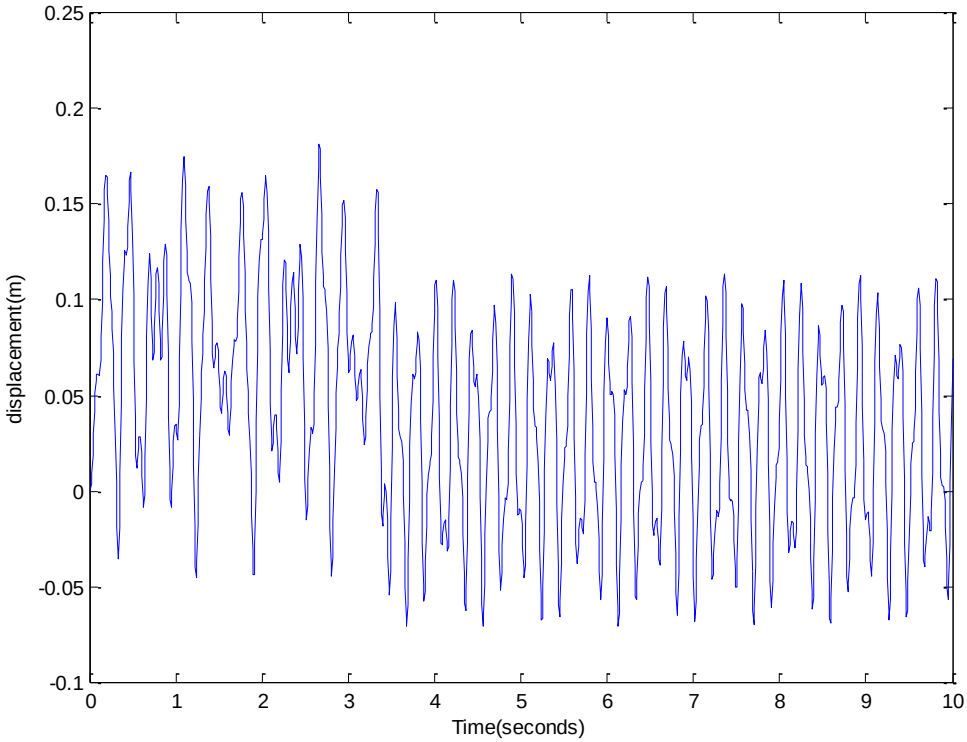

Figure 3.6 Wheel displacement (no damping)

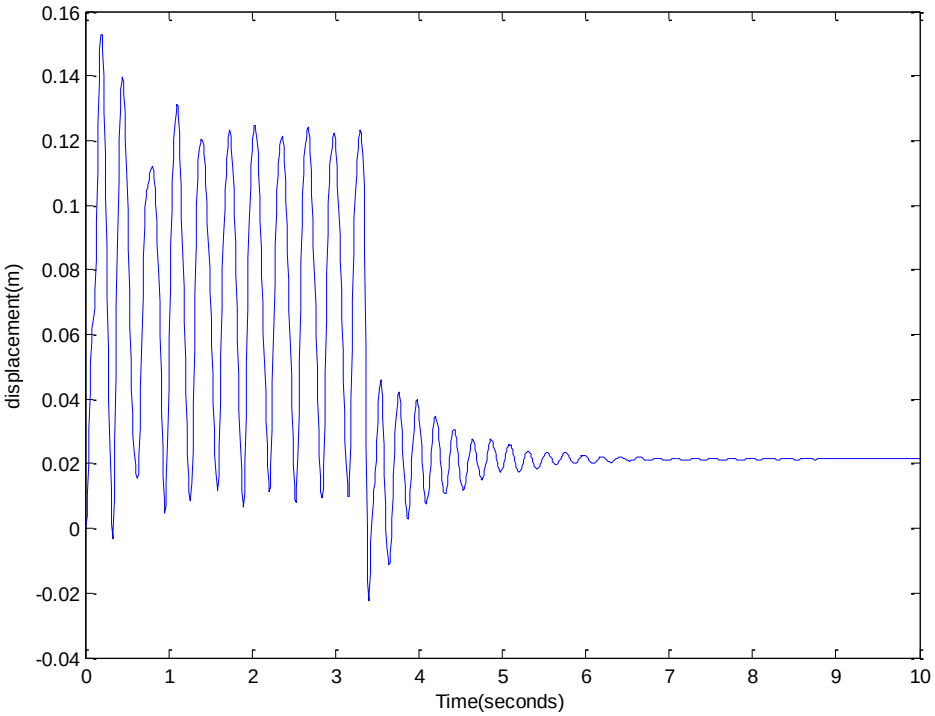

Figure 3.7 Wheel displacement (including damping)

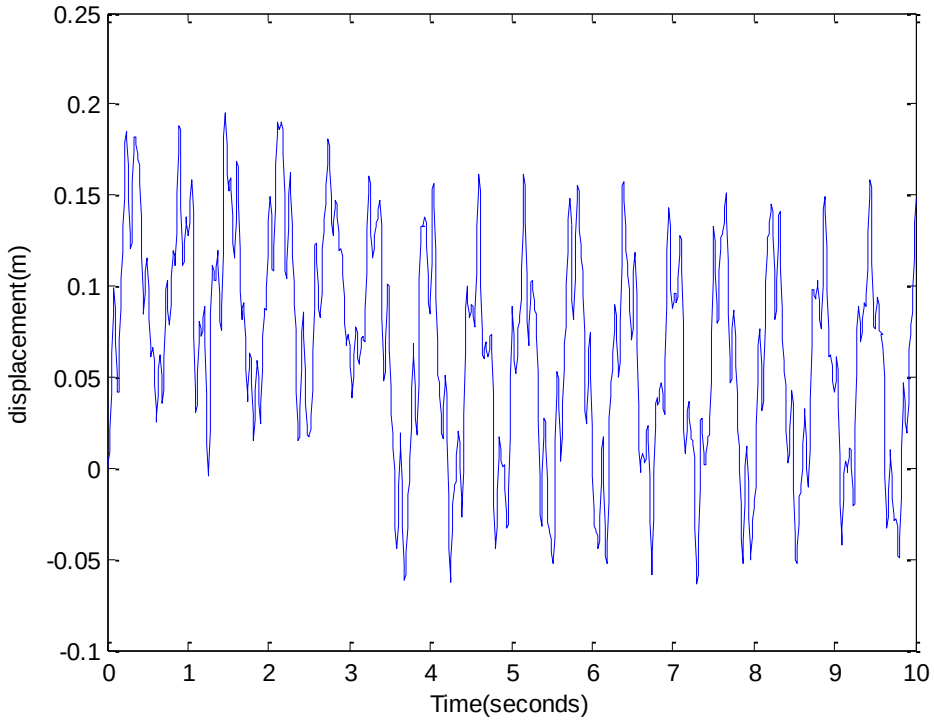

Figure 3.8 Bogie displacement (no damping)

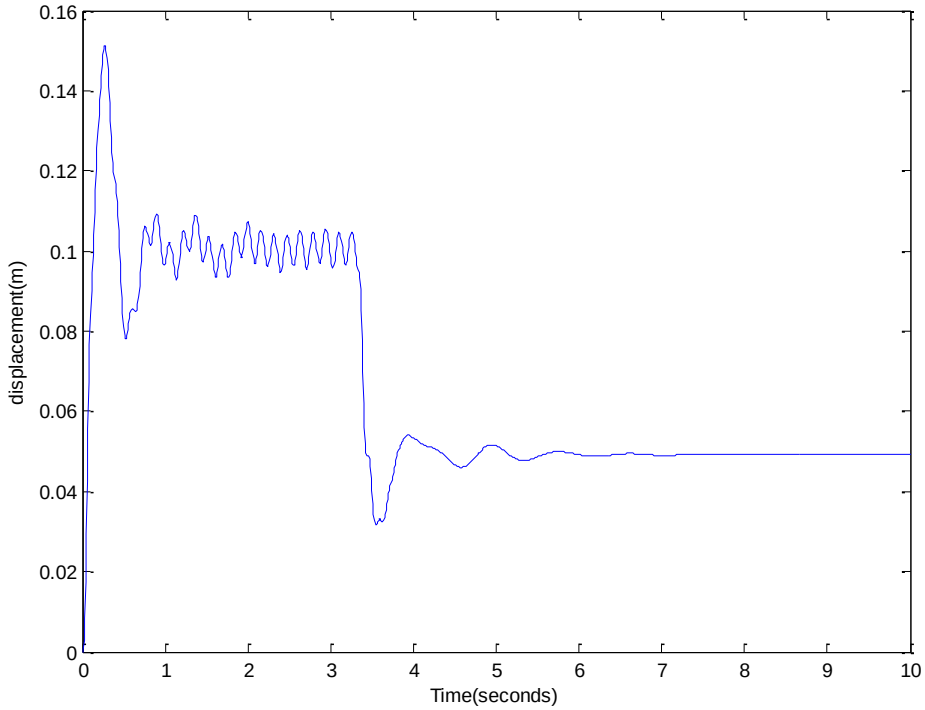

Figure 3.9 Bogie displacement (including damping)

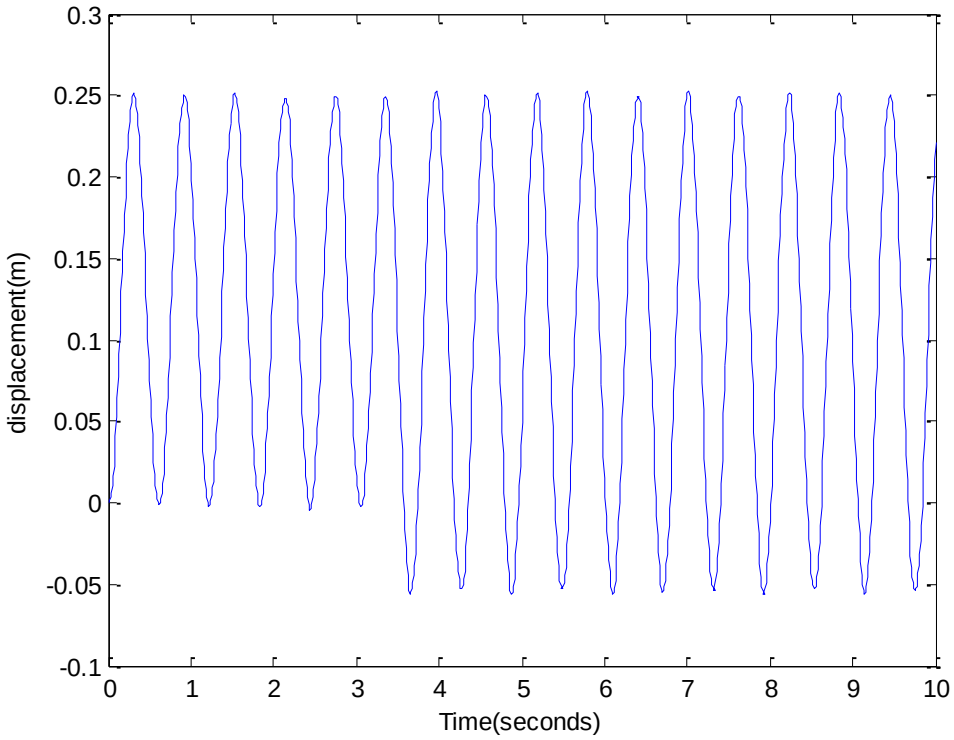

Figure 3.10 Car body displacement (no damping)

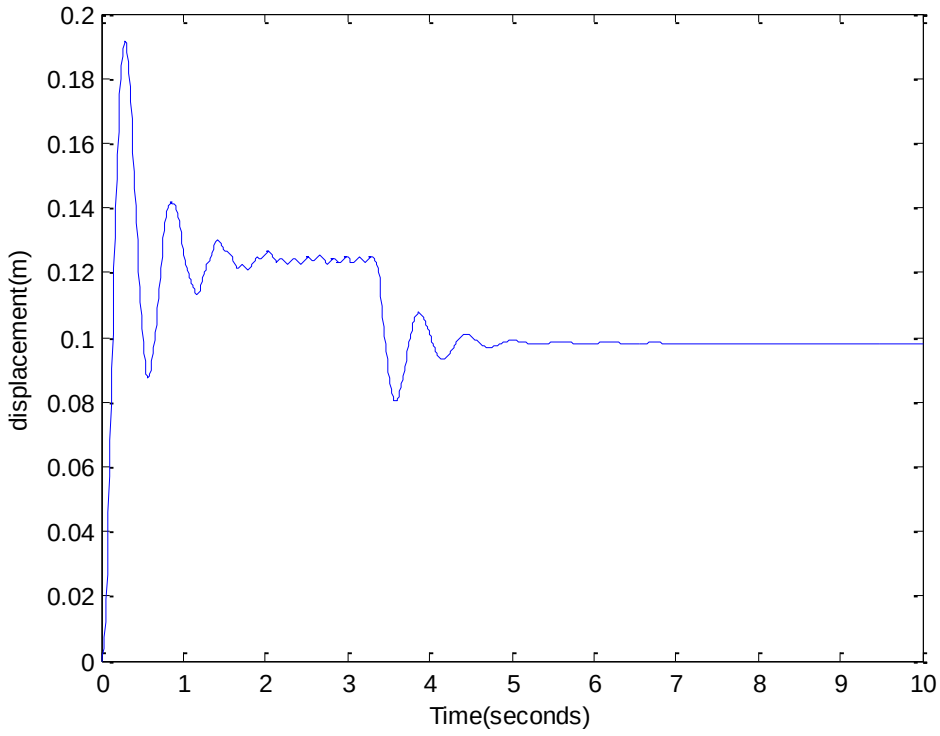

Figure 3.11 Car body displacement (including damping)

To control the lateral response of vehicle to lateral loading, a vertical half-staggered rectified sine displacement as rail irregularities is applied to rails. Right and left rail have phase angle difference of 90 degrees so vibration in lateral direction, as well as vertical motions occurs. Figure 3.12 shows the applied irregularities to right and left rails. Figure 3.13 to Figure 3.15 depict the lateral displacements of wheelset, bogie and car body, respectively. Vertical displacements of vehicle are also shown in Figure 3.16 to Figure 3.18.

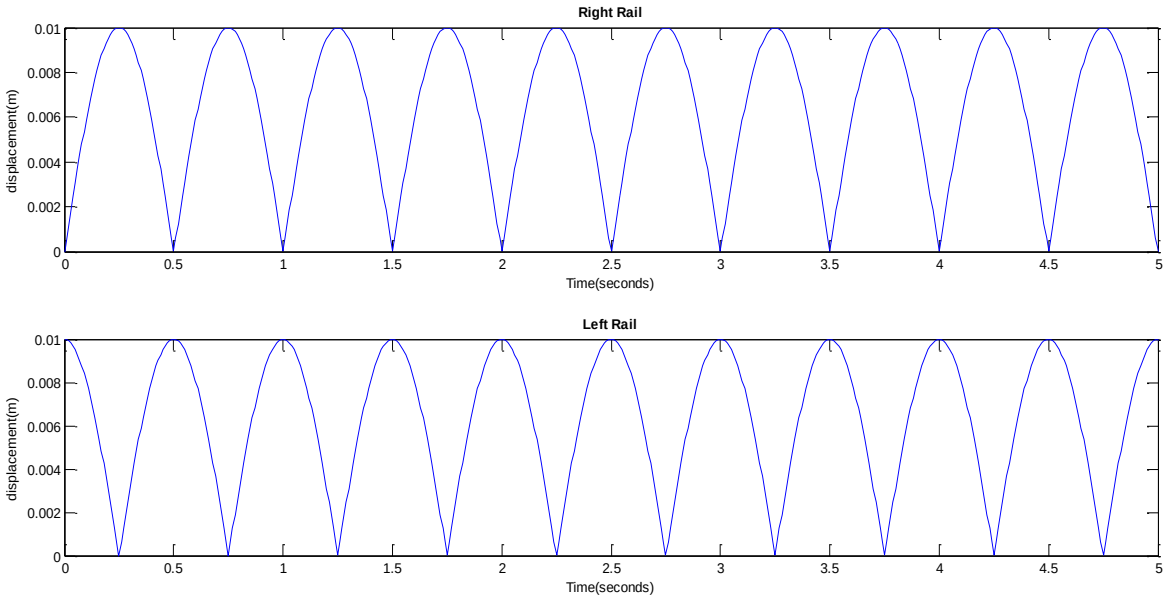

Figure 3.12 Rail irregularities (up) right rail (down) left rail

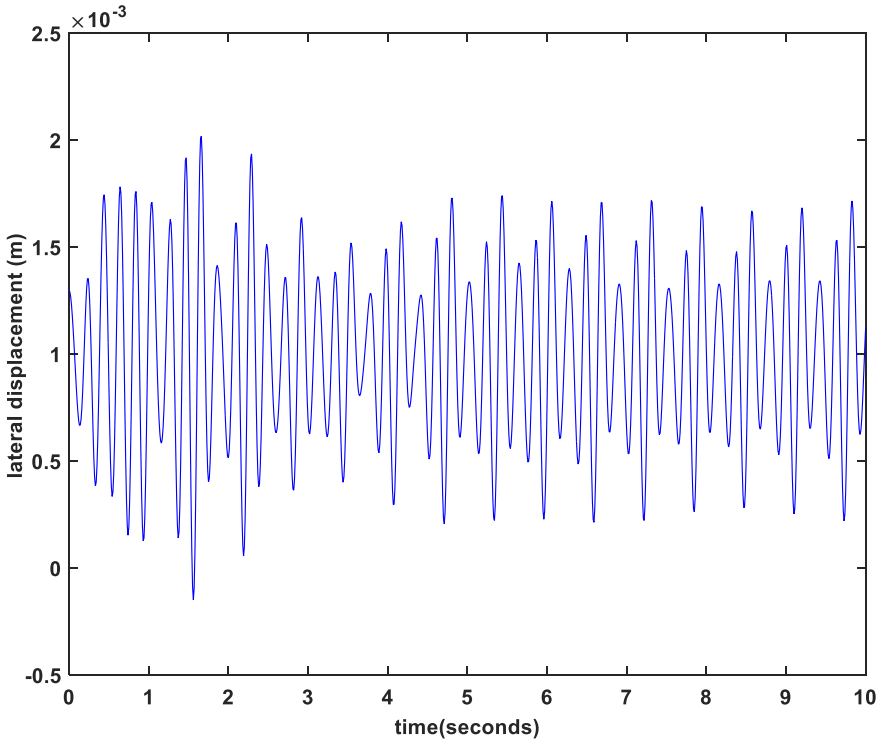

Figure 3.13 lateral displacement of wheel

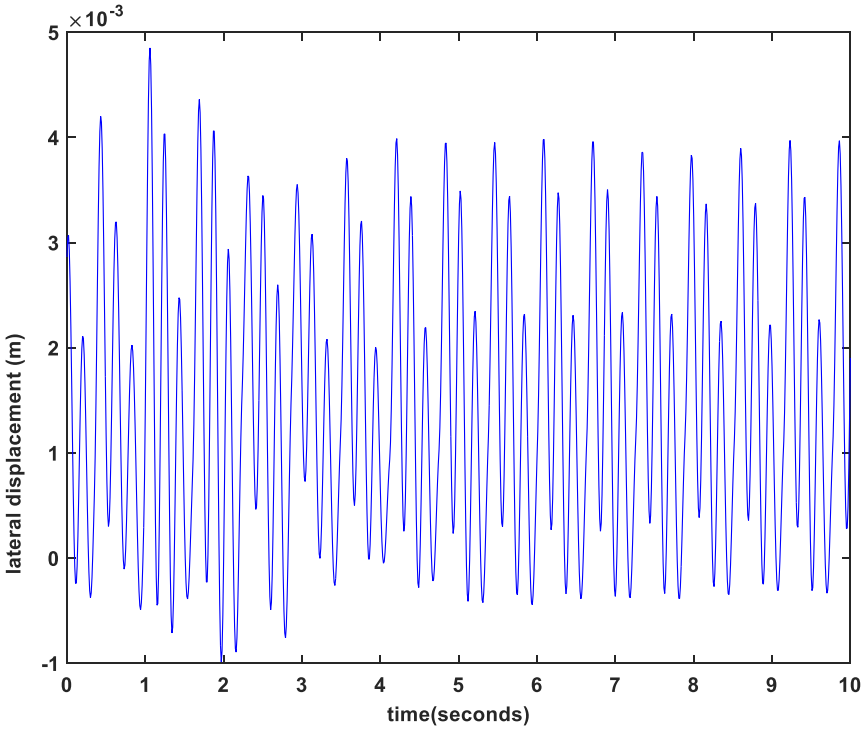

Figure 3.14 lateral displacement of bogie

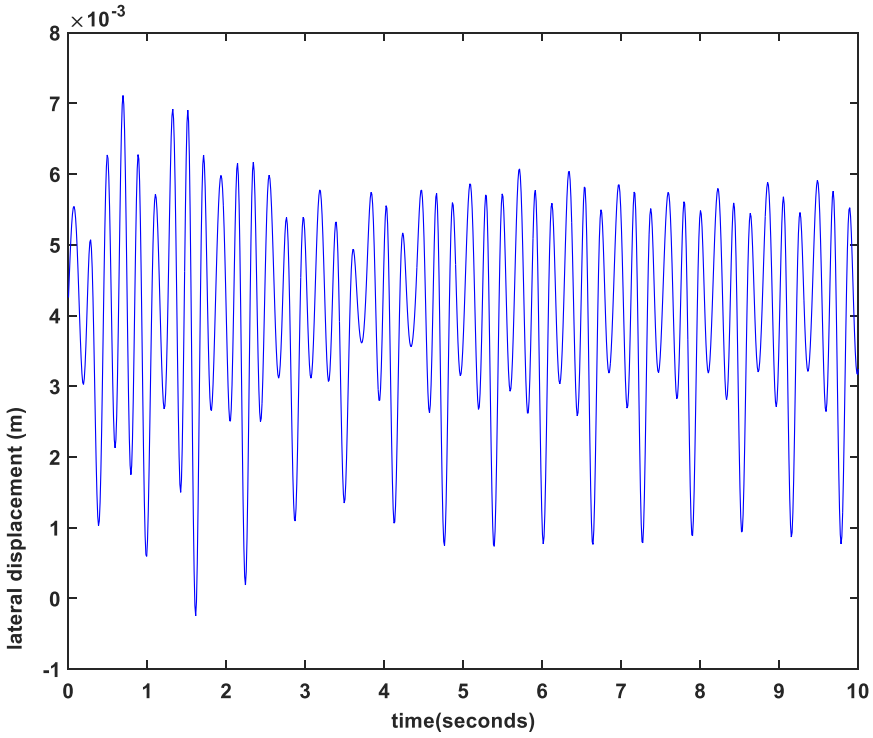

Figure 3.15 lateral displacement of car body

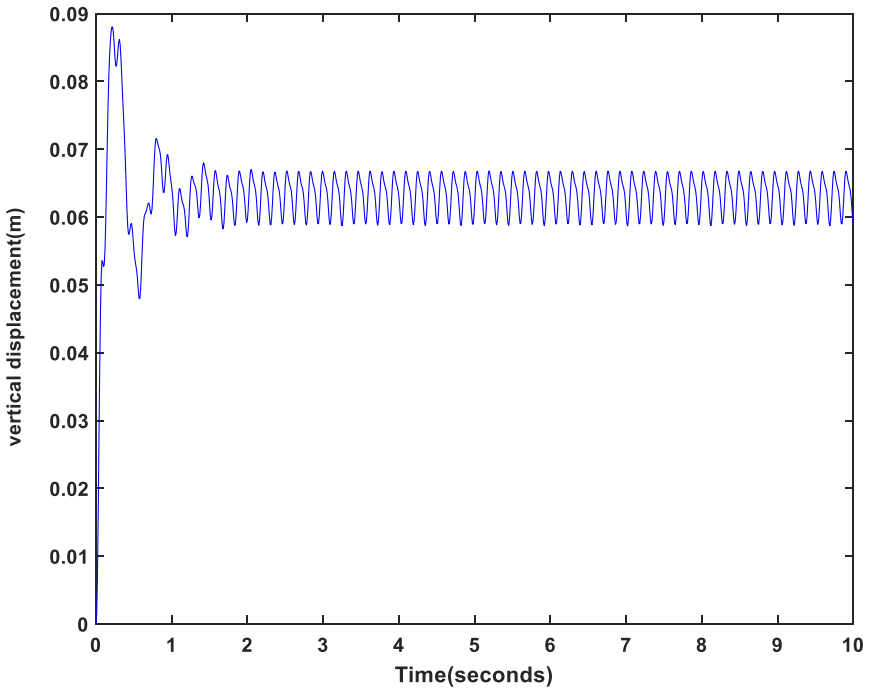

Figure 3.16 vertical displacement of Wheelset

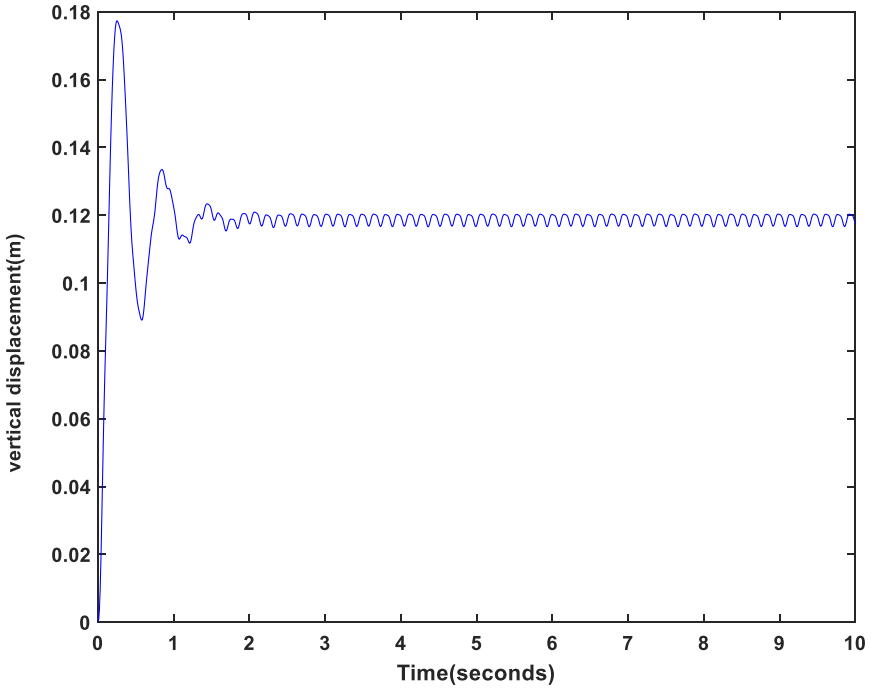

Figure 3.17 vertical displacement of Bogie

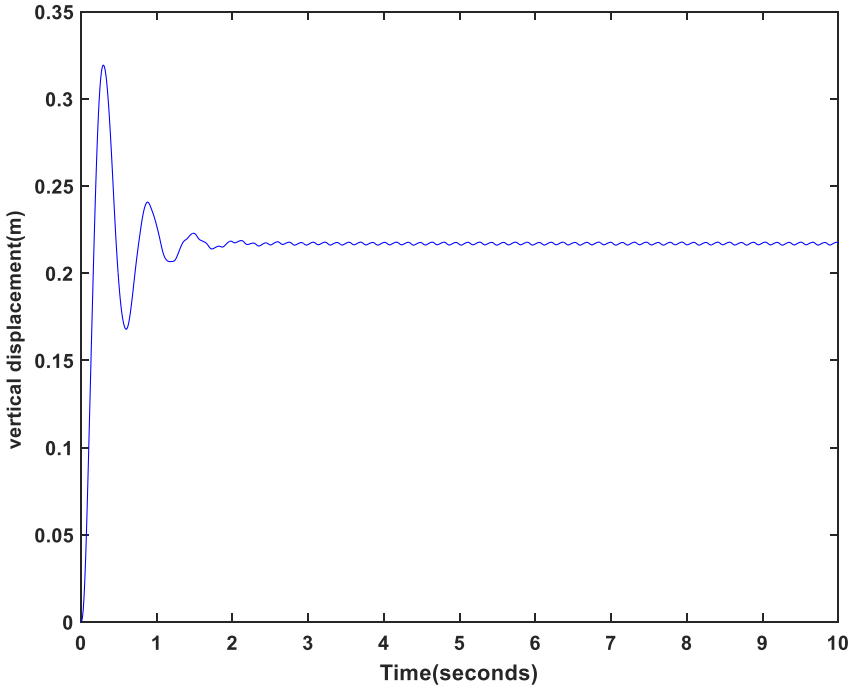

Figure 3.18 vertical displacement of car body

3. 5. The Vehicle's Natural Frequencies

Since mass and stiffness matrices of vehicle are formed, natural frequencies can be calculated. Free vibration of a linear system is determined by harmonic functions as shown in the following equation: (Chopra 2011)

$$\{u\} = \{\varphi_i\} cos\omega_i t \qquad 3.17$$

where "φ_i" is eigenvector of i-th natural frequency (ω_i)

Neglecting damping, the equation of motion reads

$$(-\omega_i^2[M] + [K])\{\varphi_i\} = \{0\} \qquad 3.18$$

This is an Eigen value problem and expanding the determinant gives algebraic equations of the Nth degree. The "N" roots of this equation represent the frequencies of the "N" modes of the vibration.

$$|[K - \omega^2 M]| = 0 \qquad 3.19$$

The mode having the lowest frequency is called the first mode, the next higher frequency is the second mode, etc.

For the rail vehicle, with the values of mass and stiffness shown in Table 3.1, the first six frequencies are:

$\omega_1 = 6.85\, rad/s \;\; or \;\; f_1 = 1.1\, Hz$

$\omega_2 = 7.01\, rad/s \;\; or \;\; f_2 = 1.12\, Hz$

$\omega_3 = 7.29\, rad/s \; or \;\; f_3 = 1.16\, Hz$

$\omega_4 = 10.22\, rad/s \; or \;\; f_4 = 1.63\, Hz$

$\omega_5 = 11.78\, rad/s \; or \;\; f_5 = 1.87\, Hz$

$\omega_6 = 28.30\, rad/s \; or \;\; f_6 = 4.50\, Hz$

4. Rail Irregularities

4. 1. Introduction

Rail irregularities are defined as deviations of rail from its ideal position. Irregularities are the major sources of track excitations during the passage of vehicles and are usually caused by imperfections of materials, tolerance errors in manufacturing of rail and other track components. Rail joints, terrain irregularities and errors in surveying during the design and construction phases of track also add to the track irregularities. Depending on the track characteristics, rail flaws may be periodic or random. Periodic irregularities are mainly attributed to flat wheels, defects in fastening system or sleepers. Periodic irregularities of the track are analytically described by the Fourier analysis. However, since random irregularities have no specific patterns and many factors contribute to them, statistical process must be used to characterize the flaws (Frýba 1996) (Wang 1984).

There are four types of track irregularities namely vertical profile, cross-level, alignment and gauge irregularities.

Vertical profile is defined as vertical deviation of rail from its planned geometry.

Gauge is defined as the horizontal distance between two rails that should be constant. For a standard track in straight route, as defined by AREMA, the gage is 56.5” or 1435 mm. Any change in the distance between rails is called gauge flaw. (American Railway Engineering and Maintenance-of-Way Association 2010)

Alignment is lateral movement of track from its centerline. It usually happens as a result of excessive lateral loading and low lateral resistance of track due to superstructure or substructure defects. This problem causes extra pressure on vehicle and track and expedites the deterioration rate of track.

Cross level (super elevation or cant) is the vertical distance between right and left rails that causes unbalanced centrifugal forces. To avoid unbalanced lateral force at curves, the level of outer rail should be raised. Extra cross level or deficiency in rails level cause extra forces on inner and outer rails. In extreme cases there is a risk of derailments.

Figure 4.1 shows the different types irregularities.

This chapter discusses the four types of random track irregularities and presents different approaches to describe them depending on the track conditions. Different models used in different countries will be presented and artificial rail surface for poor and good track quality will be produced.

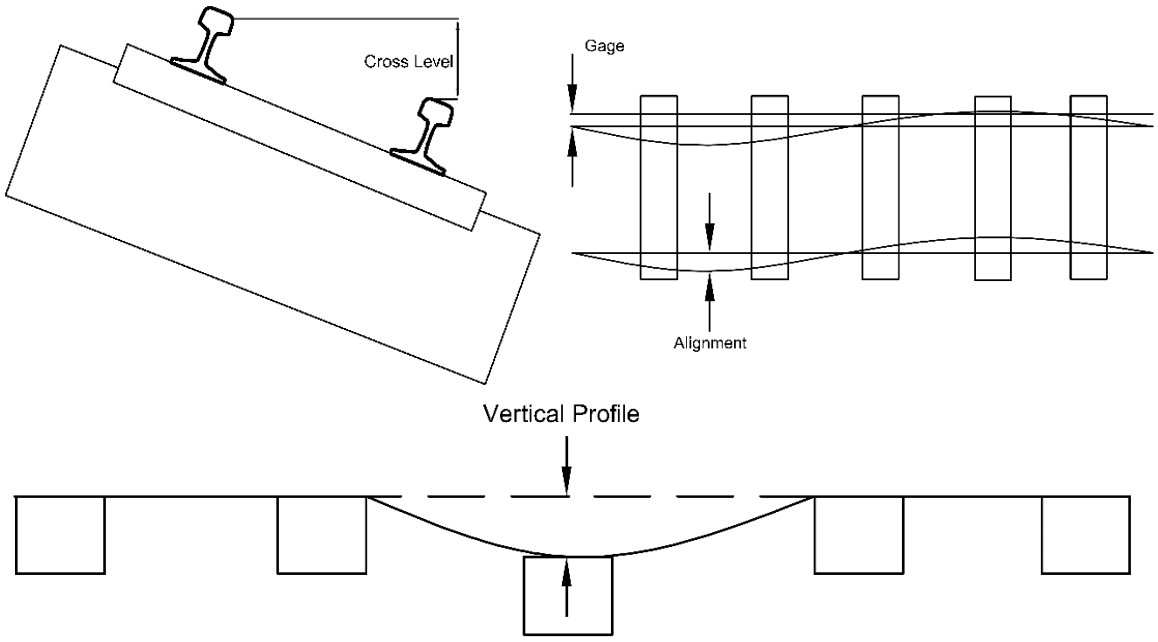

Figure 4.1 Four types of track irregularities

4. 2. Formulations to rail irregularities

Rail irregularities are random in nature and as a result, each measurement of rail profile produces a unique surface that cannot be predicted. Rail profile can be characterized by stochastic Gaussian ergodic processes which mean that the statistical measures are

independent of time and every signal of the ensemble can be considered representative for the statistical properties of the process.

To produce the rail surface profile, some expressions should be defined first;

The mean value ($\bar{\varepsilon}$) and correlation function ($R_\varepsilon(\xi)$) of an ergodic stationary process $\varepsilon(x)$ in the range 0-L, is defined:

$$\bar{\varepsilon} = \lim_{n\to\infty} \frac{1}{L} \int_0^L \varepsilon(x)\, dx \tag{4.1}$$

$$R_\varepsilon(\xi) = \lim_{n\to\infty} \frac{1}{L} \int_0^L \varepsilon(x)\varepsilon(x-\xi)\, dx \tag{4.2}$$

Power Spectrum Density (PSD) is the Fourier transform of the correlation function. PSD is defined by the following formula

$$S(\Omega) = \int_{-\infty}^{\infty} R_\varepsilon(\xi) e^{-2\pi i \Omega \xi}\, d\xi \tag{4.3}$$

Where "Ω" is the frequency,

The inverse Fourier transform is

$$S(\xi) = \int_{-\infty}^{\infty} R_\varepsilon(\Omega) e^{2\pi i \Omega \xi}\, d\Omega \tag{4.4}$$

In case of $\xi = 0$, the correlation function is mean square value:

$$\overline{\varepsilon^2} = \lim_{n\to\infty} \frac{1}{L} \int_0^L \varepsilon^2(x)\, dx \tag{4.5}$$

Which results the following equation

$$\overline{\varepsilon^2} = \int_{-\infty}^{\infty} S(\Omega)\, d\Omega \tag{4.6}$$

For one-sided spectral density, i.e.$\Omega \geq 0$, PSD can be obtained by

$$G(\Omega) = 2S(\Omega) \tag{4.7}$$

The definition of PSD shows that the mean square value of a signal in specific frequency range is equal to the area under the spectral density function.

Using the following formula proposed by Yang, rail surface irregularities can be simulated (Y.C.Yang 1986)

$$\varepsilon(t) = \sum_{n=1}^{N} \alpha_n cos(2\pi\Omega_n t - \beta_n) \tag{4.8}$$

Where "β_n" is random phase angle in the range of $[0,2\pi]$ and "α_n" is defined by

$$\overline{\varepsilon^2} = \sum_{n=1}^{N} \frac{1}{2}\alpha_n^2 \tag{4.9}$$

The mean square value, "$\overline{\varepsilon^2}$", can also be defined over a range of frequency divided into "N" intervals with bandwidth "$\Delta\Omega$"

$$\overline{\varepsilon^2} = \sum_{n-1}^{N} G(\Omega_n)\,\Delta\Omega \tag{4.10}$$

So "α_n" can be resulted from

$$\alpha_n = \sqrt{2G(\Omega_n)\Delta\Omega}$$

The rail irregularities then read

$$\varepsilon(t) = \sum_{n=1}^{N} \sqrt{2G(\Omega_n)\Delta\Omega} cos(2\pi\Omega_n t - \beta_n) \tag{4.11}$$

$$\Omega_n = \Omega\Delta\Omega = \Omega\frac{\Omega_u - \Omega_l}{N}$$

where "N" represents the total number of discrete spatial frequencies, and "Ω_n" is the nth

discrete frequency. "Ω_u" and "Ω_l" are, respectively, the maximum and minimum frequencies.

4. 3. Spectral Density Functions for Rail Irregularities

As discussed earlier, rail irregularities should be modeled by using PSD functions. Different countries conducted comprehensive tests to record rail surface irregularities for different track conditions. Employing the PSD functions, an artificial rail surface is simulated and the response of track and vehicle can be measured. This section reviews a number of PSD functions derived from field measurements in different countries and railroads.

4. 3. 1. The SNCF Function

The SNCF[1] or French National Railway Company suggested the following PSD formula

$$G(n) = \frac{10^{-6}A}{\left(1 + \frac{n}{n_0}\right)^3} \qquad 4.12$$

Where" n_0" is equal to 0.307 cycles/m. "A" is a parameters that shows the quality of track. For good rail condition, A = 160 and for poor condition, A = 550. Figure 4.2 show the power spectral density formula of the rail roughness proposed by SNCF for good and poor track conditions. Figure 4.3 and Figure 4.4 also illustrate the waveform of rail roughness for good and poor state.

[1] Société Nationale des Chemins de Fer François

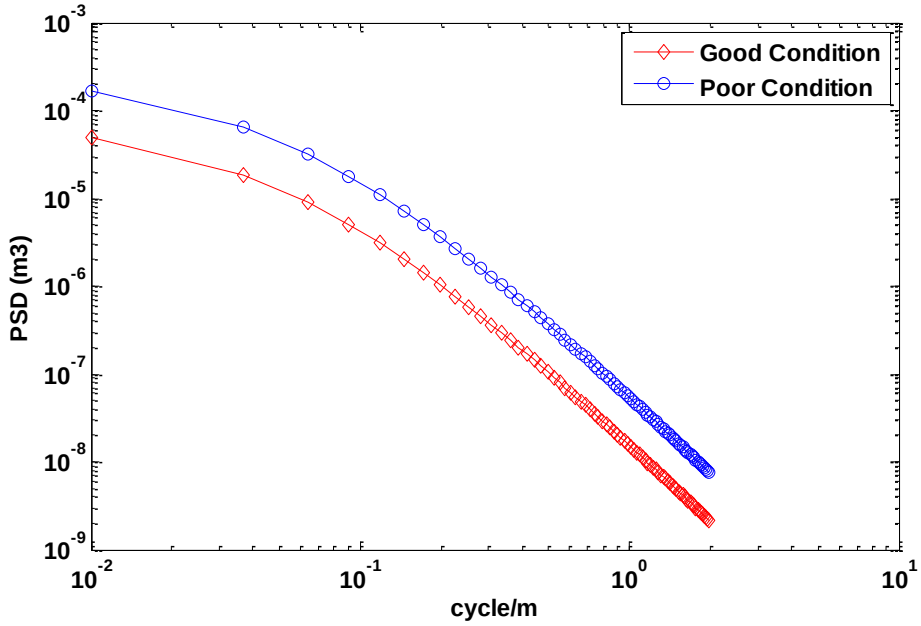

Figure 4.2 PSD function of the rail roughness proposed by SNCF

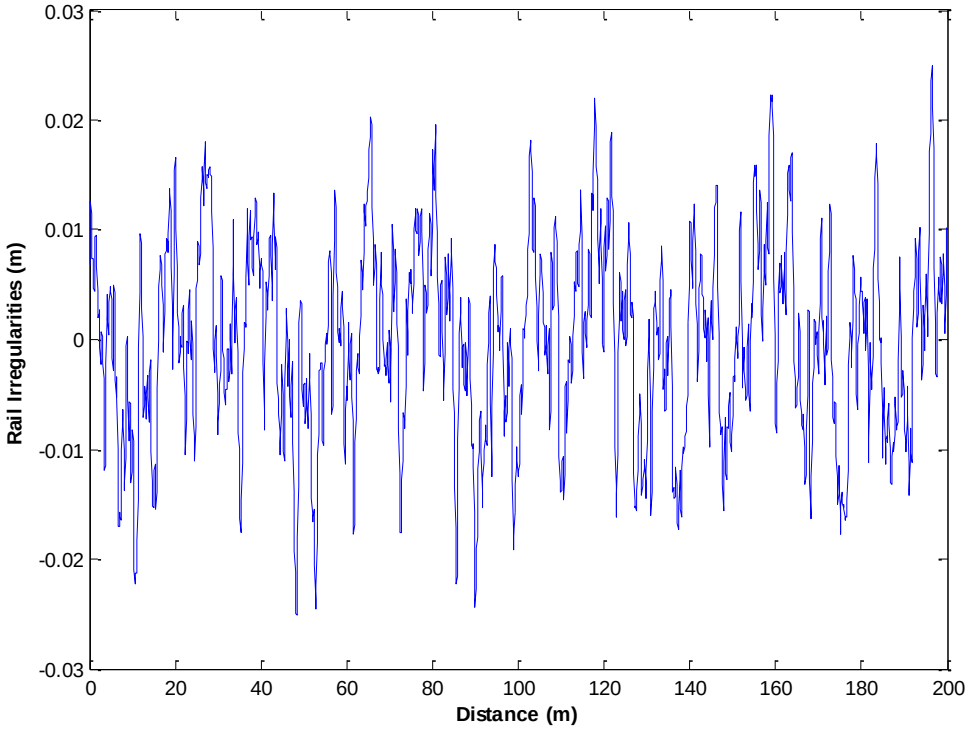

Figure 4.3 Rail irregularities proposed by SNCF for poor state

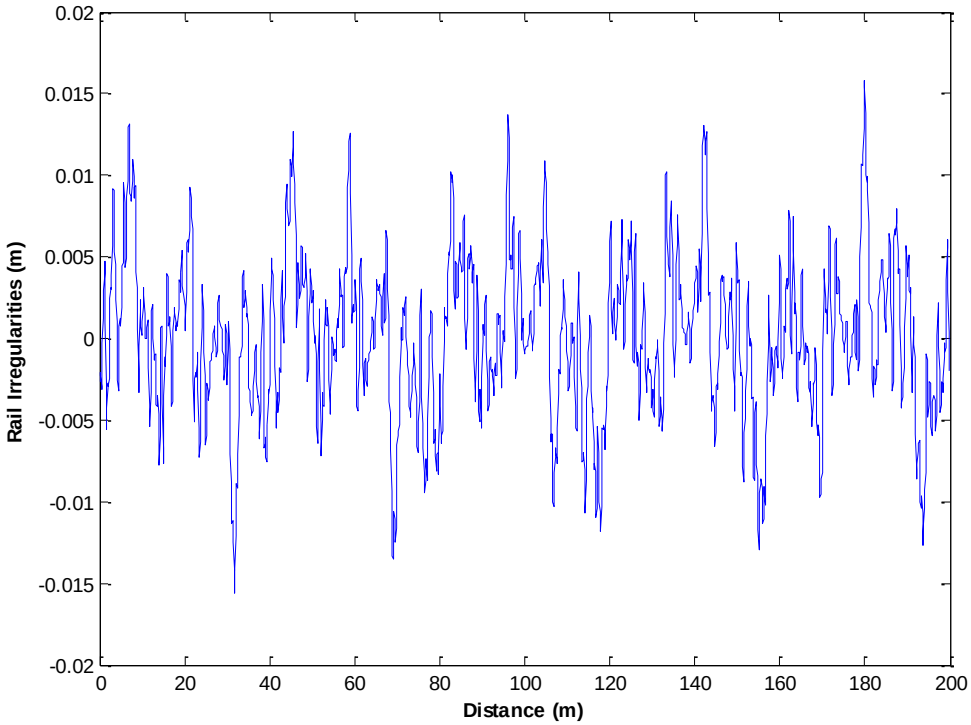

Figure 4.4 Rail irregularities proposed by SNCF for good state

4. 3. 2. Braun and Hellenbroich's Functions

Braun and Hellenbroich (1991) using PSD for road surface roughness proposed a PSD function for rail irregularities.

$$G(n) = G_{rr}(n_0)\left(\frac{n}{n_0}\right)^{-\omega} \qquad 4.13$$

Where n_0 = 1 / (2π) cycles/m and the exponent "ω" is constant between 3 and 4. For good track condition, the values of the roughness parameter $G(n_0) = 5 \times 10^{-7}$ m^3 and for poor condition $G(n_0) = 1 \times 10^{-9}$ m^3.

The PSD functions graphs for upper and lower limits are presented in Figure 4.5.

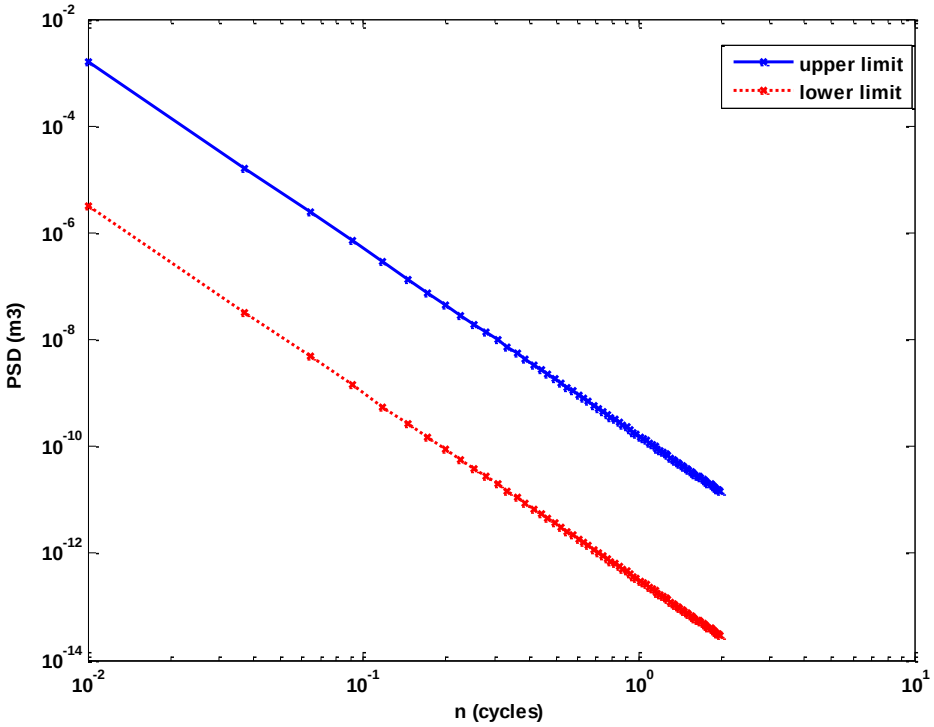

Figure 4.5 PSD function proposed by Braun and Hellenbroich

4. 3. 3. FRA formulations

The most widely used PSD formulations for track analysis and design were presented by FRA (Federal Railroad Administration). FRA collected a large database of track irregularities profiles in the United States. Based on the recorded rail profiles, Track is divided into six classes (1 the worst and 6 the best quality) to characterize the roughness of the rail and track quality. FRA suggested the following PSD functions for rail irregularities (Hamid et al. 1983).

$$G_{e,a}(n) = \frac{An_2^2(n^2 + n_1^2)}{n^4(n^2 + n_2^2)} \qquad 4.14$$

$$G_{c,g}(n) = \frac{An_2^2}{(n^2 + n_1^2)(n^2 + n_2^2)} \qquad 4.15$$

where "$G_{e,a}$" is PSD function for vertical profile and alignment and "$G_{c,g}$" is the PSD

function for cross level and gauge irregularities. "A" is the roughness parameter (in^2-cycle/ft.). "n_1" and "n_2" are defined as the break frequencies (cycle/ft.). The values of "A", "n_1", and "n_2" are different for track classes 1 to 6. The values of the constants are given in Table 4.1 (Wang 1984), (Hamid et al. 1983).

Table 4.1 Spectrum constants for different track classes defined by FRA(Wang 1984)

Irregularities	Parameter	Track Class					
		6	5	4	3	2	1
Profile	$A\times10^{-4}$	0.45	0.79	1.4	2.5	4.5	7.9
	$n1\times10^{-3}$	7.1	7.1	7.1	7.1	7.1	7.1
	$n2\times10^{-2}$	4.0	4.0	4.0	4.0	4.0	4.0
Cross level	$A\times10^{-4}$	0.34	0.50	0.74	1.1	1.6	2.3
	$n1\times10^{-3}$	7.1	7.1	7.1	7.1	7.1	7.1
	$n2\times10^{-2}$	4.0	4.0	4.0	4.0	4.0	4.0
Alignment	$A\times10^{-4}$	0.28	0.50	0.89	1.6	2.8	5.0
	$n1\times10^{-3}$	10.0	10.0	10.0	10.0	10.0	10.0
	$n2\times10^{-2}$	5.6	5.6	5.6	5.6	5.6	5.6
gage	$A\times10^{-4}$	0.28	0.50	0.89	1.5	2.8	5.0
	$n1\times10^{-3}$	8.9	8.9	8.9	8.9	8.9	8.9
	$n2\times10^{-2}$	7.1	7.1	7.1	7.1	7.1	7.1

Figure 4.6 to Figure 4.9 illustrate the power spectral density for vertical profile, cross level, alignment and gauge irregularities. The presented results are for track class 4 based on FRA classification.

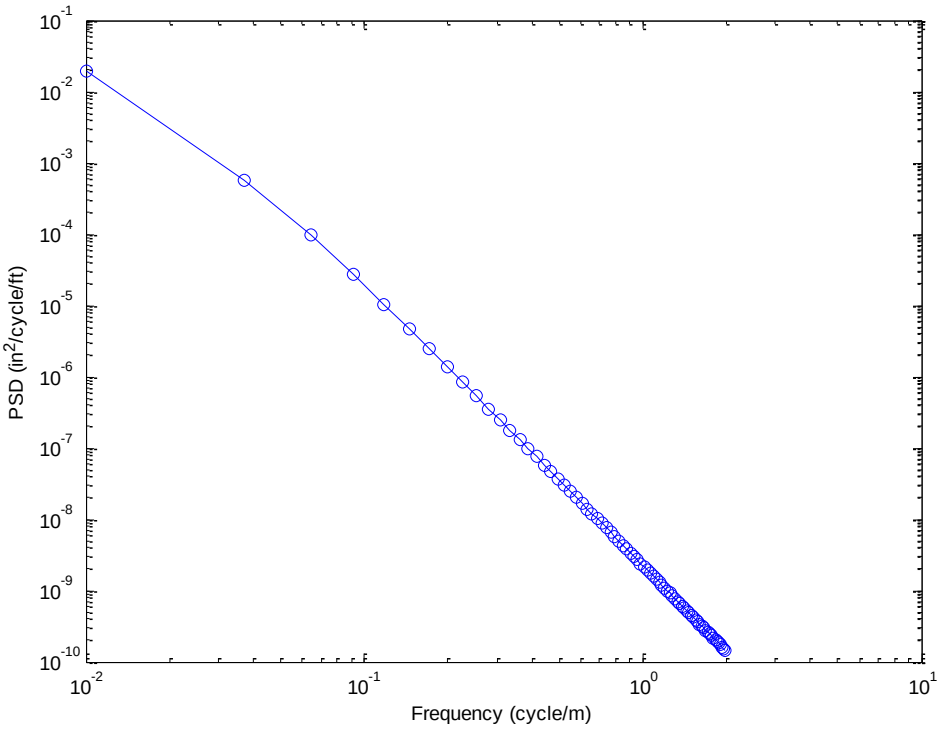

Figure 4.6 Vertical profile power spectral density for track class 4

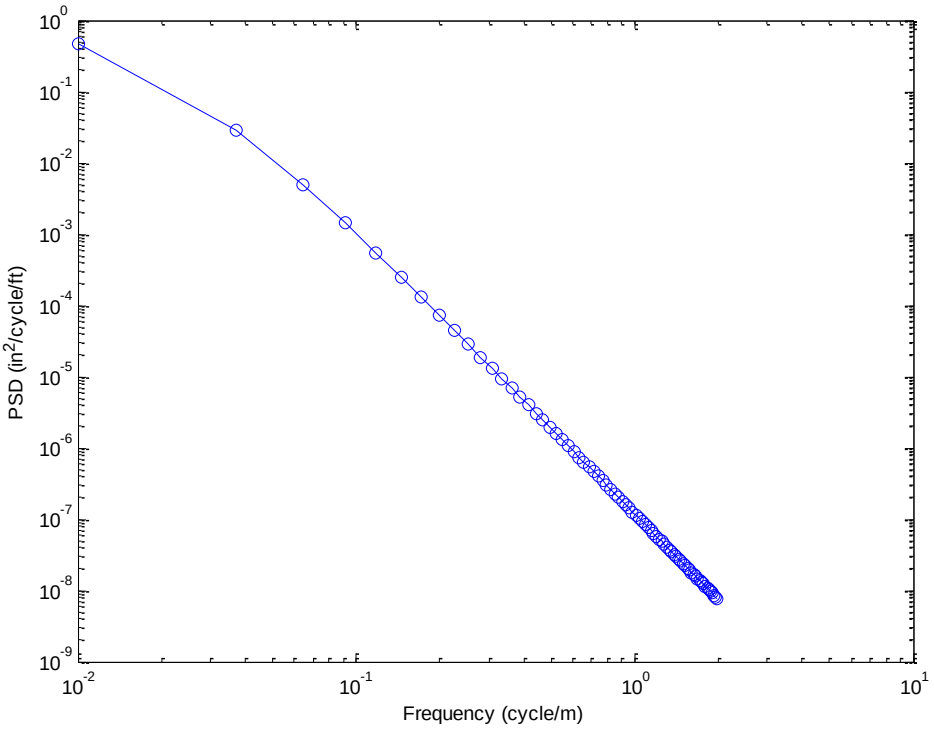

Figure 4.7 Cross level power spectral density for track class 4

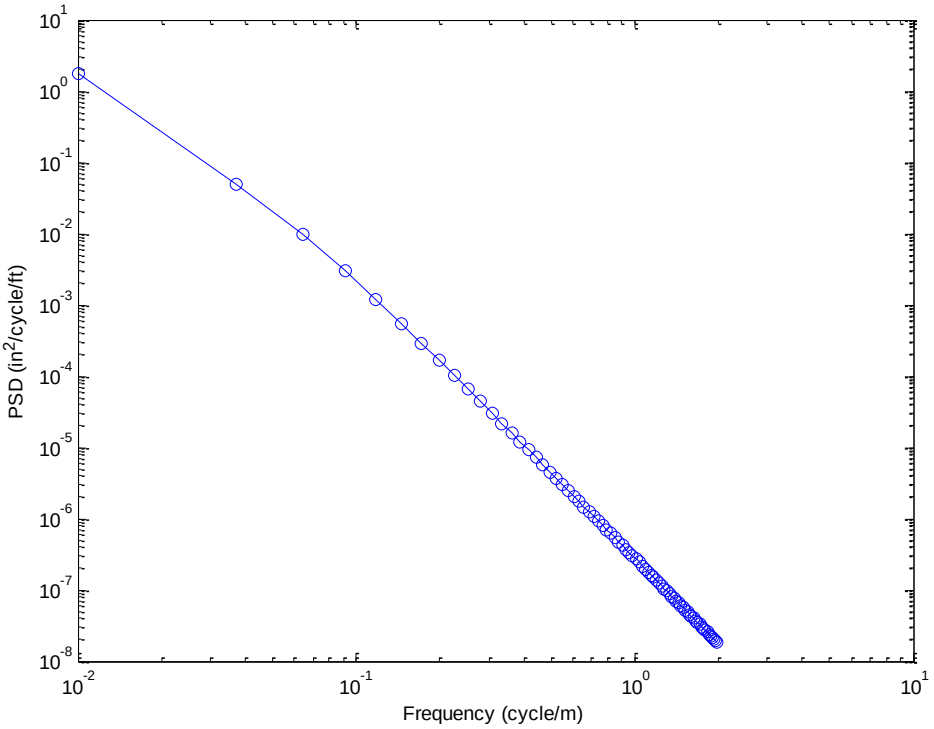

Figure 4.8 Alignment power spectral density for track class 4

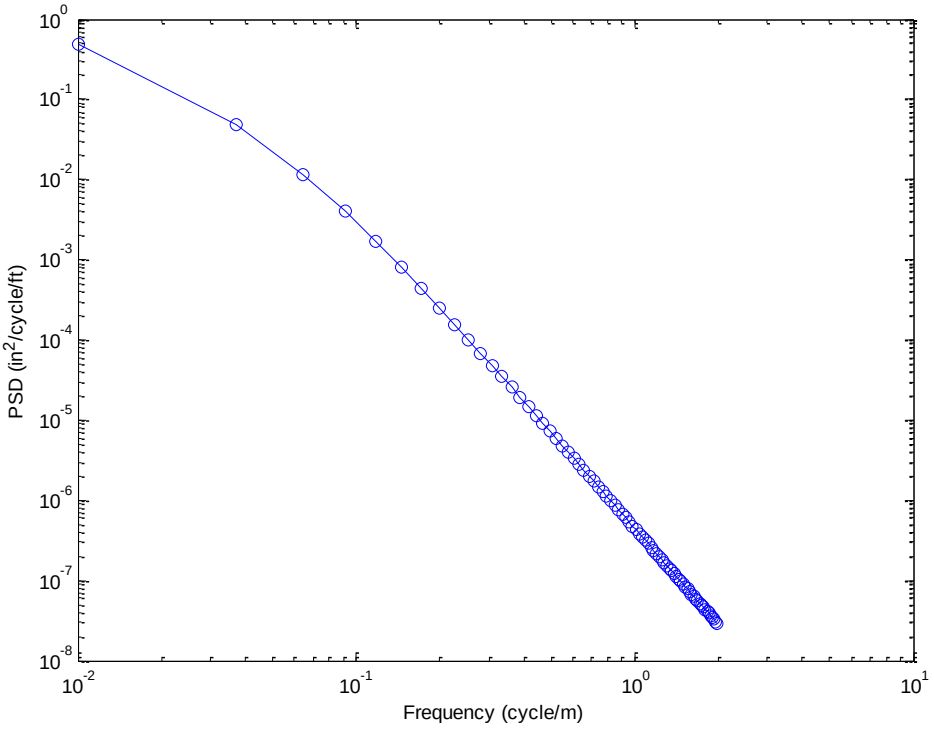

Figure 4.9 Gauge power spectral density for track class 4

If “R” and “L” refer to right and left rails, then the vertical (u_y) and lateral (u_z) irregularities are given as (Wang 1984)

$$u_{yR} = (\varepsilon_v + \frac{1}{2}\varepsilon_c)\ ,\ u_{zR} = (\varepsilon_a + \frac{1}{2}\varepsilon_g) \quad 4.16$$

$$u_{yL} = (\varepsilon_v - \frac{1}{2}\varepsilon_c)\ ,\ u_{zL} = (\varepsilon_a - \frac{1}{2}\varepsilon_g) \quad 4.17$$

In which “ε_v”, “ε_c”, “ε_a”and “ε_g” are vertical profile, cross level, alignment and gauge irregularities, respectively.

Figure 4.10 to Figure 4.13 show right and left rail vertical and lateral irregularities for track class 4. The same results for track class 6 are presented in Figure 4.14 to Figure 4.17. Comparing the figures of the two track classes clearly demonstrates that class 4 irregularities are about 30% higher than those of track class 6.

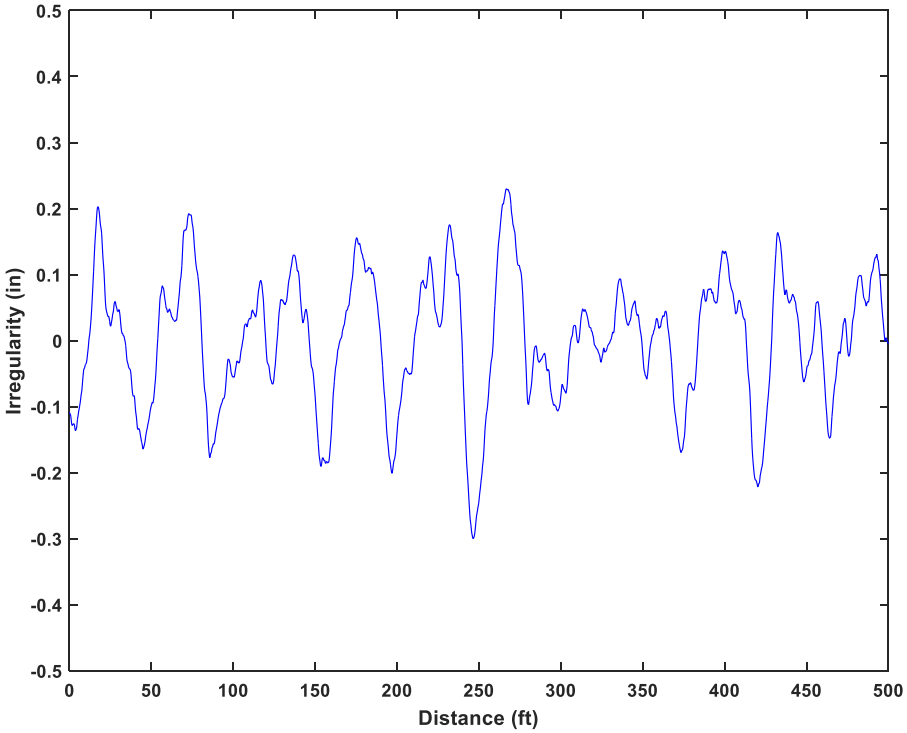

Figure 4.10 Right rail vertical irregularities for track class 4 (Vertical profile + ½cross level)

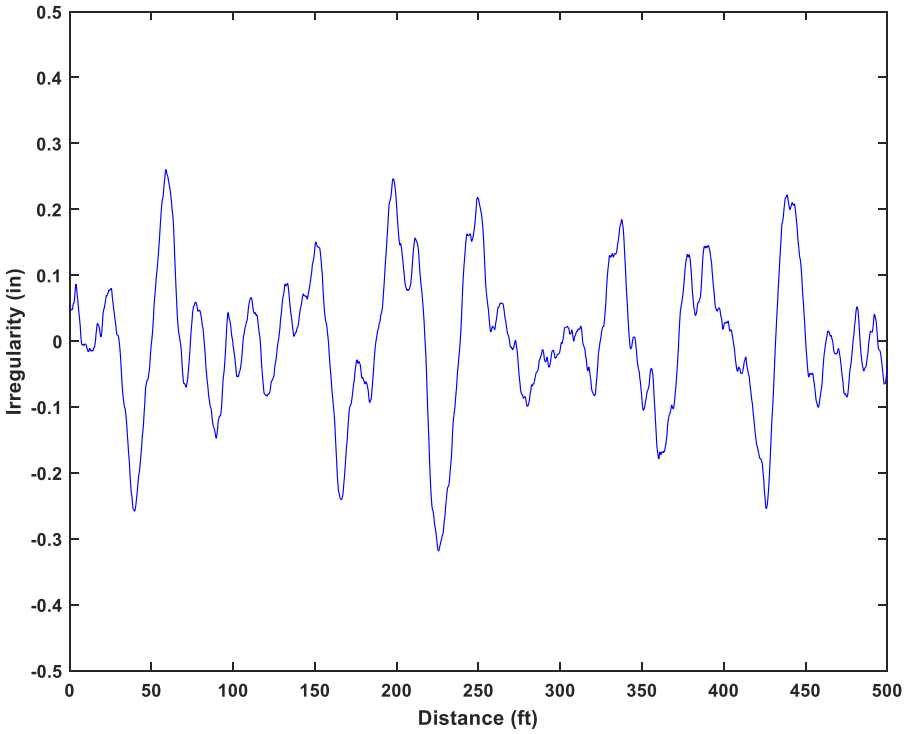

Figure 4.11 Left rail vertical irregularities for track class 4 (Vertical profile - ½cross level)

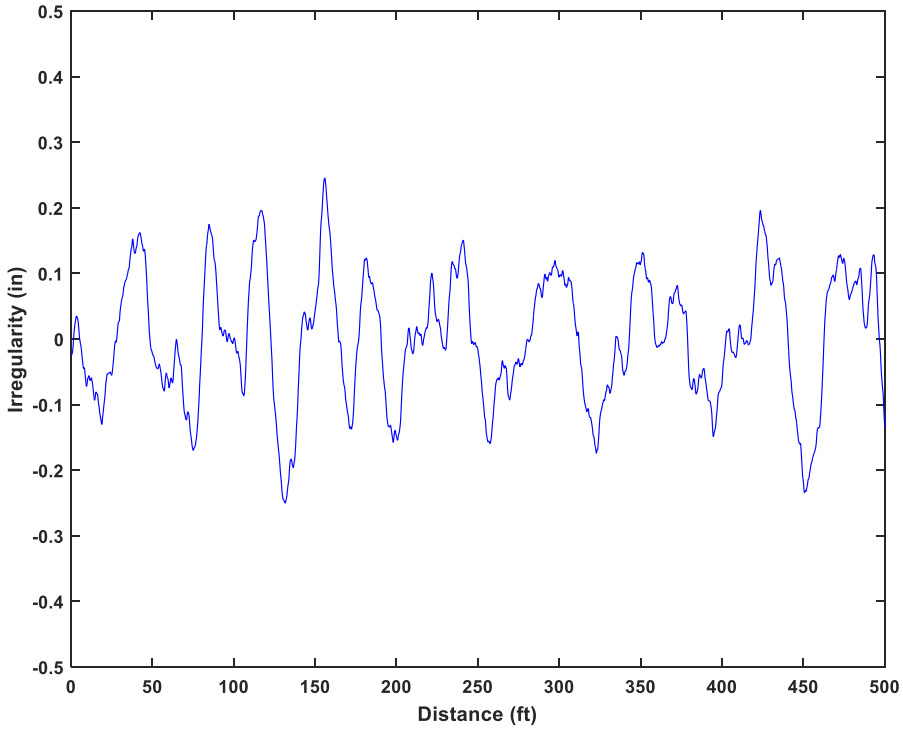

Figure 4.12 Right rail lateral irregularities for track class 4 (Alignment +½gage)

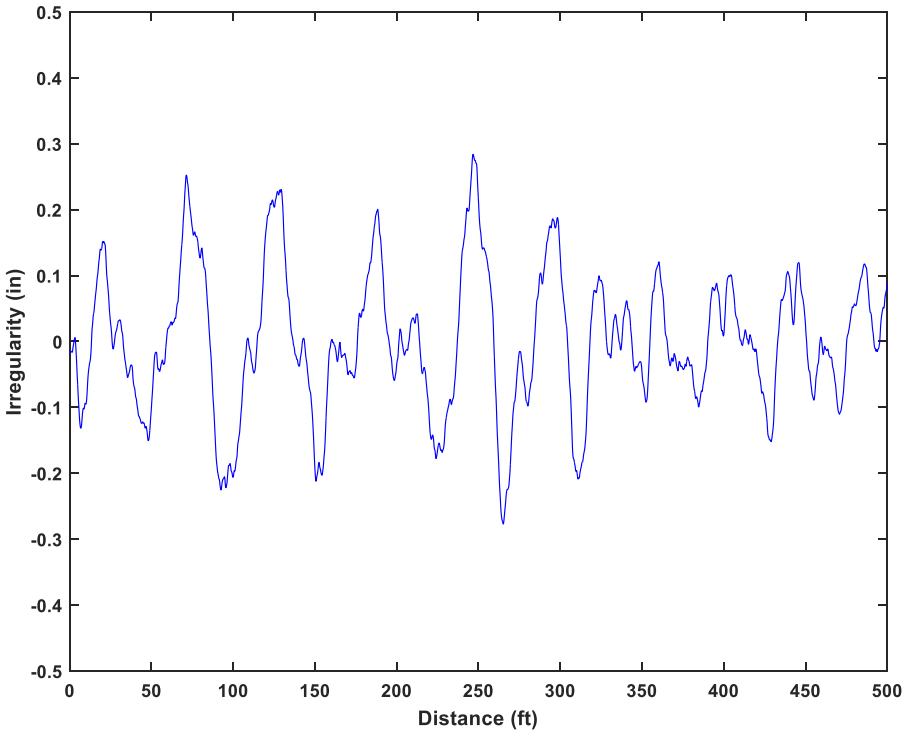

Figure 4.13 Left rail lateral irregularities for track class 4 (Alignment - ½gage)

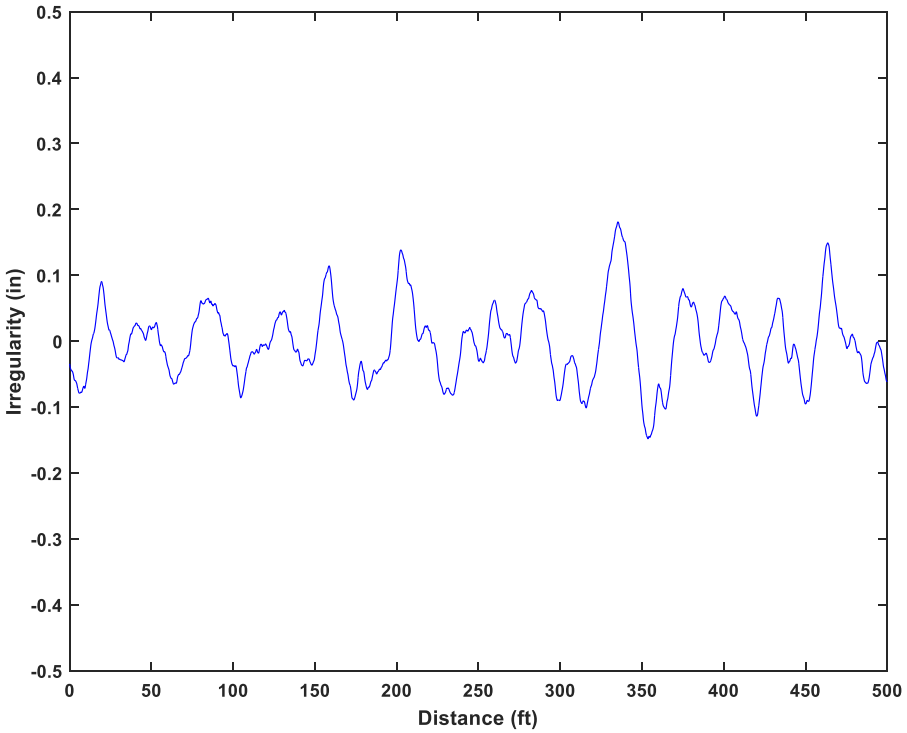

Figure 4.14 Right rail vertical irregularities for track class 6 (Vertical profile + ½ cross level)

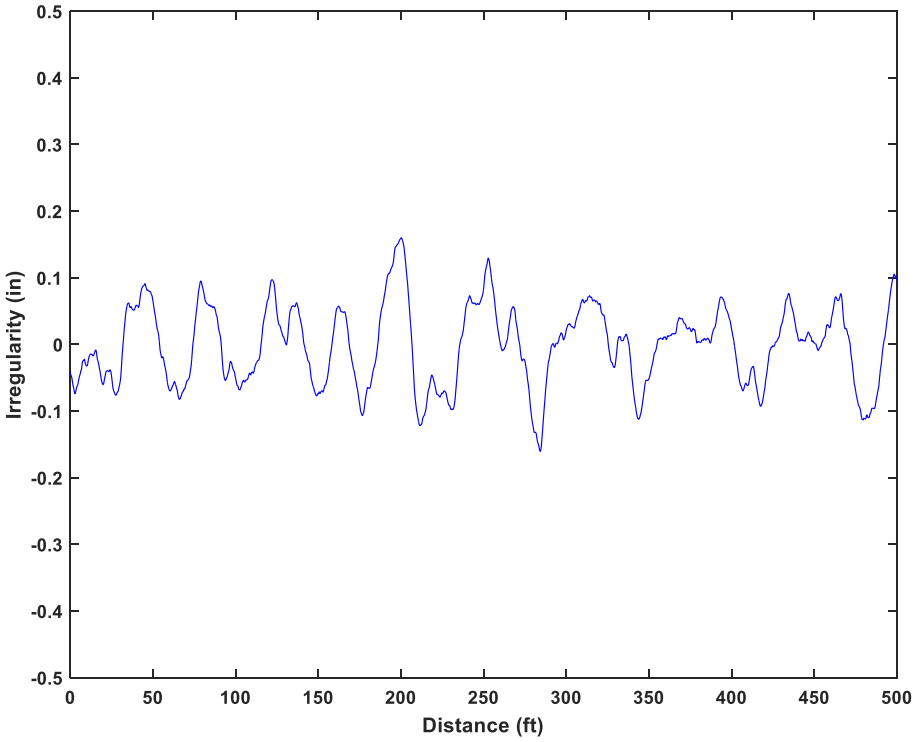

Figure 4.15 Left rail vertical irregularities for track class 6 (Vertical profile - ½cross level)

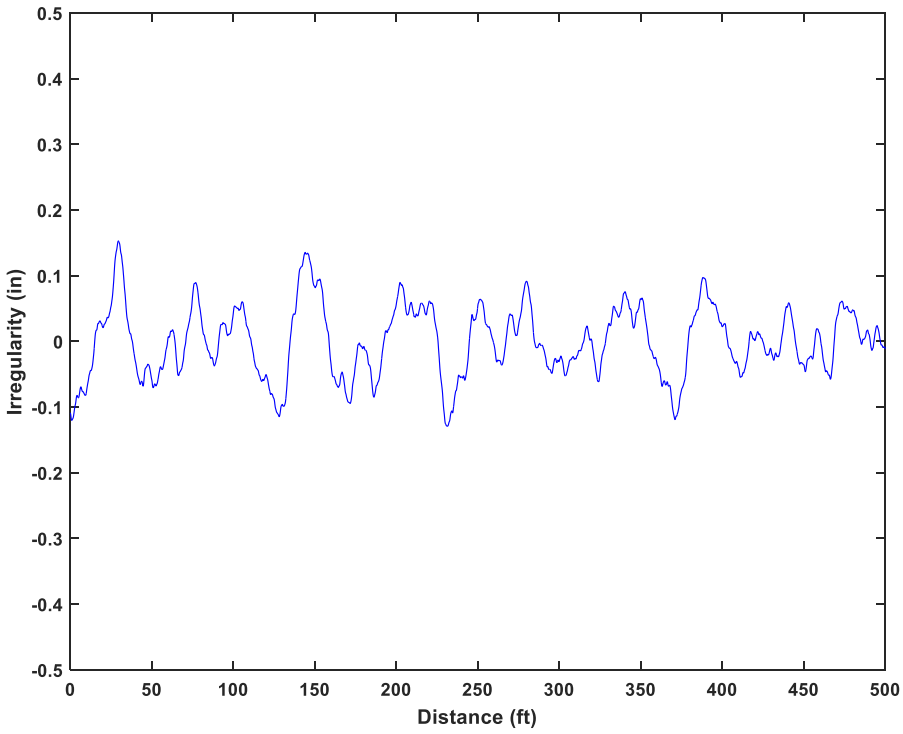

Figure 4.16 Right rail lateral irregularities for track class 6 (Alignment +½gage)

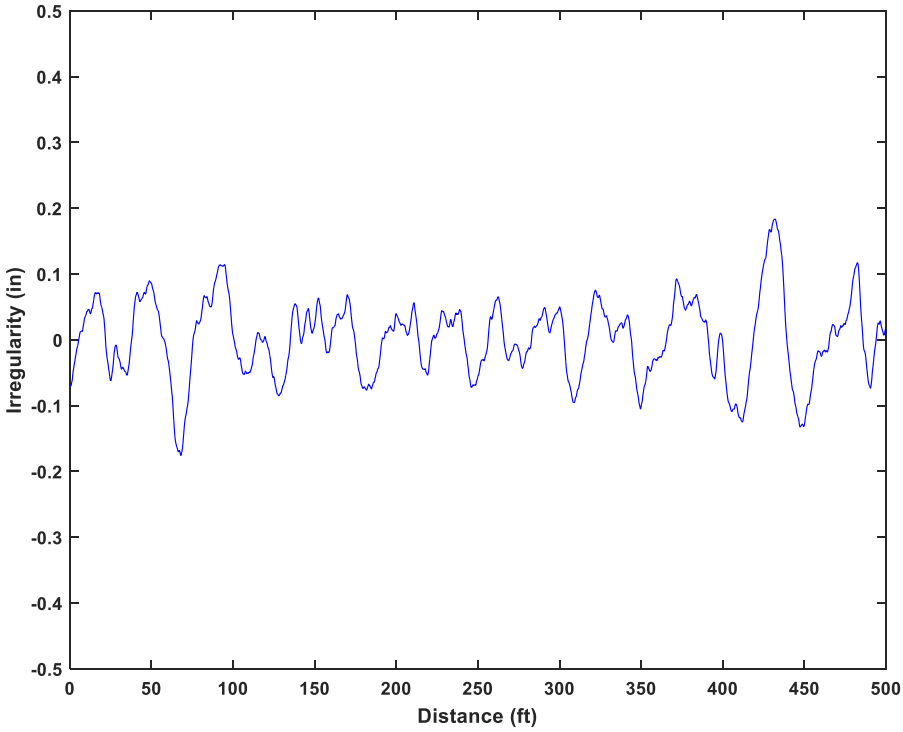

Figure 4.17 Left rail lateral irregularities for track class 6 (Alignment - ½gage)

4. 3. 4. Spectral Density Functions for High-Speed Track

As mentioned earlier, different PSD functions have been developed for different railroad tracks. Recently, there have been attempts to delve more into rail irregularities of high-speed tracks. Kang et al (2014) based on the measurements in Chinese high-speed tracks, developed the following PSD functions

$$G(f) = Af^{-k} \tag{4.18}$$

where "A" and "k" are constants defined for four categories of track quality. Table 4.2 shows the values of the constants for different sections.

Figure 4.18 to Figure 4.21 demonstrate vertical and lateral irregularities for right and left rail.

Table 4.2 Parameters of PSD for high-speed rail (Kang et al. 2014)

Irregularities	Section 1		Section 2		Section 3		Section 4	
	A	k	A	k	A	k	A	k
Gage	5.497×10^{-2}	0.828	5.070×10^{-3}	1.903	1.877×10^{-4}	4.594	-	-
Alignment	3.614×10^{-3}	1.727	4.368×10^{-2}	1.046	4.586×10^{-3}	2.093	-	-
Profile	3.951×10^{-3}	1.867	1.104×10^{-2}	1.535	7.563×10^{-4}	2.817	-	-
Cross-level	1.054×10^{-5}	3.389	3.558×10^{-3}	1.927	1.978×10^{-2}	1.364	3.948×10^{-4}	3.451

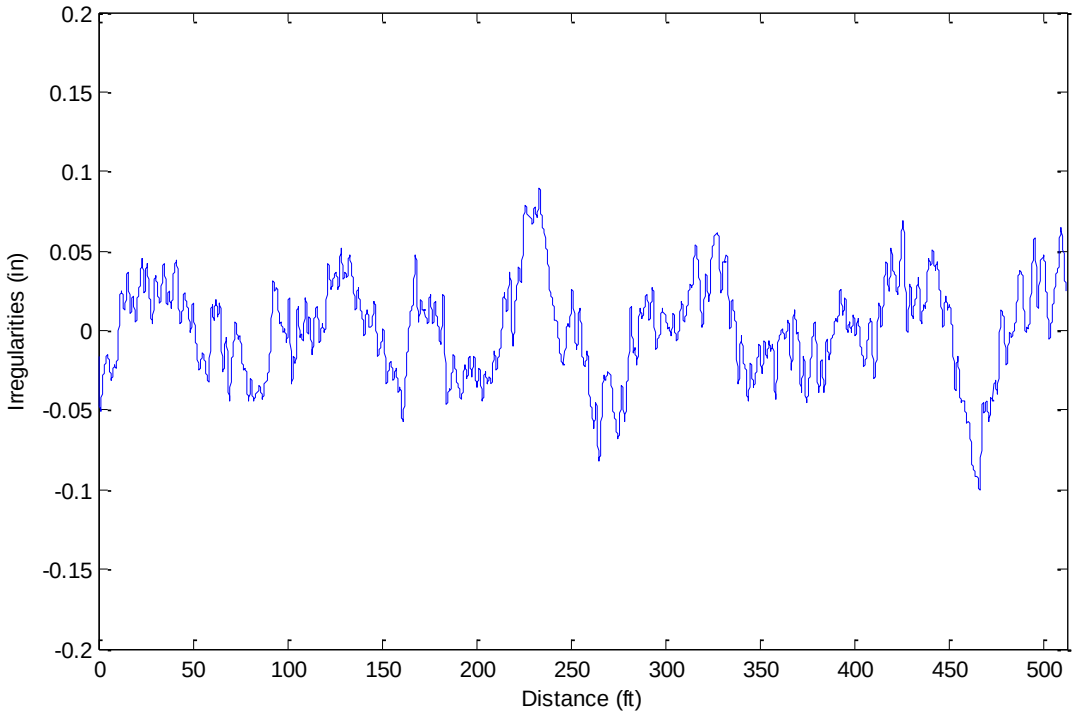

Figure 4.18 Right rail Vertical irregularities for HSR model (Vertical profile + ½cross level)

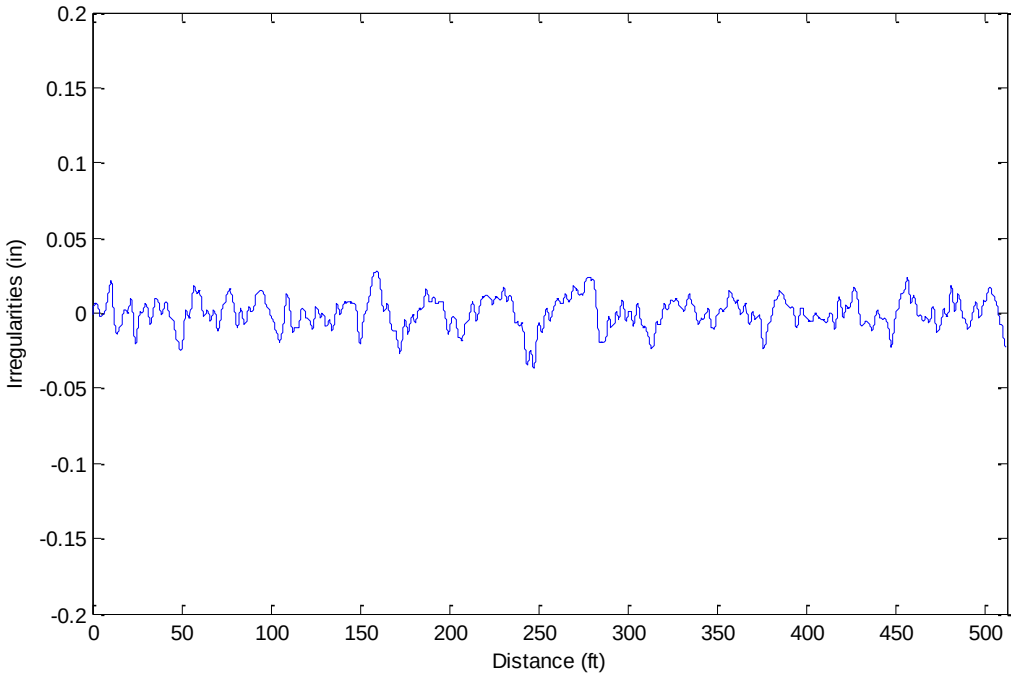

Figure 4.19 Left rail Vertical irregularities for HSR model (Vertical profile + ½cross level)

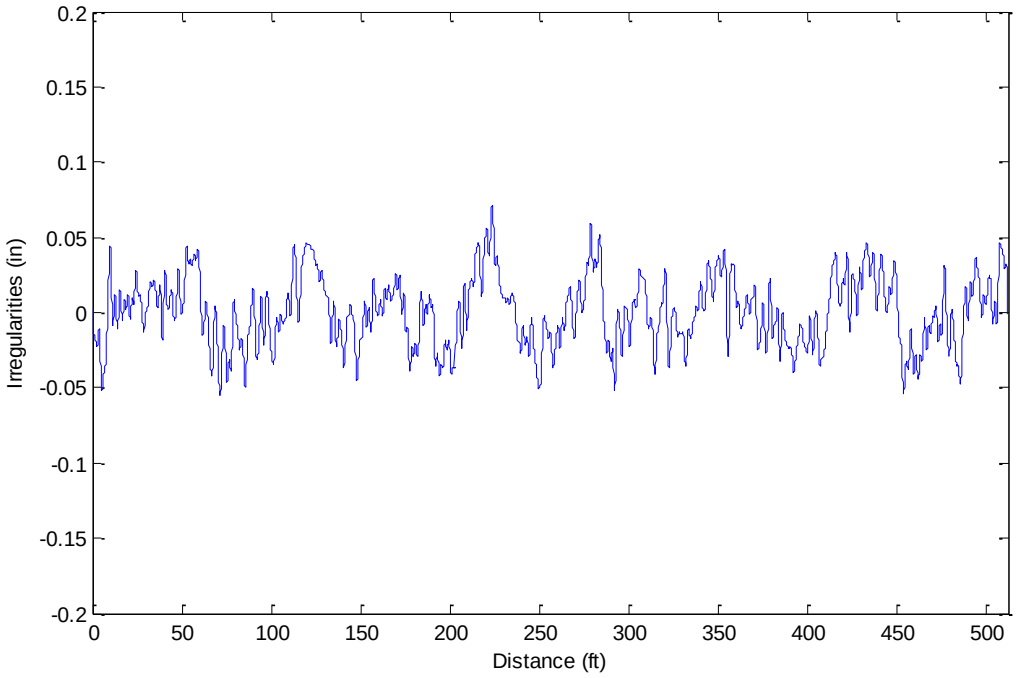

Figure 4.20 Right rail lateral irregularities for HSR model (Alignment + ½gage)

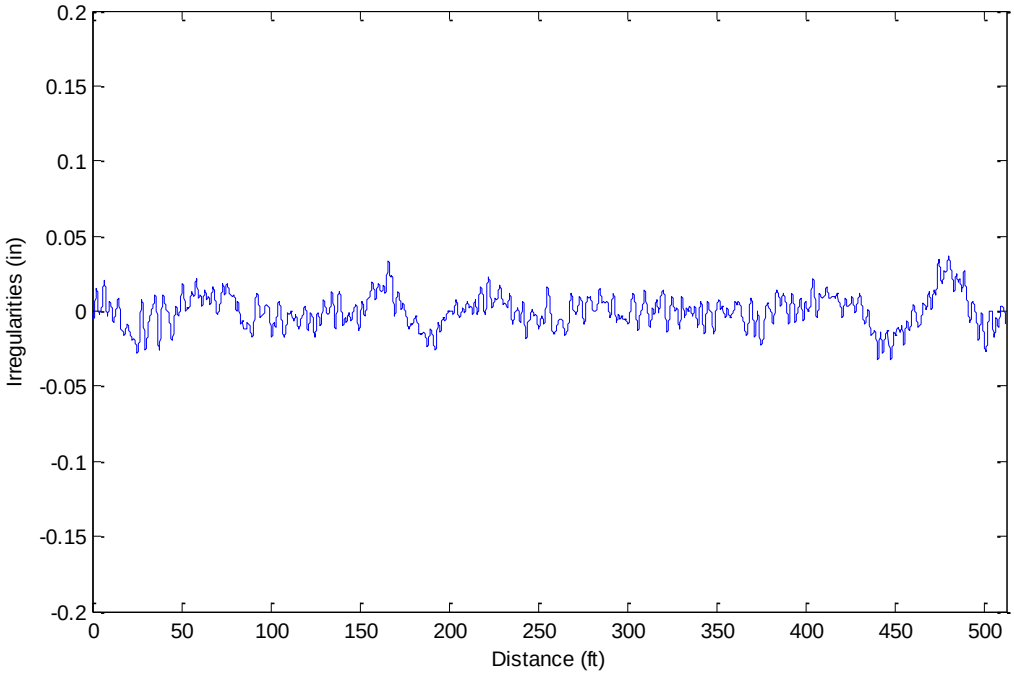

Figure 4.21 Left rail lateral irregularities for HSR model (Alignment - ½gage)

4. 4. Effect of rail irregularities on vehicle response

To demonstrate the effect of rail irregularities on rail response, the results presented in chapter 3, are repeated with applying random irregularities instead of half-staggered rectified sine displacement. Figure 4.22 show the irregularities used in the analyses. To clearly see the effects of irregularities, large amplitude of 2 cm for rail irregularities has been considered. The results are shown for PSD function proposed by Braun and Hellenbroich for poor condition.

Figure 4.23 to Figure 4.28 show the response of wheelset, bogie frames and car body to rail roughness. To illustrate the effect of irregularities, the results with and without irregularities for rail, bogie and car body depicted. As the figures suggests, the effect of irregularities on vehicle components displacements decreases from rail to car body. If irregularities are applies, the increase in maximum rail displacement is more than 87%

compared to smooth rail. For the same rail surface conditions, bogie displacement increases only 12% and car body maximum displacement does not show any increase.

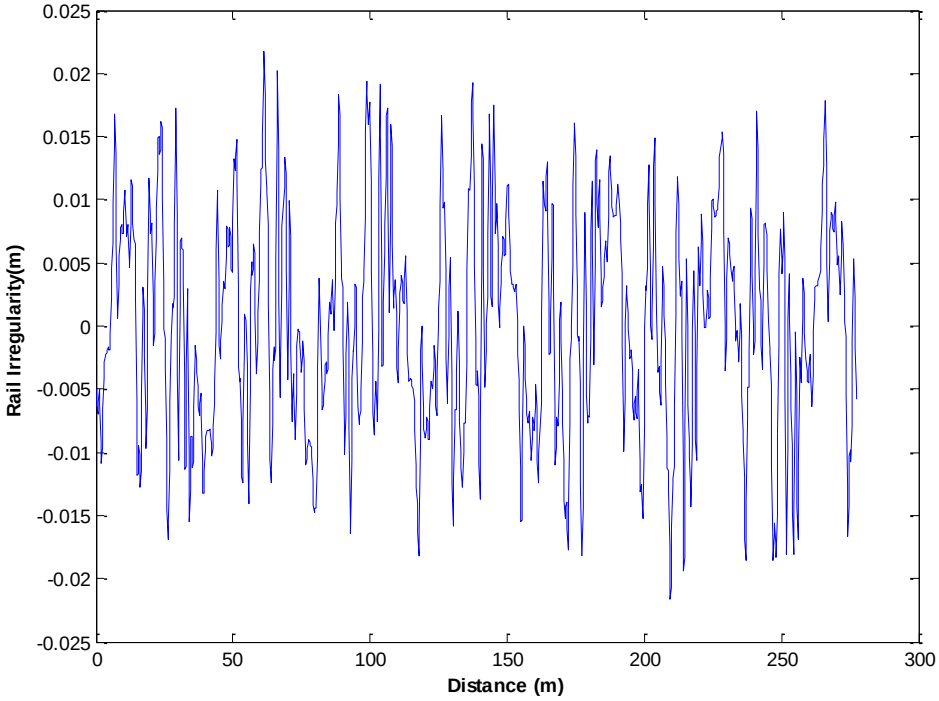

Figure 4.22 Rail irregularities, produced by PSD function proposed by Braun and Hellenbroich

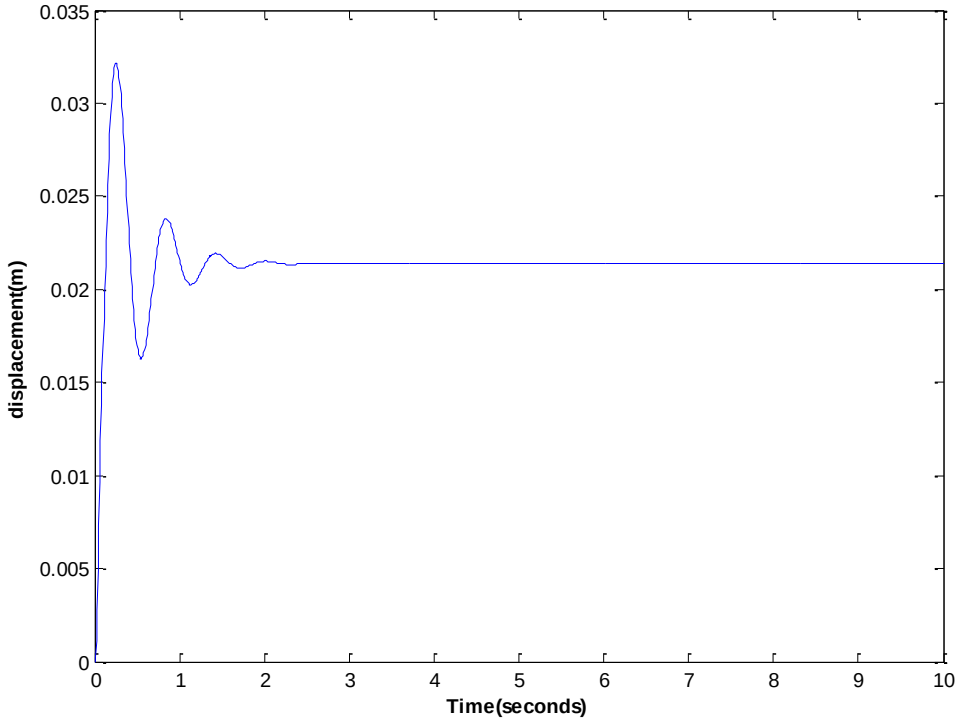

Figure 4.23 Rail displacement (No irregularities)

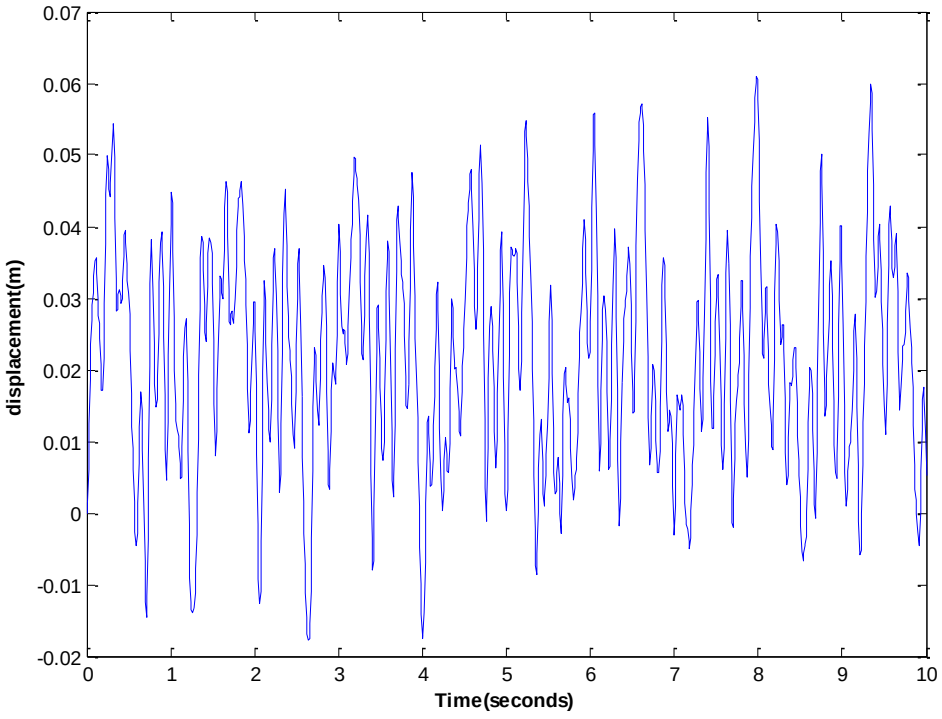

Figure 4.24 Rail displacement (with irregularities)

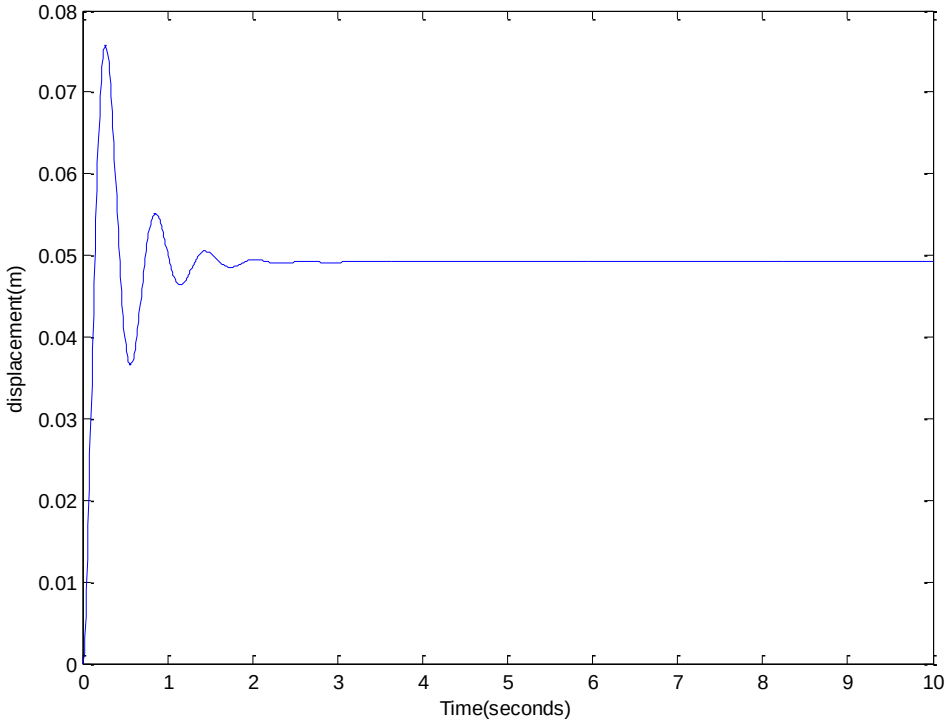

Figure 4.25 Bogie displacement (No irregularities)

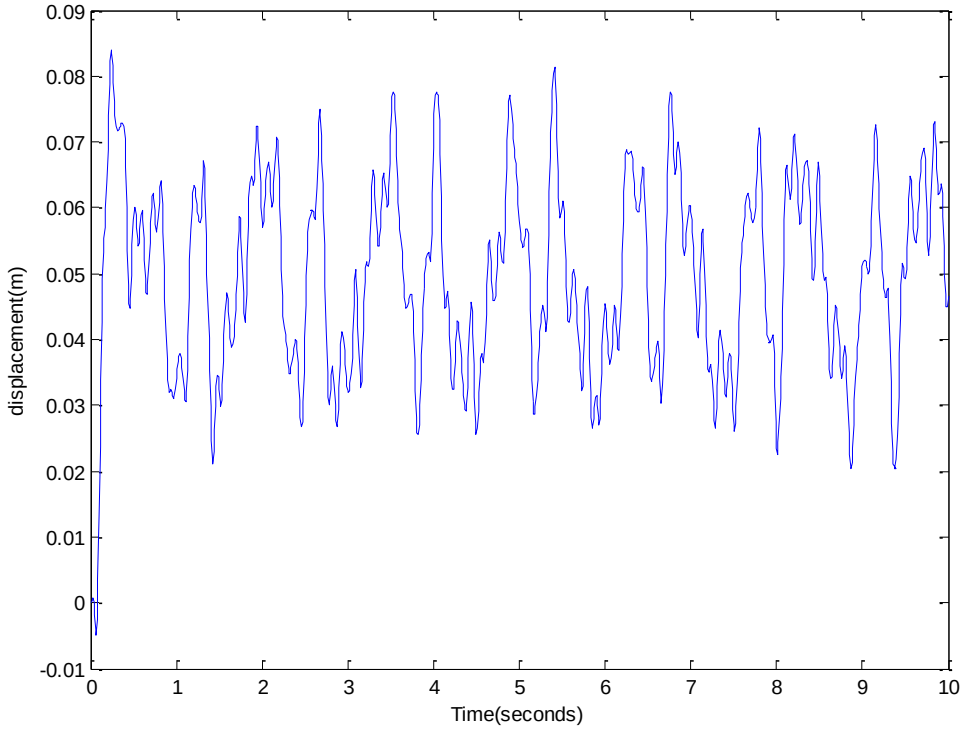

Figure 4.26 Bogie displacement (with irregularities)

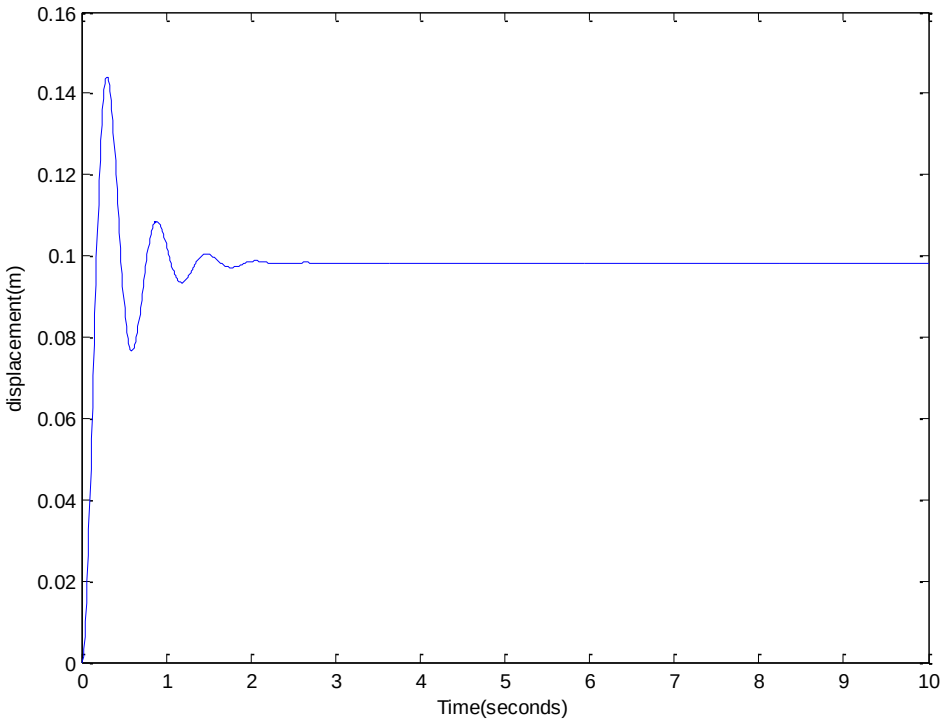

Figure 4.27 Car body displacement (No irregularities)

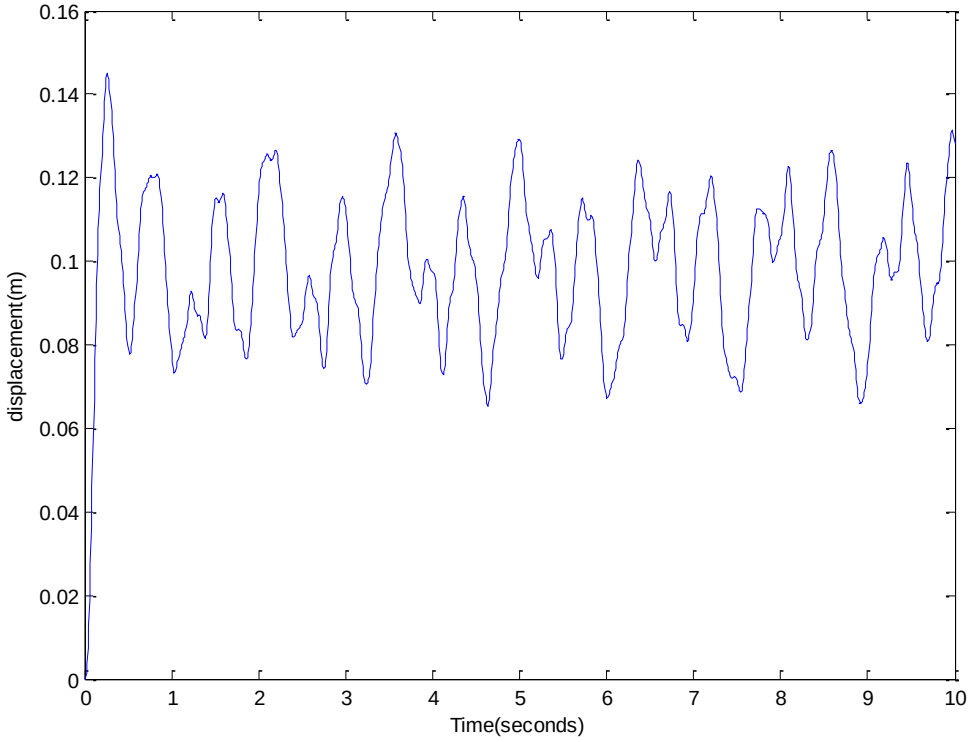

Figure 4.28 Car body displacement (with irregularities)

5. Track model

The purpose of this chapter is to describe the modeling procedure of railroad track. This chapter are divided into two parts; first the modeling the interaction of vehicle and track and second, the modeling of track components and track substructure. Then the differential equations of the whole vehicle-track system are formed and solved by numerical solutions.

5. 1. Train-Track Interaction

The vehicle-track interaction is an important issue in railroad track dynamics. Due to high contact pressure at wheel-rail interface, most rail and track failures occur or initiate from this point. Based on the results of an analysis of causes of major train derailment conducted by Liu et al. (Liu et al. 2012), rail defects are responsible for almost 20% of derailments and more than 30% of derailed vehicles. On the other hand, creep, fatigue and slippage at the rail surface make the modeling of train-track interaction important.

The contact theory of rail and wheel evolved during the past decades. The early models considered Coulomb's friction on the rail interface and a concentrated load applied on rail and wheel interface. Hence, fatigue, as well as wear phenomenon cannot be calculated by the early models (Kalker 1991).

Due to limitations of single-point contact theory, Carter (Carter F.W 1926), assuming rail as infinite half-space and wheel as moving cylinder developed two-dimensional solution for rail-wheel interaction problem. However, this model only considers rolling forces and it fails to simulate lateral forces. Therefore, three-dimensional theories have been developed to address this problem. One model that successfully describes the vehicle-track interaction is Hertz contact theory which states that the elastic deformation of the steel of the wheel and the rail creates an elliptic area. The dimensions of the contact ellipse are

determined by the normal force on the area, while the ratio of ellipse axes "a" and "b" depends on the main curvatures of the wheel and rail profiles. Figure 5.1 shows the contact area between wheel and rail (Esveld 2001)

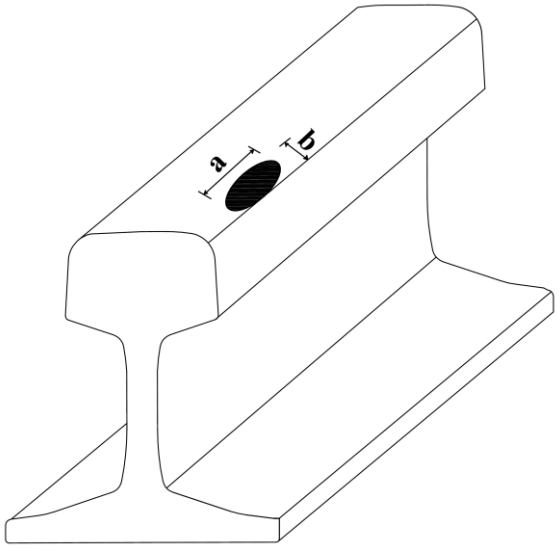

Figure 5.1Wheel-rail contact area

To find the wheel-rail contact force, the contact stiffness in vertical direction "$K_{w/r}^{v}$" needs to be defined first. It depends on the wheel load and wheel and rail properties.

$$K_{w/r}^{v} = \sqrt[3]{\frac{3E^2P\sqrt{R_{wheel}R_{rail}}}{2(1-\nu^2)^2}} \qquad 5.1$$

where "R_{wheel}" and "R_{rail}" are wheel rolling radius and rail head radius, respectively and "P" is the static wheel load. Note that it is assumed that wheel and rail have the same modulus of elasticity, "E" and Poisson ratio," ν".

The wheel-rail contact force" $F_{w/r}^{v}$" then can be determined by

$$F_{w/r}^{v} = K_{w/r}^{v}(y_{wheel} - y_{rail}) \qquad 5.2$$

"y_{wheel}" and "y_{rail}" are wheel and rail vertical displacements. The contact force is

nonlinear elastic and tensionless which means that if $(y_{wheel} - y_{rail})$<0 or wheel and rail are not in contact then the force will be equal to zero. It should be noted that in the above formula, rail irregularities will be added to the rail displacement (Esveld 2001).

The lateral interaction between rail and wheel is modeled by a linear spring at the contact point (Wu & Thompson 2002). As Thompson reported the lateral contact spring is 20% stiffer than the vertical spring (Thompson 1990). Figure 5.2 is the illustration of Hertz vertical and horizontal springs.

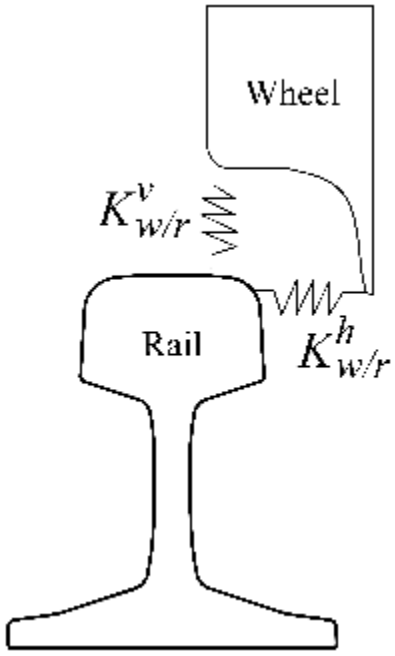

Figure 5.2 Wheel-rail interaction

5. 2. Track model

Track model consists of rail, rail pad, sleeper and ballast. Rail is modeled as beam elements with six degrees of freedom at each node. So the nodal displacements of rail can be expressed as a vector

$$[U] = [u_1 \quad v_1 \quad w_1 \quad \alpha_1 \quad \beta_1 \quad \gamma_1 \quad u_2 \quad v_2 \quad w_2 \quad \alpha_2 \quad \beta_2 \quad \gamma_2]^T \qquad 5.3$$

Where “u”, “v” and “w” represent displacements in “x”, “y” and “z” directions and “α”, “β” and “γ” denote rotations around “x”, “y” and “z” axes. Subscripts 1 and 2 indicate first (left) and second (right) node of a beam element. (Chopra 2011)

First order Lagrange shape functions (N_1 and N_2) and cubic Hermitian interpolation functions (N_3, N_4, N_5, N_6) are used to describe the axial and flexural deflections of beam elements. Note that ‘e’ is the distance from the left node of the beam and ‘l’ is the beam element length. To simplify the solution, the length of beam elements is equal to the distance between two adjacent sleepers. Figure 5.3, shows the beam element and its DOFs.

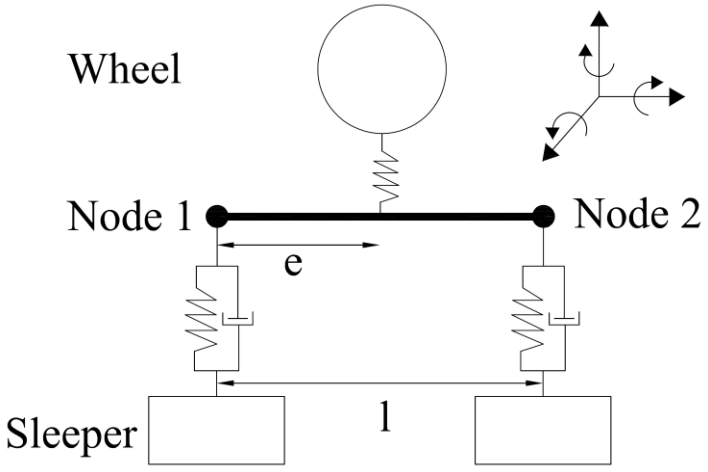

Figure 5.3 beam element’s DOFs

The interpolation vectors for the axial, vertical, lateral, and torsional displacements are given as follows:

$$[N_u] = [N_1 \quad 0 \quad 0 \quad 0 \quad 0 \quad 0 \quad N_2 \quad 0 \quad 0 \quad 0 \quad 0 \quad 0]^T$$

$$[N_v] = [0 \quad N_3 \quad 0 \quad 0 \quad 0 \quad N_4 \quad 0 \quad N_5 \quad 0 \quad 0 \quad 0 \quad N_6]^T \qquad 5.4$$

$$[N_w] = [0 \quad 0 \quad N_3 \quad 0 \quad -N_4 \quad 0 \quad 0 \quad 0 \quad N_5 \quad 0 \quad -N_6 \quad 0]^T$$

$$[N_\alpha] = [0 \quad 0 \quad 0 \quad N_1 \quad 0 \quad 0 \quad 0 \quad 0 \quad 0 \quad N_2 \quad 0 \quad 0]^T$$

where

$$N_1(e) = 1 - \frac{e}{l}$$

$$N_2(e) = \frac{e}{l}$$

$$N_3(e) = 1 - 3\left(\frac{e}{l}\right)^2 + 2\left(\frac{e}{l}\right)^3$$

$$N_4(e) = e\left(1 + \left(\frac{e}{l}\right)^2 - 2\left(\frac{e}{l}\right)\right)$$

$$N_5(e) = 3\left(\frac{e}{l}\right)^2 - 2\left(\frac{e}{l}\right)^3$$

$$N_6(e) = e\left(\left(\frac{e}{l}\right)^2 - \left(\frac{e}{l}\right)\right)$$

The displacements of a rail element can be related to nodal DOFs as follows

$$u(x) = [N_u][U]$$

$$v(x) = [N_v][U]$$

$$w(x) = [N_w][U] \qquad 5.5$$

$$\alpha(x) = [N_\alpha][U]$$

The mass matrix for the beam element can be written in the following form:

$$[M] = \frac{\overline{m}}{420}\begin{bmatrix} 140 & 0 & 0 & 0 & 0 & 0 & 70 & 0 & 0 & 0 & 0 & 0 \\ & 156 & 0 & 0 & 0 & 22l & 0 & 54 & 0 & 0 & 0 & -13l \\ & & 156 & 0 & -22l & 0 & 0 & 0 & 54 & 0 & 13l & 0 \\ & & & 140r^2 & 0 & 0 & 0 & 0 & 0 & 70r^2 & 0 & 0 \\ & & & & 4l^2 & 0 & 0 & 0 & -13l & 0 & -3l^2 & 0 \\ & & & & & 4l^2 & 0 & 13l & 0 & 0 & 0 & -3l^2 \\ & & & & & & 140 & 0 & 0 & 0 & 0 & 0 \\ & & & & & & & 156 & 0 & 0 & 0 & -22l \\ & & & & & & & & 156 & 0 & 22l & 0 \\ & & & & & & & & & 140r^2 & 0 & 0 \\ & & & & & & & & & & 4l^2 & 0 \\ Sym & & & & & & & & & & & 4l^2 \end{bmatrix} \qquad 5.6$$

The mass matrix of rail, composed of mass matrices of right and left rails, then can be expressed as the following formula:

$$M_R = \begin{bmatrix} M_{rr} & 0 \\ 0 & M_{lr} \end{bmatrix} \tag{5.7}$$

where "M_{rr}" and "M_{lr}" are mass matrices of right and left rails, respectively. Since each beam element has 12 degrees of freedom, the total DOFs of mass matrix for right and left rails would be 24.

The same procedure and shape function are utilized to find the stiffness matrix of beam elements. The stiffness matrix of the beam element reads:

$$[K]=\begin{bmatrix}
\frac{AE}{l} & 0 & 0 & 0 & 0 & 0 & -\frac{AE}{l} & 0 & 0 & 0 & 0 & 0 \\
 & \frac{12EI_z}{l^3} & 0 & 0 & 0 & \frac{6EI_z}{l^2} & 0 & -\frac{12EI_z}{l^3} & 0 & 0 & 0 & \frac{6EI_z}{l^2} \\
 & & \frac{12EI_y}{l^3} & 0 & -\frac{6EI_y}{l^2} & 0 & 0 & 0 & -\frac{12EI_y}{l^3} & 0 & -\frac{6EI_y}{l^2} & 0 \\
 & & & \frac{GJ}{l} & 0 & 0 & 0 & 0 & 0 & -\frac{GJ}{l} & 0 & 0 \\
 & & & & \frac{4EI_y}{l} & 0 & 0 & 0 & \frac{6EI_y}{l^2} & 0 & \frac{2EI_y}{l} & 0 \\
 & & & & & \frac{4EI_z}{l^2} & 0 & -\frac{6EI_z}{l^2} & 0 & 0 & 0 & \frac{2EI_z}{l} \\
 & & & & & & \frac{AE}{l} & 0 & 0 & 0 & 0 & 0 \\
 & & & & & & & \frac{12EI_z}{l^3} & 0 & 0 & 0 & -\frac{6EI_z}{l^2} \\
 & & & & & & & & \frac{12EI_y}{l^3} & 0 & \frac{6EI_y}{l^2} & 0 \\
 & & & & & & & & & \frac{GJ}{l} & 0 & 0 \\
 & & & & & & & & & & \frac{4EI_y}{l} & 0 \\
Sym & & & & & & & & & & & \frac{4EI_z}{l}
\end{bmatrix} \tag{5.8}$$

To apply damping to the system, proportional or Rayleigh damping is used. It is assumed that the matrix of damping is proportional to a linear combination of mass and stiffness

$$[C] = c_1[M] + c_2[K] \tag{5.9}$$

where 'c_1' and 'c_2' are constant coefficients which show the effect of mass and stiffness on damping. The values of "c_1" and "c_2" are 400 and 4×10^7 as used by Naeimi et al. (Naeimi et al. 2015).

Sleepers are modeled as rigid bodies. Rail is linked to sleepers by rail pads modeled by linear springs and dashpots. Although previous studies showed that rail fastening behavior is not linear but an average value of stiffness produces good results (Sadeghi et al. 2015). Ballast material is considered to be rigid body which is connected to the subgrade. Since ballast is composed of coarse aggregate materials, the shear stiffness and damping or the effects of the ballast granules interlocking is also considered in the modeling.

To find the effective mass and stiffness of ballast material, it is assumed that sleeper load distributes in conical area in ballast. The mass and stiffness of ballast will be calculated considering ballast in the cone area and the "outside ballast" is not considered in dynamic analysis. The so-called "ballast pyramid model" first developed by Ahlbeck et al (Ahlbeck et al. 1978). In this research, the pattern of load distribution in ballast was considered for non-overlapping pyramids of stress distribution in two neighboring sleepers. The equations, proposed for mass and stiffness of the ballast for non-overlapping cones, are: (Zhai et al. 2004) and (Esmaeili et al. 2014)

$$M_{bal} = \rho_{bal} h_{bal} \left[l_e l_{slp} + \left(l_e + l_{slp}\right) h_{bal} \tan\theta + \frac{4}{3} {h_{bal}}^2 \tan^2\theta \right] \qquad 5.10$$

$$K_{bal} = \frac{2\left(l_e - l_{slp}\right)\tan\theta}{ln\left[\left(\frac{l_e}{l_{slp}}\right).\left(l_{slp} + 2h_{bal}\tan\theta\right)/\left(l_e + 2h_{bal}\tan\theta\right)\right]} E_{bal} \qquad 5.11$$

where "ρ_{bal}" stands for the density of the ballast, "E_{bal}" is the elastic modulus of ballast, and "h_{bal}" represents the thickness of the ballast layer. "l_e" indicates the effective support range of a half sleeper," l_{slp}" is the width of sleeper and "θ" shows the ballast stress distribution angle. Figure 5.4 depicts the effective volume of ballast used in ballast pyramid model. (Zhai et al. 2004)

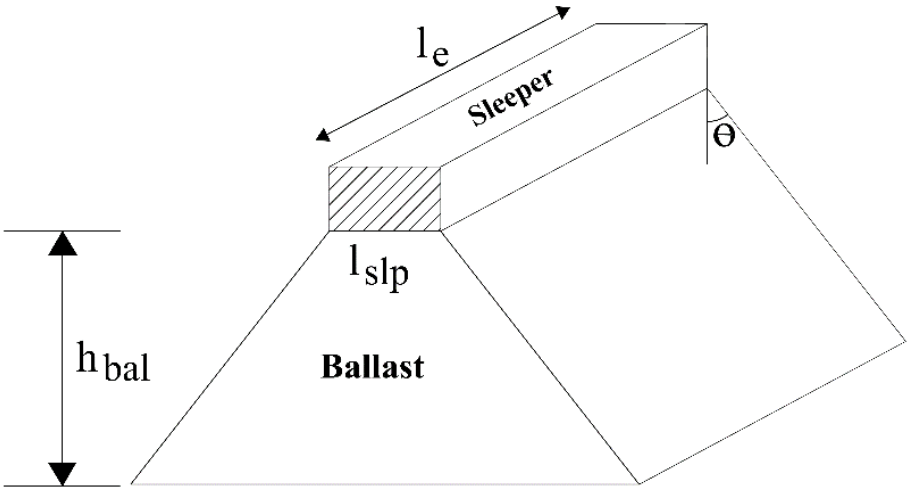

Figure 5.4 Stress Distribution in Ballast

The interaction matrix of track subsystem consisting rail, sleepers and ballast can be written as follows

$$[I] = \begin{bmatrix} R & R/S & 0 \\ S/R & S & S/B \\ 0 & B/S & B \end{bmatrix} \quad 5.12$$

"R", "S" and "B" represents the matrices of mass, stiffness or damping for rail, sleeper and ballast, respectively. Non-diagonal members represent the interaction between elements.

By the assemblage of the mass, stiffness and damping matrices of the track components, the dynamic equation of the track subsystem is presented in the following format.

$$[M^{tr}]\{\ddot{U}^{tr}\} + [C^{tr}]\{\dot{U}^{tr}\} + [K]\{U^{tr}\} = \{P^{tr}\} \quad 5.13$$

The subscript "tr" shows that each matrix is formed by assembling track components matrices. Figure 5.5 shows the process of numerical solution to the vehicle-track problem.

Table 5.1 Track Parameters

Notation	Parameter	Value	Unit
M_r	Rail Mass Per Unit Length	60	Kg/m
M_{slp}	Sleeper Mass	250	Kg
l_s	Sleeper spacing	0.6	m
l_e	Effective support length of half sleeper	0.95	m
l_{slp}	Sleeper width	0.27	m
K_{pad}	Rail Pad Stiffness	4×107	N/m
C_{pad}	Rail pad Damping	1.3×105	N.s/m
h_{bal}	Ballast thickness	0.45	m
E_{bal}	Elastic Modulus of Ballast	1×108	N/m^2
K_{int}	Ballast Shear Stiffness	7.8×107	N/m
C_{int}	Ballast Shear Damping	8×104	N.s/m
θ	Ballast stress distribution angle	35	degree
C_{bal}	Ballast Damping	8×104	N.s/m
E_{sub}	Elastic Modulus of Subgrade	8×107	N/m^2
C_{sub}	Subgrade Damping	5.5×104	N.s/m
$K_{w/r}$	Hertz Spring Constant	1.1×1011	N/m^2
R_{rail}	Rail head radius	0.3	m

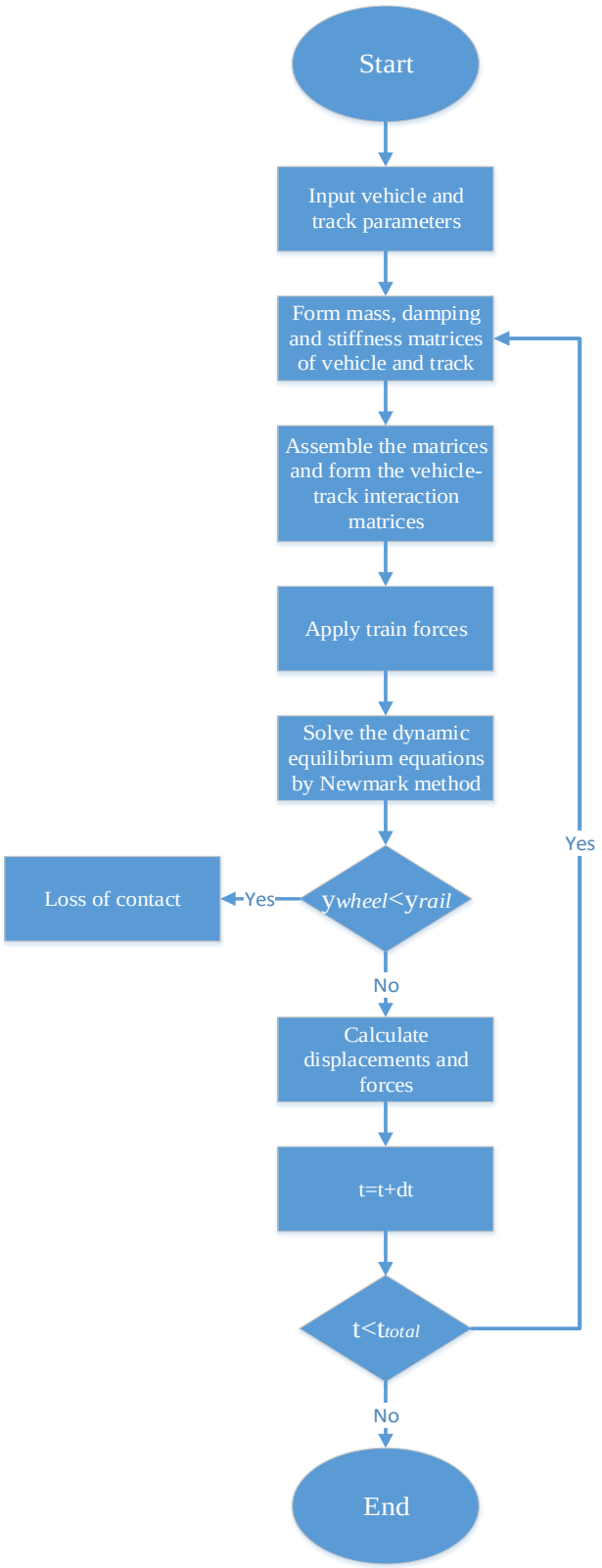

Figure 5.5 Algorithm of train-track numerical analysis

5. 3. Bridge model

Bridge is considered as Euler-Bernoulli beam and the procedure of modeling is the same as explained for the rail model. The Hermitian and first order Lagrange shape functions are utilized. The bridge bearings are modeled as vertical springs and dampers as well as, lateral springs and dampers to account for friction and lateral resistance of girder-pier connection. Figure 5.6 shows the vehicle-track-bridge model used in this study. The parameters in numerical study are also shown in Table 5.2. The total vehicle-track-bridge equations of motion can be formulated

$$\begin{bmatrix} M_{veh} & 0 & 0 \\ 0 & M_{tra} & 0 \\ 0 & 0 & M_{brg} \end{bmatrix} \begin{Bmatrix} \ddot{u}_{veh} \\ \ddot{u}_{tra} \\ \ddot{u}_{brg} \end{Bmatrix} + \begin{bmatrix} C_{veh} & C_{veh/tra} & 0 \\ C_{tra/veh} & C_{tra} & C_{tra/brg} \\ 0 & C_{brg/tra} & C_{brg} \end{bmatrix} \begin{Bmatrix} \dot{u}_{veh} \\ \dot{u}_{tra} \\ \dot{u}_{brg} \end{Bmatrix} + \begin{bmatrix} K_{veh} & K_{veh/tra} & 0 \\ K_{tra/veh} & K_{tra} & K_{tra/brg} \\ 0 & K_{brg/tra} & K_{brg} \end{bmatrix} \begin{Bmatrix} u_{veh} \\ u_{tra} \\ u_{brg} \end{Bmatrix} = \begin{Bmatrix} F_{veh} \\ F_{tra} \\ F_{brg} \end{Bmatrix} \quad 5.14$$

where "M", "C" and "K" are matrices of mass, damping and stiffness of each sub-systems. Since the beam elements are used to find the behavior of bridge, the matrix form is similar to rail formulations. The mass matrix of bridge is a diagonal matrix of order n×n

$$M_{brg} = diag[m_{eb1} \quad m_{eb2} \quad \dots \quad m_{ebn}] \quad 5.15$$

where "n" is the number of beam elements.

Bridge element stiffness can be formed by following formula

$$K_{brg} = diag[k_{eb1} \quad k_{eb2} \quad \dots \quad k_{ebn}] \quad 5.16$$

"k_{ebi}" shows the stiffness of ith bridge element.

$$k_{ebi} = \int_0^l E_{brg} I_{brg} N_{bi}''^T N_{bi}'' dx + \sum_{j=1}^{m} k_{sub} N_{bj}^T N_{bj} \quad 5.17$$

Note that "m" is the total number of subgrade spring located on ith bridge element. "l" is

the length of bridge element and "x" is local coordinate system measured from the left node of bridge element. Figure 5.7 shows the bridge element.

The track structure is connected to bridge by ballast material so the submatrix "$K_{tra/brg}$" should demonstrate the interaction of bridge and ballast.

$$K_{tra/brg} = diag[k_{bb1} \quad k_{bb2} \quad \dots \quad k_{bbn}] \tag{5.18}$$

where "k_{bbi}" is the stiffness matrix of the ballast-bridge interaction on the ith bridge element. "k_{bbi}" can be formulates as follows

$$k_{bbi} = [-k_{sub}N_{b1}^T \quad -k_{sub}N_{b2}^T \quad \dots \quad -k_{sub}N_{bn}^T] \tag{5.19}$$

"n" is the total number of concentrated mass considered in the bridge element.

Incorporating viscous dampers makes the process of forming damping matrix easy and the formulas are similar to the resulted stiffness matrices

$$C_{brg} = diag[c_{eb1} \quad c_{eb2} \quad \dots \quad c_{ebn}] \tag{5.20}$$

"c_{ebi}" shows the damping of ith bridge element.

$$c_{ebi} = \int_0^l E_{brg}\, I_{brg} N_{bi}^T N_{bi} dx + \sum_{j=1}^{m} c_{sub} N_{bj}^T N_{bj} \tag{5.21}$$

and the submatrix "$C_{tra/brg}$" has the following form

$$C_{tra/brg} = diag[c_{bb1} \quad c_{bb2} \quad \dots \quad c_{bbn}] \tag{5.22}$$

where "c_{bbi}" is the damping matrix of ballast-bridge interaction on ith bridge element. "c_{bbi}" can be formulates as follows

$$c_{bbi} = [-c_{sub}N_{b1}^T \quad -c_{sub}N_{b2}^T \quad \dots \quad -c_{sub}N_{bn}^T] \tag{5.23}$$

In which "c_{sub}" is damping coefficient of ballast material.

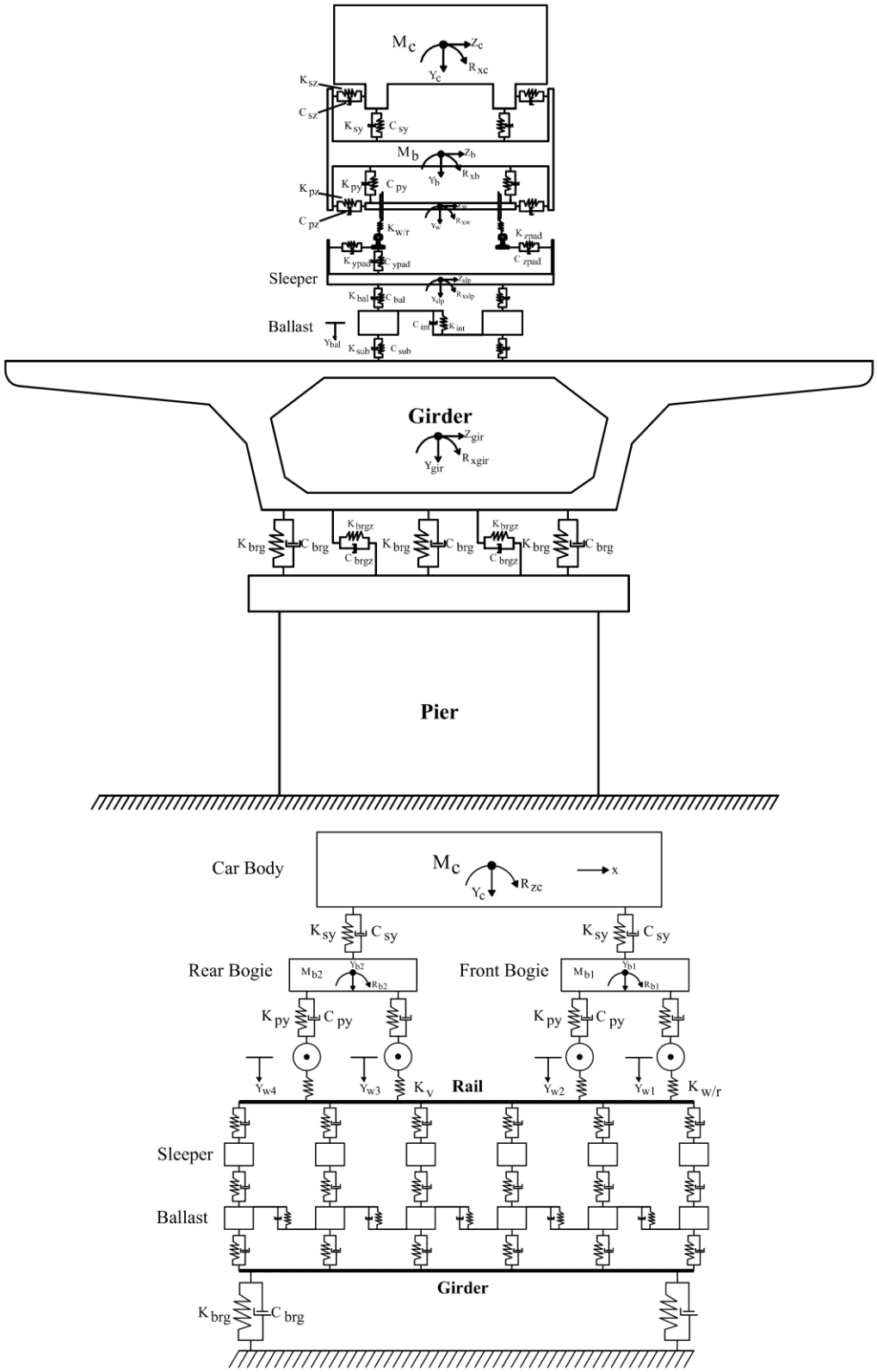

Figure 5.6 Vehicle-track-bridge model

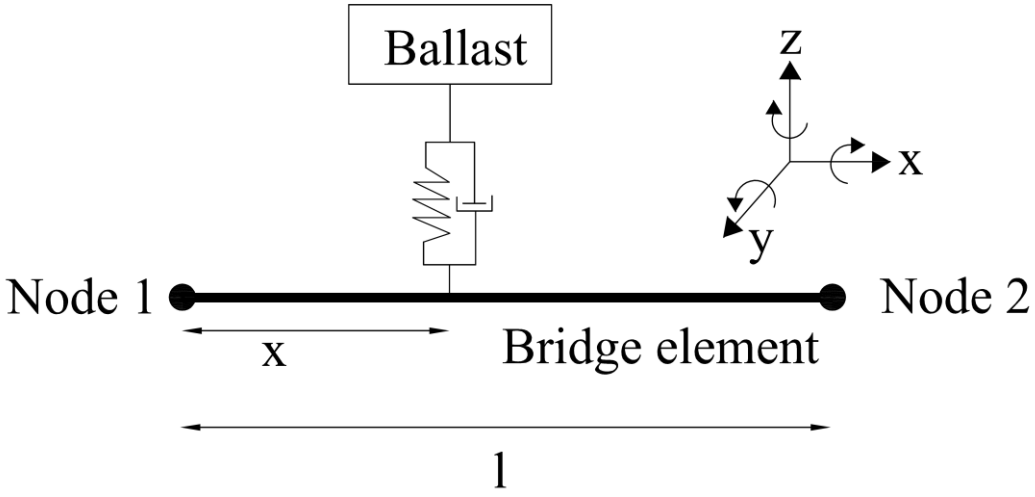

Figure 5.7 Bridge element

Table 5.2 Bridge parameters

Notation	Parameter	Value	Unit
M_{brg}	Bridge Mass Per Unit Length	4×10^{10}	Kg/m
E_{brg}	Elastic Modulus of bridge	3.5×10^{10}	N/m^2
G_{brg}	Shear modulus of bridge	1.5×10^{10}	N/m^2
I_{xbrg}	moment of inertia about x-axis	50	m^4
I_{ybrg}	moment of inertia about y-axis	20	m^4
I_{zbrg}	moment of inertia about z-axis	120	m^4
K_{lbrg}	Lateral stiffness of elastic bearing	5×10^{8}	N/m
K_{vbrg}	Vertical stiffness of elastic bearing	5×10^{9}	N/m
C_{lbrg}	Lateral damping of elastic bearing	1×10^{5}	N.s/m
C_{vbrg}	Vertical damping of elastic bearing	1×10^{6}	N.s/m

Table 5.3 shows the first five natural frequencies of the bridge. The process of calculating the Eigen values or the natural frequencies of the system has been explained in chapter 3.

Table 5.3 The first five natural frequency of the bridge

Mode No.	Natural Frequency (Hz)
1	5.865
2	6.121
3	6.899
4	7.250
5	10.704

5. 4. Solution to Train-Track-Bridge Model

By the assemblage of the mass, stiffness and damping matrices of the vehicle and track elements, the dynamic equation of the whole system will be formed

$$[M^t]\{\ddot{U}^t\} + [C^t]\{\dot{U}^t\} + [K^t]\{U^t\} = \{P(x,t)\} \tag{5.24}$$

Where, $[M^t]$, $[C^t]$ and $[K^t]$ are the matrices representing mass, damping and the stiffness of total train- track coupling system, respectively. "P" indicates the vector of the load induced by the passage of the train.

To solve the dynamic equation of motion, the Newmark integration method is used. This method, developed by Newmark (1959), is based on the assumption that the acceleration varies linearly between two instants of time. So if the track response is known at time "t", the response at time "t+dt" can be calculated.

$$\begin{aligned}
&\{U_{t+dt}\} = [\bar{K}]\big[\{F_{t+dt}\} + [M]\big(b_1\{U_t\} + b_3\{\dot{U}_t\} + b_4\{\ddot{U}_t\}\big) + \\
&[C]\big(b_2\{U_t\} + b_5\{\dot{U}_t\} + b_6\{\ddot{U}_t\}\big)\big] \\
&\{\dot{U}_{t+dt}\} = b_2(\{U_{t+dt}\} - \{U_t\}) - b_5\{\dot{U}_t\} - b_6\{\ddot{U}_t\} \\
&\{\ddot{U}_{t+dt}\} = b_1(\{U_{t+dt}\} - \{U_t\}) - b_3\{\dot{U}_t\} - b_4\{\ddot{U}_t\}
\end{aligned} \tag{5.25}$$

where $[\bar{K}] = (b_1[M] + b_2[C] + [K])^{-1}$ and "b_1" to "b_6" are constants as follows (Chopra 2011).

$$b_1 = \frac{1}{\alpha dt^2}\,, \qquad b_2 = \frac{\beta}{\alpha dt}\,, \qquad b_3 = \frac{1}{\alpha dt}$$
$$b_4 = \frac{1}{2\alpha} - 1\,, \qquad b_5 = \frac{\beta}{\alpha} - 1\,, \qquad b_6 = \frac{dt}{2}\left(\frac{\beta}{\alpha} - 2\right) \tag{5.26}$$

The Newmark integration is an implicit method which means the proper values of "α" and "β" leads to unconditionally stable solution. For this reason, the values of "α" and "β" are considered 0.25 and 0.5 throughout the analyses.

Note that the time step in numerical analyses is assumed 0.0001s.

5. 5. Track Model validation

To show the validity of the numerical solution and formulation procedure, the response of a beam under a series of moving loads from current solution was compared with the results from theoretical solutions for the same problem. Figure 5.8 shows a series of concentrated loads on an Euler-Bernoulli beam as a validation model. The beam is rested on an elastic foundation and track stiffness and damping have been modeled by a continuous layer of springs with stiffness "K_p" and dampers with constant "C_p" in unit length. The loads are moving at the speed "v".

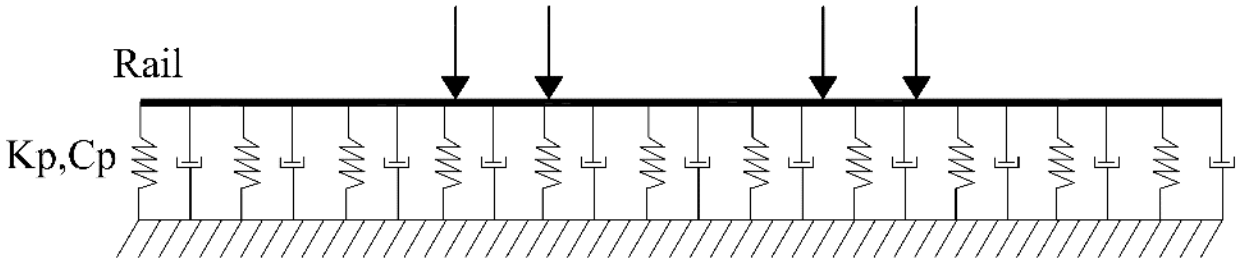

Figure 5.8 Euler-Bernoulli beam on elastic foundation

Table 5.4 Parameters of validation model

Notation	Parameter	Value	Unit
F	Wheel-set load	15	ton
K_p	Rail support stiffness	2×10^6	N/m
C_p	Rail support damping	25000	N.s/m
v	Moving loads' speed	20	m/s
l	Length of rail	36	m
E	Rail's elastic modulus	2×10^{11}	N/m^2
I_r	Rail's moment of inertia	3×10^{-5}	m^4
m	Beam mass of a unit length	50	Kg/m

Using the above assumptions, the governing differential equations of beam on elastic foundation can be determined (Hussein & Hunt 2006)

$$EI_r \frac{\partial^4 w_r(x,t)}{\partial x^4} + m_r \frac{\partial^2 w_r(x,t)}{\partial t^2} + k_p w_r(x,t) + c_p \frac{\partial w_r(x,t)}{\partial t} = P_0 \exp(i\bar{\omega}t)\delta(x-vt) \qquad 5.27$$

where $\delta(x-vt)$ is Dirac delta function as well as $w_r(x,t)$ and $\bar{\omega}$ indicate rail displacement and load frequency. Terms $\exp(i\bar{\omega}t)$ and $\delta(x-vt)$, respectively, show that the load is oscillating with frequency $\bar{\omega}$ and moving. It is also assumed that at time t=0, the location of first load is x=0.

A number of solutions proposed to solve the differential equation (Hussein & Hunt 2006), (Frýba 1999). An easy way to solve the above equations is to use Fourier transformation. In other words, the problem should be transformed from time-space domain (x, t) to wavenumber-frequency domain (ζ, ω).

Double Fourier transform results in

$$EI_r\zeta^4\tilde{w}_r - m_r\omega^2\tilde{w}_r + k_p\tilde{w}_r + c_p i\omega\tilde{w}_r = 2P_0\pi\delta(\omega+\zeta v-\tilde{\omega}) \qquad 5.28$$

In which $\tilde{w}_r$ and $\tilde{\omega}$ are transformed rail displacement and load frequency respectively, and

"i" is unit imaginary number.

Applying double inverse Fourier transform, rail displacement in time-space domain takes form

$$w_r(x,t)=\frac{P_0\exp(i\bar{\omega}t)}{2\pi}\int_{-\infty}^{\infty}\frac{\exp\left(i\zeta(x-vt)\right)}{EI_r-m\bar{\omega}^2-mk^2V^2+2mkV\bar{\omega}+k_p+\bar{\omega}c_pi-k_pc_pVi}d\zeta \qquad 5.29$$

By determining the poles of the integrand and applying theory of residues, rail displacement can be determined (Hussein & Hunt 2006). The solution is repeated for other three loads which are located at 2, 8 and 10 meters from the first load. Assuming linear elastic materials, beam response can be calculated by the superposition principle.

Figure 5.9 shows the time histories of midpoint deflection obtained by the current and analytical solutions. As the Figure suggests, the results from numerical procedure used in this research are in good agreement with those from theory. In the figure, less than 5% discrepancy can be observed. Note that, no rail irregularities are considered in the verification model.

The parameters used in both theoretical and numerical solutions are shown in Table 5.4.

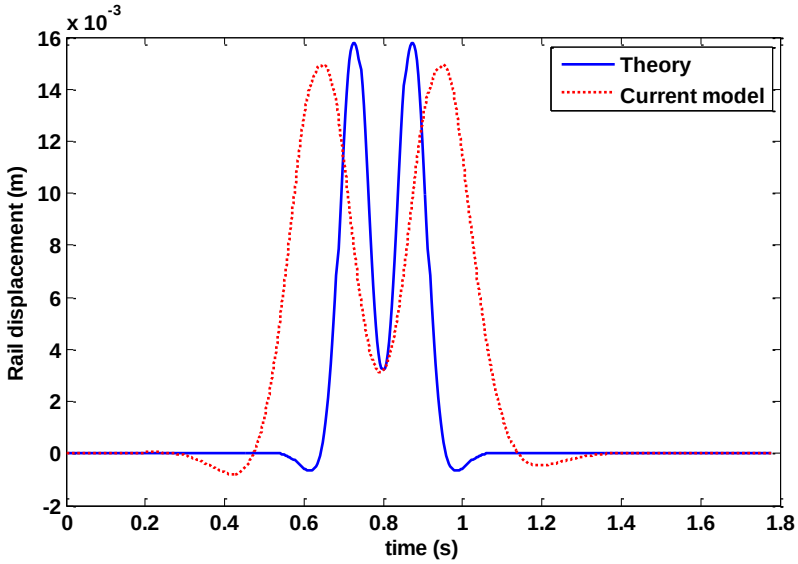

Figure 5.9 Rail midpoint displacements from theory and current model

6. Analyses results

This chapter presents the results of analyses of the vehicle, track and bridge and discusses the effects of rail defects on track and vehicle response. Both lateral and vertical defects are investigated and the results compared to conclude the influence of each defect on track and vehicle vibration. This chapter also investigates the impact of train and track parameters on bridge dynamic response.

6. 1. Rail defects

Three kinds of rail flaws are considered: rail irregularities, rail joints (with or without dip and raise) and rail corrugation. The results obtained from different parameters to determine the significance of rail flaws on rail impact factor. In the analyses, unless mentioned otherwise, it is assumed that track is in class 6 condition and train speed is 100 km/hr.

6. 1. 1. Effect of Rail Corrugation

Corrugation is a prevalent defect on rail head initiating from rail head de-carbonization (on new steel) and irregularities such as rail manufacture pitting, contact fatigue defects, rail welds, rail joints, etc. (American Railway Engineering and Maintenance-of-Way Association 2010). Corrugations with different depths and frequencies are detected in the field. The International Union of Railways, based on wavelength, divided this defects into two groups: short-pitch with wavelength between 3 to 8 cm, and long-pitch corrugation with wavelength between 8 to 30 cm (International Union of Railways 2002). The depth of corrugation also varies depending on rail and wheel condition. In this study, the depth of corrugation is considered between 0.01 to 0.1 mm. Figure 6.1 shows the short (0.05 m wavelength) and long pitch (0.3 m wavelength) corrugation. The corrugation is simulated as a sine wave and the same phase for the right and left rails.

To demonstrate the effect of rail defects on dynamic forces, the impact factor will be used as a criterion. Impact Factor indicates the increase in forces due to dynamic excitations and is defined by the following equation

$$\text{Impact Factor}(\%) = \frac{\text{Maximum Dynamic Response} - \text{Maximum Static Response}}{\text{Maximum Static Response}} \times 100 \qquad 6.1$$

It should be noted that based on the vehicle data used in this research, the static load of train is 75 KN. Figure 6.2 shows the effect of rail corrugation depth and wavelength on rail displacements. Increasing corrugation depth from 0.02 mm to 0.05 mm leads to 0.1 mm increase in rail vertical displacement, but corrugation wavelength is not as effective as corrugation depth and the maximum rail displacement in this case is about 0.05 mm.

Figure 6.3 shows the relation between corrugation depth and the impact factor of the rail and vehicle forces. It is evident that for deeper corrugation, the accelerated increase in impact factor occurs. The same trend can be observed for the rail, primary suspension and car body. The highest rail impact factor is 103% for 0.1 mm rail corrugation.

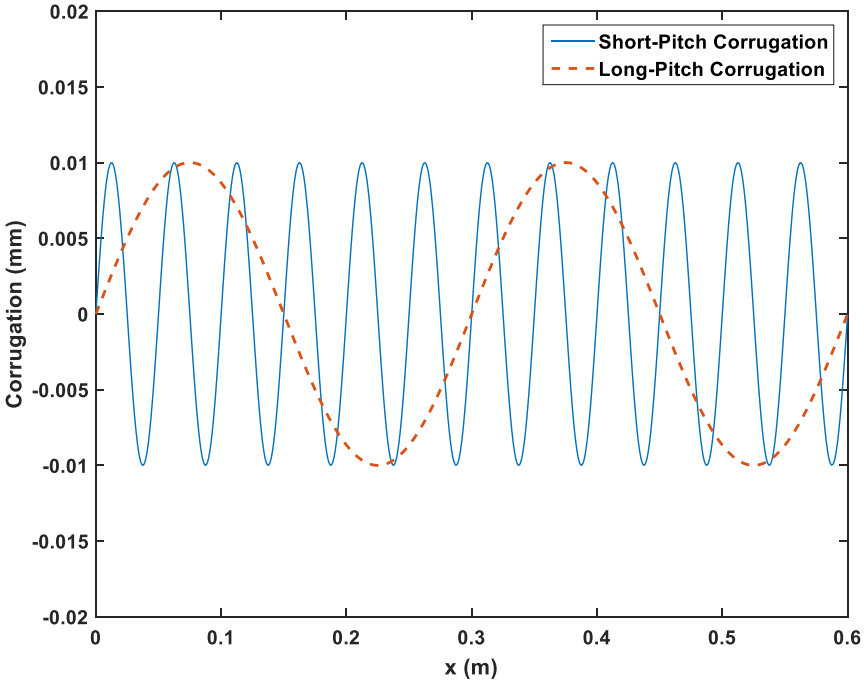

Figure 6.1 short-pitch and long-pitch corrugation

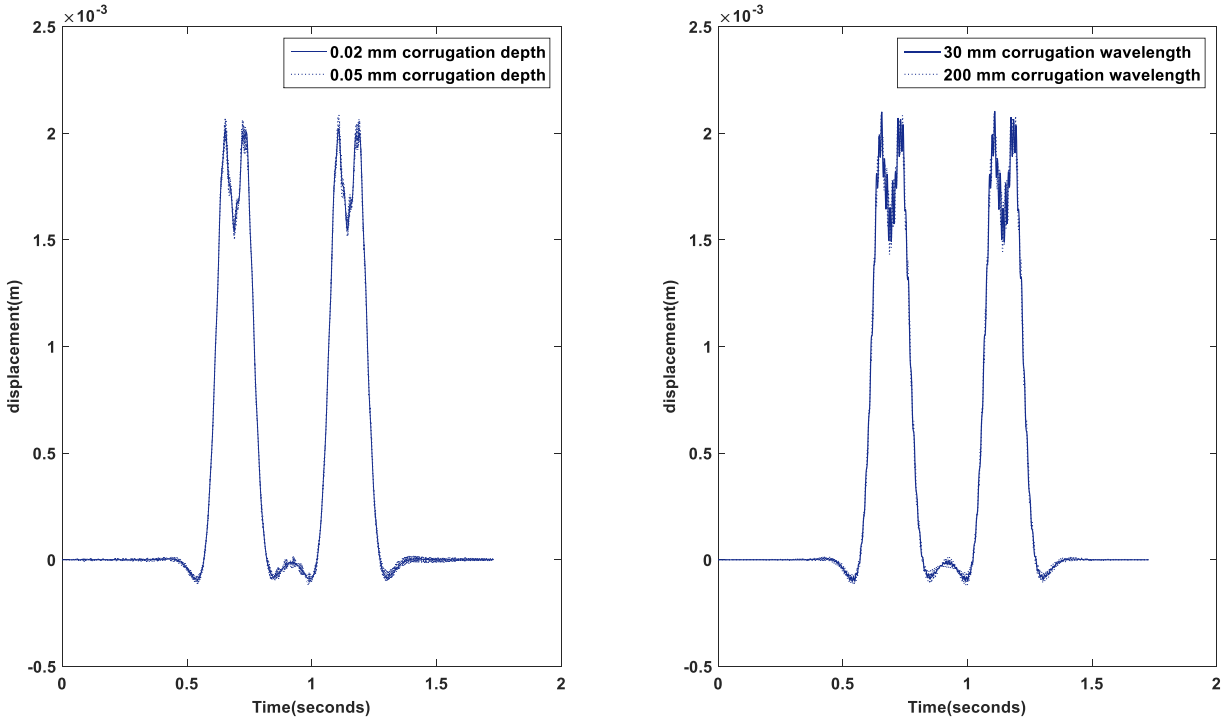

Figure 6.2. the effect of rail corrugation depth (left) and rail corrugation wavelength (right) on rail displacement

Figure 6.4 shows the impact factor for different corrugation wavelength. In this case, the depth of corrugation is 0.04 mm and the dynamics amplification is observed for different wavelength range from 50 to 300 mm. This figure shows that with increasing the wavelength, the impact factor decreases considerably. This trend is valid especially for lower wavelengths. As the wavelength of corrugation increases the rate of impact factor reduction drops. This trend can be clearly seen in the case of car body vertical impact factor where the impact factor decreases sharply as wavelength increases.

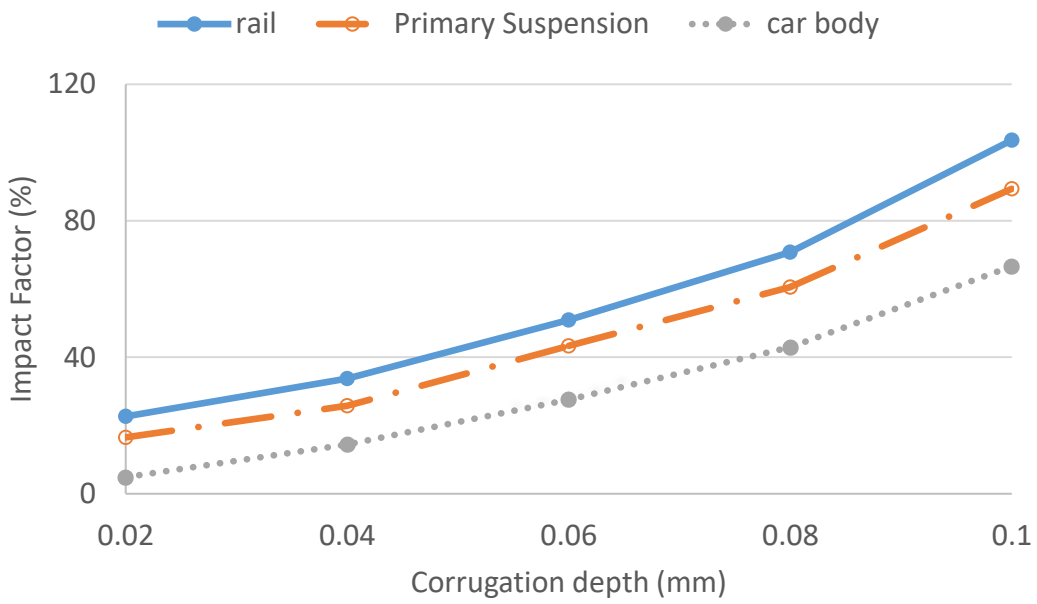

Figure 6.3. The effect of corrugation depth on rail impact factor

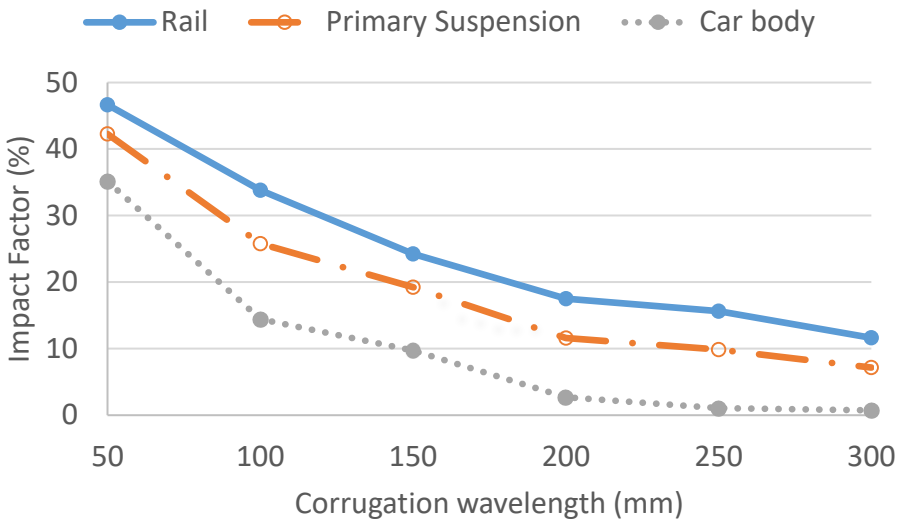

Figure 6.4. the effect of corrugation wavelength on rail impact factor

Figure 6.5 and Figure 6.6 demonstrate the effect of train speed on rail impact factor for different wavelengths and depths. As Figure 6.5 depicts, at a certain speed the dynamic force reaches its maximum value. This critical speed for the wavelengths 100 and 200 mm is 200 km/hr, and for corrugation with the wavelength 300 mm, it increases to about 250 km/hr. It is evident from Figure 6.6 that there is the same trend for deeper corrugation but in this case, the impact factor increases substantially and the maximum value is 4.7 times greater than that of 0.01 mm corrugation depth. This graph also shows that increasing corrugation depth has a major effect on rail impact factor for longer wavelength. For example, in case of 250 km/hr train speed shown in Figure 6.5, the impact factor corresponding to 300 mm wavelength is 4% higher than that of 100 mm wavelength while as shown in Figure 6.6, this value increases to 31% with increasing corrugation depth from 0.01 to 0.1 mm.

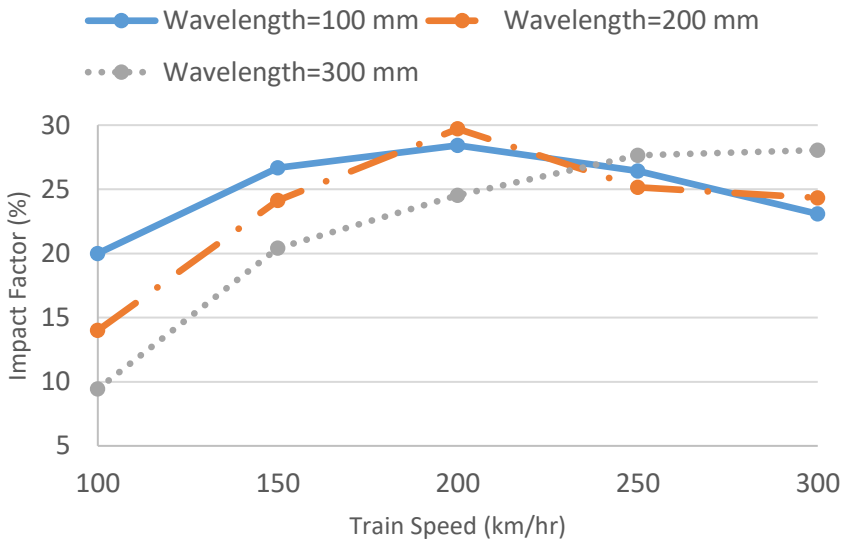

Figure 6.5. the effect of train speed on rail impact factor (for 0.01 mm corrugation depth)

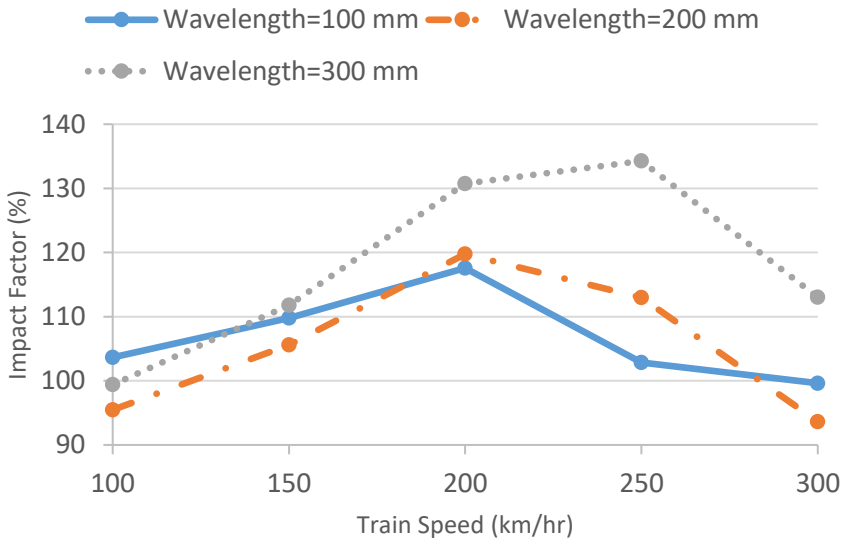

Figure 6.6. the effect of train speed on rail impact factor(for 0.1 mm corrugation depth)

6. 1. 2. Rail joint dip and raise

Some rail defects including shelling of running surface, crushing, and rail burning may cause rail dip. Many of these defects are not visible or hardly visible at the outset, and become apparent in the track after a time-interval which varies according to the traffic load (International Union of Railways 2002). Rail joints are one of the most important track

points of weakness. Due to defects such as rails height difference, rail joints are susceptible to cause rail accidents. This problem especially arises when the rail joint is dipped. Figure 6.7 shows a schematic view of rail dip. The curve of the dipped rail is modeled by quadratic functions and characterized by parameters “L”, length of dip, “H”, depth of dip, and “α”, the dip angle (Wu & Thompson 2003).

The opposite case or raise on rail joints may also happen. This flaw may especially occurs due to manufacturing or material defects and improper welding (Sun & Dhanasekar 2002), (Steenbergen & Esveld 2006). Raise on rail surface is a dangerous defect and generates great dynamic forces. In order to compare the results from rail surface flaws, the same conditions as rail dip has been taken into account. The shape of the raise on rail surface is quadratic and the same parameters “L”, “H” and “α” have been used to characterize the rail defect.

In this research, the effect of defects parameters on rail impact factor is investigated for track class 6 and different train speeds. Figure 6.8 shows the rail impact factor for rail joints with and without defect for different train speed. As the Figure 6.8 suggests, in the condition of no defect, the impact factor does not change considerably with increasing load speed. The maximum impact factor is 13% for 100 km/hr train speed. However, dip in rail joint has a profound influence on rail dynamic forces. With increasing speed, impact factor increases from 18% to 62% when vehicle speed increases from 50 to 200 km/hr. the graph also demonstrates that the rate of increase in impact factor is a function of train speed and higher speeds result in increasingly more impact factor. Figure 6.9 to Figure 6.10 also compares rail impact factor for rail joint raise and dip. The results of the study show that the defects causing rail raise generally produce much more dynamic forces compared to

dip type defects. Figure 6.9 implies that the rail impact factor increases considerably when the depth of defect increases. In Figure 6.10, with increasing the defect length, the rail impact factor increases sharply to the maximum value which occurs at the defect length of 0.3 m, then it decreases. This figure also shows that the impact of the defect length on the rail impact factor reduces gradually. Moreover, it is evident that for the shorter defect length, the difference of rail impact factors between raised and dipped flaws is considerable. The results are shown for 1 mm deep rail dip.

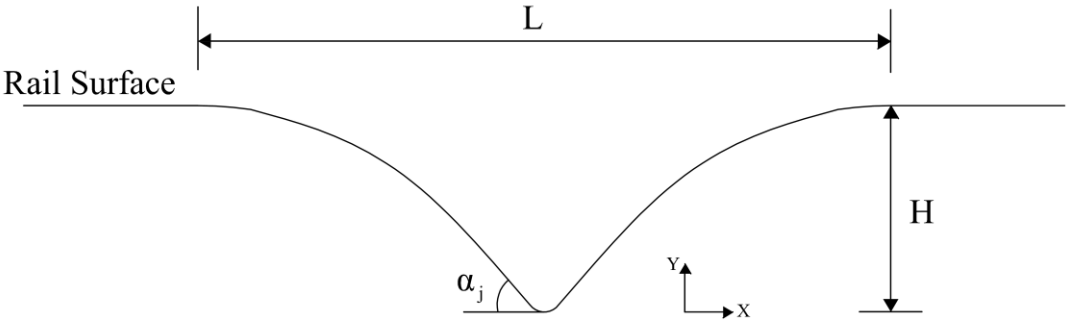

Figure 6.7. Rail dip shape

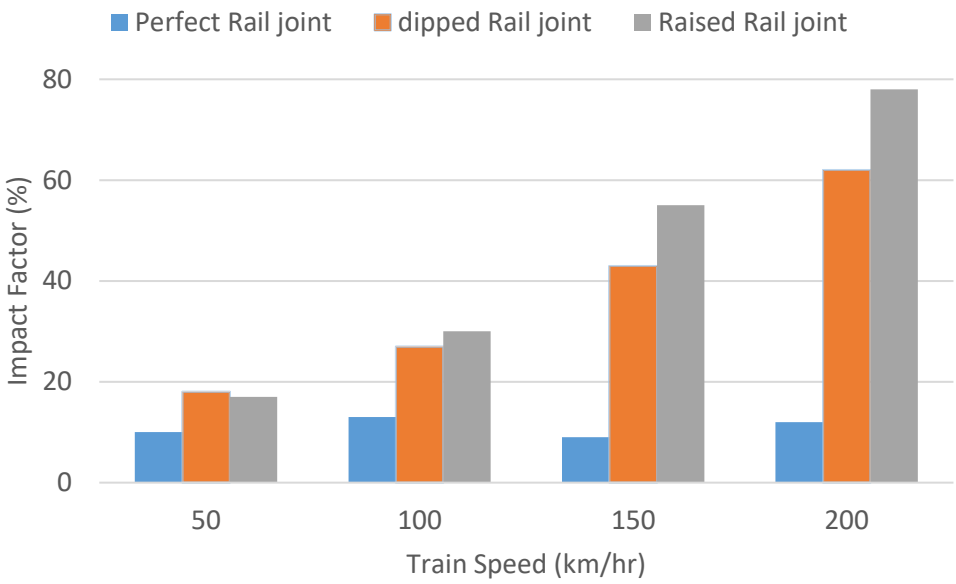

Figure 6.8. The effect of dip and raise on rail joint impact factor

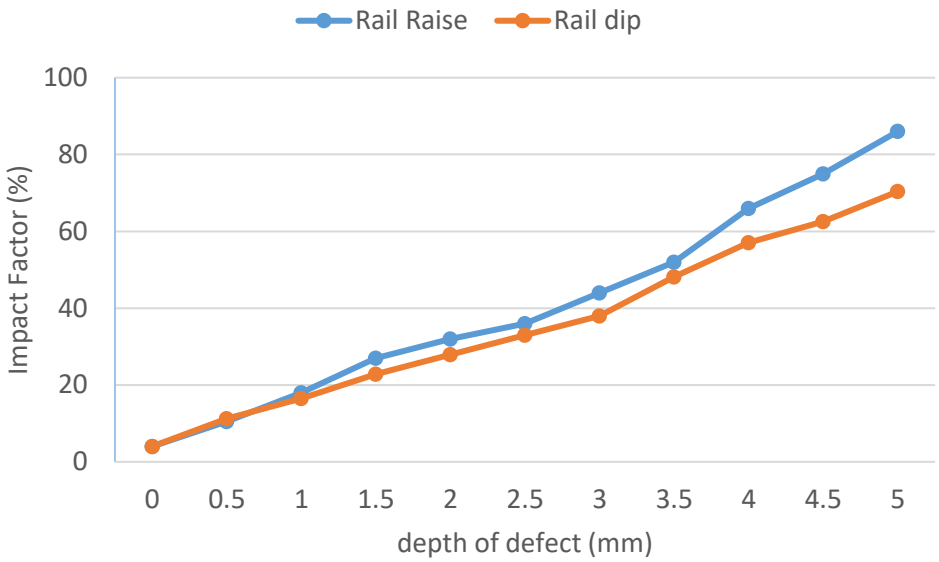

Figure 6.9. The effect of depth of rail dip and raise on rail impact factor

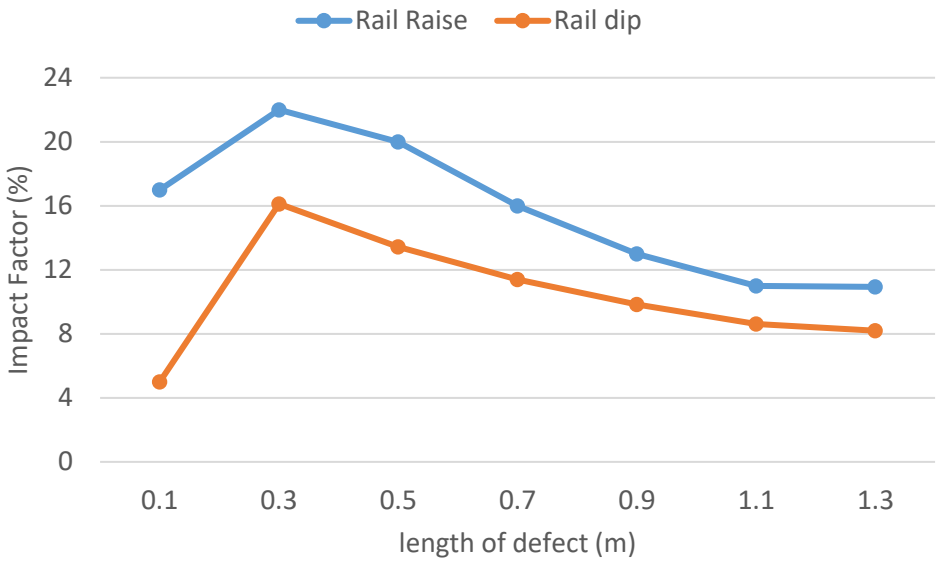

Figure 6.10. The effect of the length of rail dip and raise on rail impact factor

6. 1. 3. Rail random irregularities

As mentioned earlier, track irregularities are random in nature and no specific pattern in rail roughness can be seen. As a result, no detectable trend in impact factor can be observed. Figure 6.11 and Figure 6.12 show the impact factor of rail, primary suspension and car

body for different train speeds for tracks class 4 and 6 ,respectively, as defined by FRA. The figures show that rail has the highest impact factor and the maximum impact factor reach 34% and 62% for class 4 and 6, respectively. Comparison of the results obtained from track class 6 with those from track class 4 also reveals that improving track condition leads to about 25% reduction in rail impact factor, but in case of car body, the difference between impact factors obtained from class 4 and 6 is limited to 17%. It is also evident that the train speed has little influence on impact factor when it increases to 250 km/hr or higher.

Figure 6.13 depicts the difference between rail displacements of classes 4 and 6. There is a maximum of 7% difference between the results from two track categories.

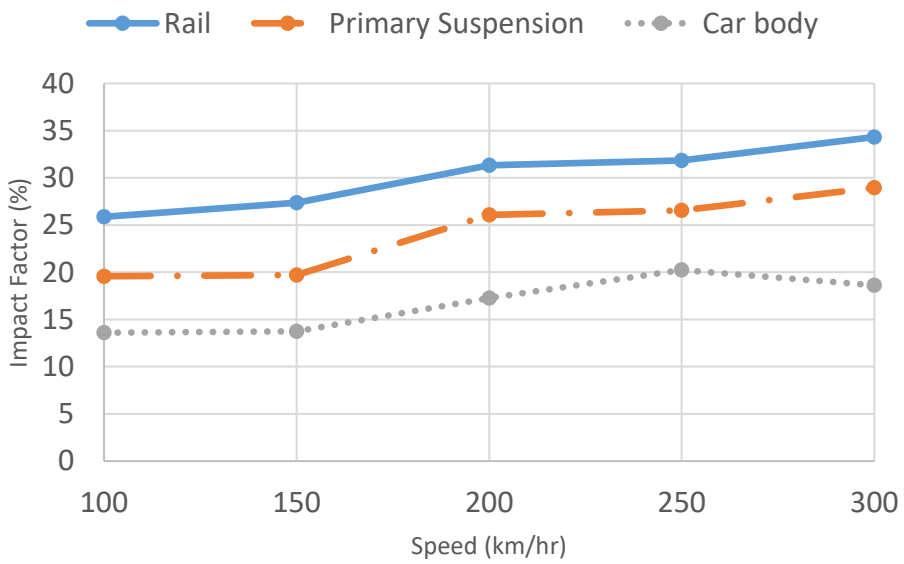

Figure 6.11. Rail impact factor for track class 6

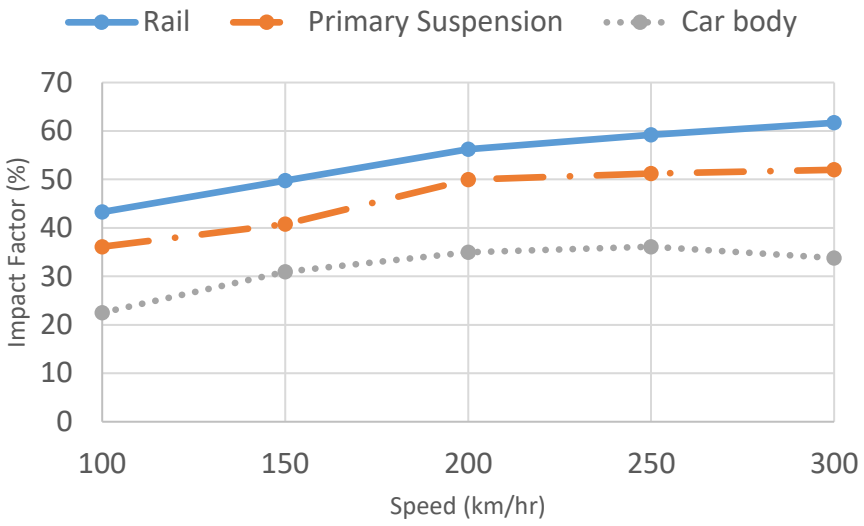

Figure 6.12. Rail impact factor for track class 4

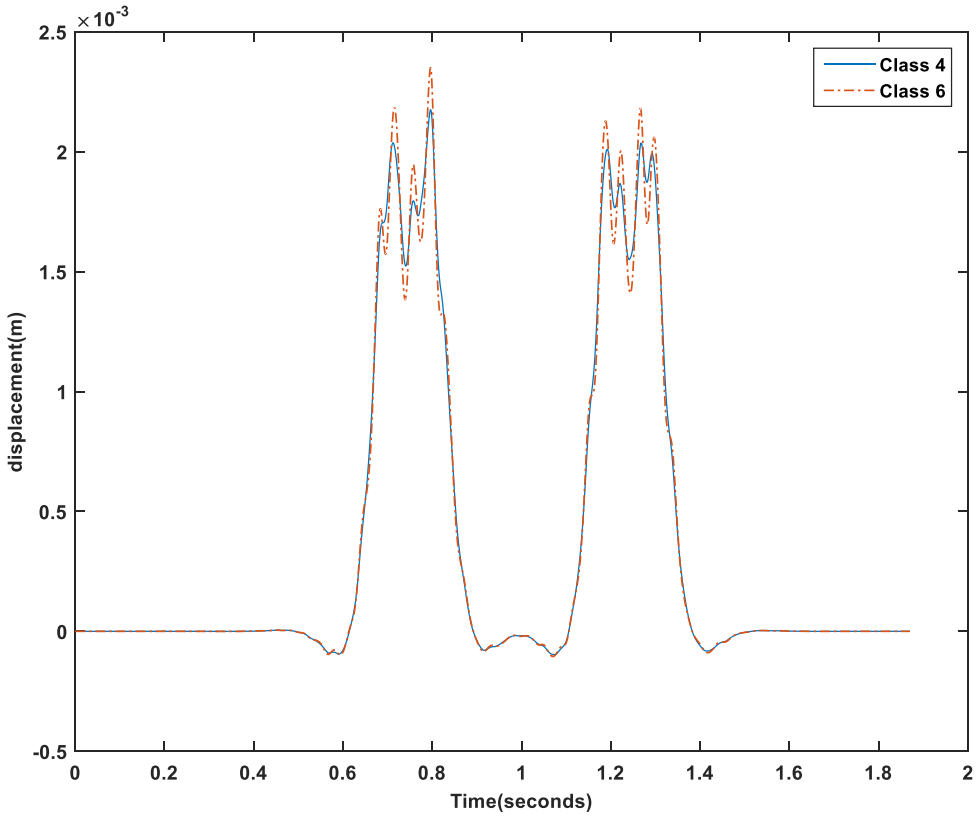

Figure 6.13. Rail displacement for track class 6 and class 4

6. 2. The influence of bridge parameters on track response

This section discusses how track and vehicle parameters affect the bridge impact factor and determines the critical response of bridge. The values of bridge parameters used in the analyses are shown in Table 5.2. The initial values of vehicle's speed and axle load are considered as 100 km/hr and 15 ton, respectively.

Figure 6.14 shows the influence of rail defects on bridge impact factor. To obtain the results, static and dynamic forces on bridge due to the passage of trains were compared. Three rail defects or rail random irregularities, rail raise, and rail corrugation are considered to determine impact factors for different bridge spans. The range of bridge spans is considered 10 to 40 m.

As Figure 6.14 shows the rail random irregularities have the least effect on bridge impact factor and as it is expected, track class 6 has less influence on bridge forces compared to track class 4. The graph also demonstrates that, for track class 6, bridge span-impact factor graph is almost linear, but track class 4 shows nonlinear behavior, especially for longer bridge spans. The other important conclusion from Figure 6.14 is that rail raise and corrugation clearly causes greater impact factors compared to random rail irregularities. The average impact factor induced by irregularities is about 20% less than that of other rail flaws. This figure also suggests that rail raise has the most influence on bridge response. However, for longer bridge spans, rail corrugation has almost the same impact on bridge forces as rail raise does. For the analyses, the rail raise parameters or depth and length, are chosen to be 0.5 mm and 0.3 meter, respectively.

Figure 6.15 shows the influence of vehicle parameters on bridge impact factor. Two parameters of vehicle speed and vehicle axle load have been taken into account. The range

of train speed is 100 to 250 km/hr. As it is shown, the behavior of impact factor due to rail irregularities is almost linear especially for track class 6. Rail raise shows highly nonlinear behavior. It can also be observed that rail raise has the biggest influence on the bridge impact factor as train speed increases.

Axle load, compared to train speed, shows more linear behavior. The same trend as before can be seen and rail irregularities and rail raise have the most and least influence on bridge impact factor, respectively. The difference between impact factors of rail raise and track class 6 irregularities is about 50%.

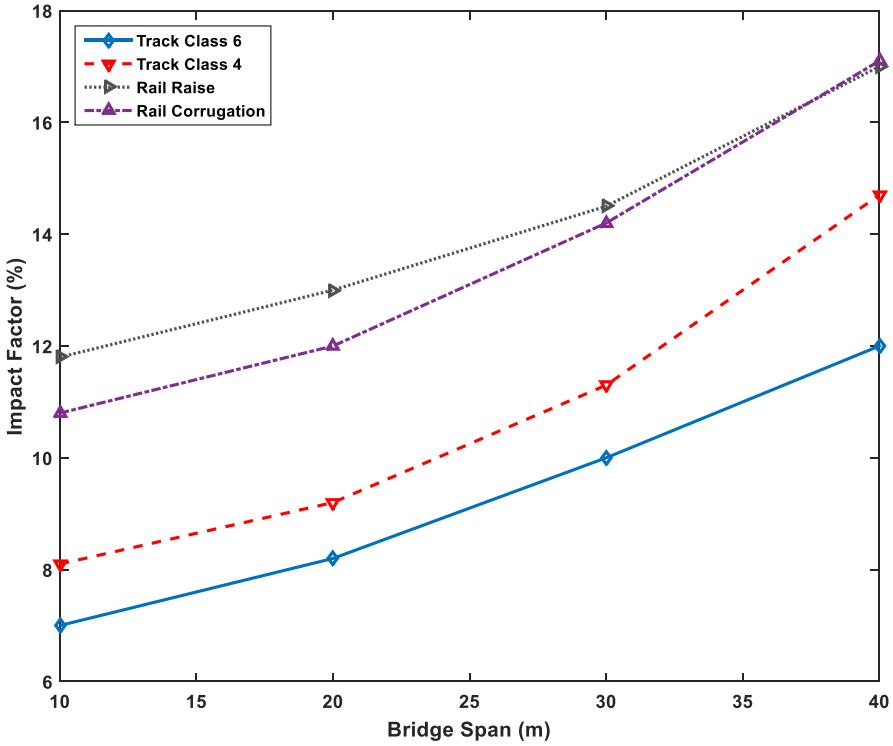

Figure 6.14. the influence of rail defects on bridge impact factor

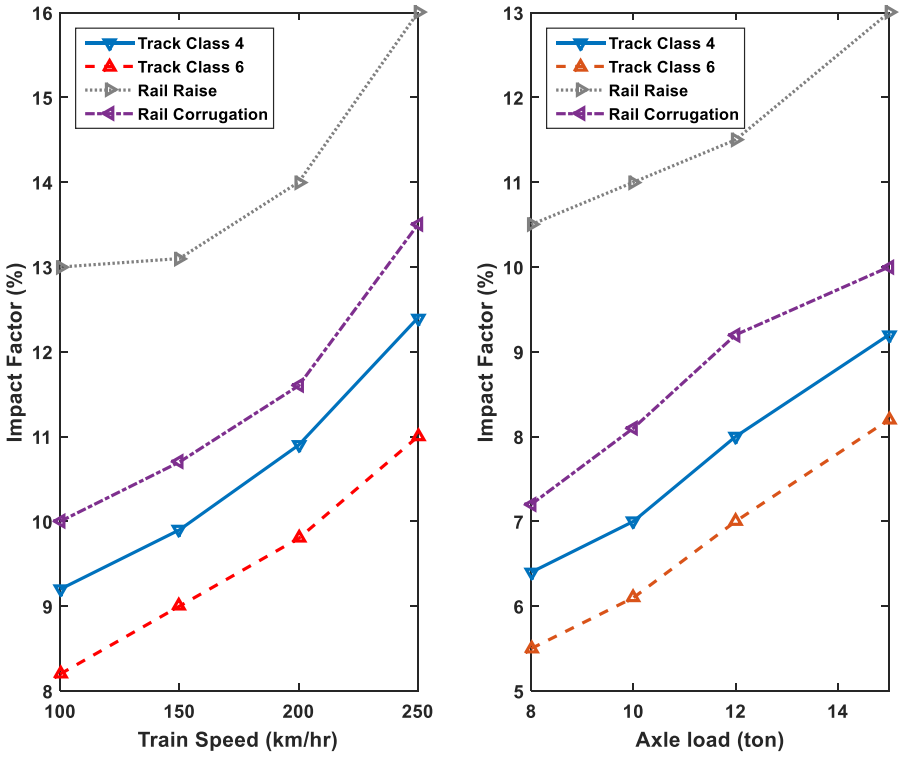

Figure 6.15. the influence of train speed and axle load on bridge impact factor

7. Vehicle Stability on Curves

As it was shown in the previous chapters, the lateral loading due to irregularities has negligible effects on track and vehicle response compared to vertical irregularities. Therefore, most research on vehicle-track analysis has been dedicated to straight beam behavior under train loadings. However, in curves with small radius, the lateral loading is significant enough that it might pose the risk of vehicle overturning. This issue is especially important for high-speed trains where centrifugal forces due to cross level (cant) deficiencies can increase the lateral forces considerably.

This chapter includes the formulation of the curved beam in railroad tracks and discusses the results of analyses on the vehicle stability. The findings from this chapter can be used to have a better understanding of the response of the vehicle-track system on the curve and put limitations on vehicle and track parameters to assure safety and smooth running of the vehicle.

7. 1. Curved beam formulations

Adding curvature parameters to beam formulation makes it more difficult to solve compared to the straight beam. In other words, out-of-plane response, i.e. vertical displacement, needs to be determined, as well as, in-plane or horizontal displacement. Curvature makes radial displacement and torsional rotation important in analysis, which can be easily neglected in the straight beam analysis.

To derive the curved beam formulations, it is assumed that: (1) beam is considered to be elastic and homogeneous; (2) transverse displacements are large compared to longitudinal displacements; (3) beam curvature is constant and does not change in the beam length.

Figure 7.1 demonstrates a two-node curved beam element with constant radius “R” and

displacements “u,” “v” and “w” in “x”, “y” and “z” direction, respectively.

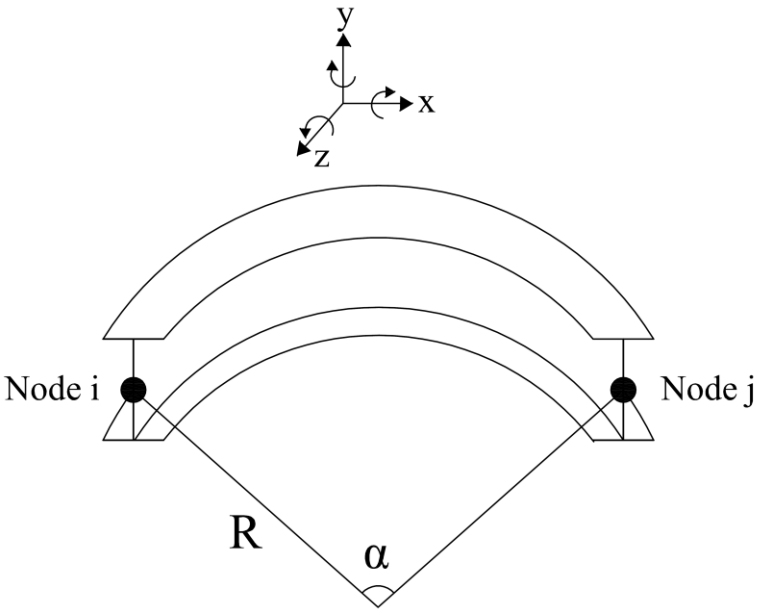

Figure 7.1 Curved beam element

To form the differential equations of the curved beam, the principle of virtual displacements has been utilized. The principle of virtual displacements states that if an elastic structure is in equilibrium, then the virtual work due to external forces is equal to the virtual work due to internal stresses. Neglecting body forces, the equilibrium of a beam with volume “V” and length “l” can be formulated

$$\int S_{ij}\delta\varepsilon_{ij}dV = External\ Virtual\ Work\ (E.V.W) \qquad 7.1$$

where, S_{ij} is the second Piola-Kirchhoff stress tensor; and $\delta\varepsilon_{ij}$ is the variation of the Green-Lagrange strain tensor (Yang & Kuo 1987).

The left-side of the equation expands as follows

$$\int S_x \delta e_x dV + \int (S_{xy}\delta e_{xy} + S_{xz}\delta e_{xz}) dV + \int S_x \delta \eta_x dV + \int (S_{xy}\delta \eta_{xy} + S_{xz}\delta \eta_{xz}) dV + \int S_z \delta \eta_z dV = E.V.W \tag{7.2}$$

The expanded formula shows that the internal virtual work consists of five terms, which accounts for strain energy of axial forces, strain energy of shear stresses, potential energy of axial stresses, potential energy of shear stresses and potential energy of radial stresses. Each term can then be rewritten as follows

$$\int S_x \delta e_x dV = \frac{1}{2}\int_0^l \left[EA\delta \left(u' + \frac{w}{R}\right)^2 + EI_y \delta \left(w'' + \frac{w}{R^2}\right)^2 + EI_z \delta \left(v'' - \frac{\theta}{R}\right)^2 + EC_w \delta \left(\theta'' + \frac{\theta}{R^2}\right)^2 \right] dx \tag{7.3}$$

where "θ" is twist angle. "E", "A" and "I" represent modulus of elasticity, cross section area and moment of inertia of the beam. "C_w" is warping constant.

$$\int (S_{xy}\delta e_{xy} + S_{xz}\delta e_{xz}) dV = \frac{1}{2}\int_0^l GJ\delta \left(\theta' + \frac{v'}{R}\right)^2 dx \tag{7.4}$$

$$\int S_x \delta \eta_x dV = \frac{1}{2}\int_0^l \left\{ F_x \delta \left[v'^2 + \left(w' - \frac{u}{R}\right)^2 \right] + M_y \delta \left[\frac{1}{R}\left(w' - \frac{u}{R}\right)^2 - 2v'\theta' - \frac{v'^2}{R} \right] - 2\left(M_z + \frac{B}{R}\right)\delta \left[\left(\theta' + \frac{v'}{R}\right)\left(w' - \frac{u}{R}\right) \right] + \bar{K}\delta \left(\theta' + \frac{v'}{R}\right)^2 \right\} dx \tag{7.5}$$

where η_x is nonlinear strain and F_x is axial force

$$\delta\eta_x = \frac{1}{2}\left[\left(\frac{\partial u}{\partial x}+\frac{w}{R}\right)^2+\left(\frac{\partial v}{\partial x}\right)^2+\left(\frac{\partial w}{\partial x}-\frac{u}{R}\right)^2\right]\left(\frac{R}{R+z}\right)^2 \tag{7.6}$$

and $\overline{K} = \int S_x(y^2+z^2)dA = \left(F_x+\frac{M_y}{R}\right)r^2, \quad r^2 = \frac{I_y+I_z}{A}$

$$\begin{aligned}\int (S_{xy}\delta\eta_{xy} + S_{xz}\delta\eta_{xz})dV \\ = \int_0^l \Bigg\{ & F_y\delta\left[-v'\left(u'+\frac{w}{R}\right)+\theta\left(w'-\frac{u}{R}\right)\right] \\ & - F_z\delta\left[\left(w'-\frac{u}{R}\right)\left(u'+\frac{w}{R}\right)+\theta v'\right] \\ & - (1-\gamma)M_x\delta\left[\frac{\theta}{R}\left(w'-\frac{u}{R}\right)+v'\left(w''-\frac{u'}{R}\right)\right] \\ & + \gamma M_x\delta\left[\left(w'-\frac{u}{R}\right)\left(v''-\frac{\theta}{R}\right)\right]\Bigg\} dx\end{aligned} \tag{7.7}$$

In which, M_x is torque (moment about axis x) and

$$\eta_{xy} = \left[\frac{\partial u}{\partial y}\left(\frac{\partial u}{\partial x}+\frac{w}{R}\right)+\frac{\partial v}{\partial y}\frac{\partial v}{\partial x}+\frac{\partial w}{\partial y}\left(\frac{\partial w}{\partial x}-\frac{u}{R}\right)\right]\frac{R}{R+z} \tag{7.8}$$

$$\eta_{xz} = \left[\frac{\partial u}{\partial z}\left(\frac{\partial u}{\partial x}+\frac{w}{R}\right)+\frac{\partial v}{\partial z}\frac{\partial v}{\partial x}+\frac{\partial w}{\partial z}\left(\frac{\partial w}{\partial x}-\frac{u}{R}\right)\right]\frac{R}{R+z} \tag{7.9}$$

$$\gamma = \frac{\int S_{xz}ydA}{M_x} \tag{7.10}$$

$$\int S_z\delta\eta_z dV = -\int \frac{M_y}{2R}\delta\left[\theta^2+\left(w'-\frac{u}{R}\right)^2\right]dx \tag{7.11}$$

Expressing the external virtual work in the following format results the differential equations of a curved beam

$$E.V.W = \left[F_x\delta u + F_y\delta v + F_z\delta w + M_x\delta\theta - M_y\delta\left(w' - \frac{u}{R}\right) + M_z\delta v' + B\delta\left(\theta' + \frac{v'}{R}\right)\right] \quad 7.12$$

where $B = EC_w\theta^{"}$

Axial displacement

$$EA\left(u" + \frac{w'}{R}\right) + \frac{1}{R}F_x\left(w' - \frac{u}{R}\right) - \frac{1}{R}\left(M_z + \frac{B}{R}\right)\left(\theta' + \frac{v'}{R}\right) + \frac{1}{2R}T'_{sv}v' - \left(F_y - \frac{M_x}{R}\right)\left(v" - \frac{\theta}{R}\right) - F'_z\left(w' - \frac{u}{R}\right) - F_z\left(w" + \frac{w}{R^2}\right) = 0 \quad 7.13$$

Radial displacement

$$EI_y\left(w'''' + 2\frac{w"}{R^2} + \frac{w}{R^4}\right) + \frac{EA}{R}\left(u' + \frac{w}{R}\right) - \left[F_x\left(w' - \frac{u}{R}\right)\right]' - \frac{1}{2}(T'_{sv}v')' + \left[\left(M_z + \frac{B}{R}\right)\left(\theta' + \frac{v'}{R}\right)\right]' - F_y\left(\theta' + \frac{v'}{R}\right) + F_z\left(u" + \frac{u}{R^2}\right) + F'_z\left(u' + \frac{w}{R}\right) - \left[M_x\left(v" - \frac{\theta}{R}\right)\right]' = 0 \quad 7.14$$

Vertical displacement

$$EI_z\left(v'''' - \frac{\theta''}{R}\right) - \frac{GJ}{R}\left(\theta'' + \frac{v''}{R}\right) - (F_x v')' + \left[M_y\left(\theta' + \frac{v'}{R}\right)\right]' + (F_z\theta)'$$
$$+ F_y\left(u'' + \frac{w'}{R}\right) + \frac{1}{R}\left[\left(M_z + \frac{B}{R}\right)\left(w' - \frac{u}{R}\right)\right]'$$
$$+ \frac{r^2}{R}\left[\left(F_x + \frac{M_y}{R}\right)\left(\theta' + \frac{v'}{R}\right)\right]' + \left[\left(M_x - \frac{1}{2}T_{su}\right)\left(w' - \frac{u}{R}\right)\right]' \quad 7.15$$
$$+ \left[M_x\left(w'' - \frac{u'}{R}\right)\right]' = 0$$

Torsional rotation

$$EC_w\left(\theta'''' + 2\frac{\theta''}{R^2} + \frac{\theta}{R^4}\right) - \frac{EI_z}{R}\left(v'' - \frac{\theta}{R}\right) - GJ\left(\theta'' + \frac{v''}{R}\right) + M_y\left(v'' - \frac{\theta}{R}\right)$$
$$+ \left[\left(M_z + \frac{B}{R}\right)\left(w' - \frac{u}{R}\right)\right]' - r^2\left[\left(F_x + \frac{M_y}{R}\right)\left(\theta' + \frac{v'}{R}\right)\right]' \quad 7.16$$
$$+ F_y\left(w' - \frac{u}{R}\right) - \frac{M_x}{R}\left(w' - \frac{u}{R}\right) = 0$$

7. 2. Lateral forces on vehicle

Lateral forces applied on the vehicle can be divided into three categories: (1) forces due to gravity and centrifugal forces; (2) forces due to rail irregularities and defects; and (3) wind loading. This section discusses how to determine these three lateral forces applied on the vehicle. The result of this section will be used to determine the stability of vehicles under different conditions.

7. 2. 1. Gravitational and centrifugal forces

Centrifugal forces at horizontal curves generate an unbalanced force on vehicles which may cause extra forces at wheel-rail interface, as well as instability of the vehicle. As Figure 7.2 demonstrates, a centrifugal acceleration v^2/R applies on a vehicle running at

constant speed “v” through a curve with a radius “R”. The track cant (super-elevation) that balances the lateral acceleration of the vehicle at curve is called “equilibrium cant”, which can be calculated by the following approximate formulas

$$CE = 4\frac{V^2}{R} \ \ (American\ units)$$
$$CE = 11.8\frac{V^2}{R}\ (metric\ units) \qquad 7.17$$

where “V”,“R” and “CE” are vehicle speed in mph (km/h), curvature radius in feet (meter) and super-elevation in inches (millimeters), respectively. It is also assumed the track gauge is standard or 56.5 in (1435 mm). Cant deficiency and cant excess lead to underbalanced and overbalanced forces.

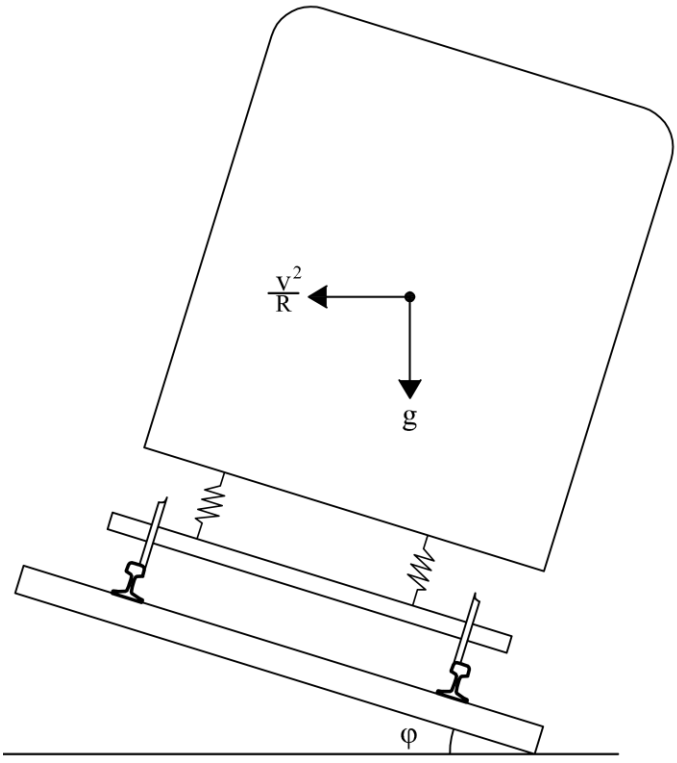

Figure 7.2 Vehicle and track at curve

In the American railroad, maximum cant is 6 inches (152 mm) and unbalanced cant should

not be more than 3 inches (76 mm). However, for freight train, the super-elevation is limited to 4 inches (101 mm). (Brinckerhoff Parsons Consulting Co. 2009)

7. 2. 2. Rail irregularities

Defects in track geometry which are presented as irregularities in gauge and super-elevation are the major source of track and vehicle lateral forces. As it was discussed in chapter 4, to simulate rail irregularities, appropriate PSD equations should be used.

7. 2. 3. Wind forces

There have been reports on wind induced accidents and derailments around the world in recent decades (Li et al. 2005). As the speed of vehicles increases and more high-speed trains become operational, rail vehicles are more susceptible to the wind loading. To response to this issue, some researchers have investigated the influence of wind on vehicle response. Vehicle-Wind-Track interactions have been studied through analytical methods, Computational Fluid Dynamics (CFD) analysis and wind tunnel tests. As the formulas of this section suggest, estimating the coefficients of wind forces depends on vehicle type and speed which makes their estimation difficult. Li et al. (2005) mentioned the difficulties of doing wind tunnel test for moving vehicles. As a result, more approximation should be applied (Li et al. 2005).

In this section, using theoretical method the effect of wind loads and other lateral forces on train stability will be discussed.

In the analysis of Vehicle-Wind-Track interaction the following assumptions have been made

- The train speed (V_T) is constant
- The direction of train and wind is perpendicular

- There is no change in the direction of vehicle and wind
- The aerodynamic effects of first and last wagon is neglected and train is considered long enough so strip assumption can be made

The detailed procedure of calculating wind loads was presented in the previous studies (Li et al. 2005) and Zhang et al. 2013).

Due to wind velocity fluctuations in wind direction (u) and vertical to wind direction (w), the wind's angle of attack is non-zero (α). The vehicle yawing angle (β), also needs to be considered in calculations.

The wind velocity and angle of attack considering fluctuations reads

$$U_R^2 = (U+u)^2 + w^2 \quad , \qquad \alpha = \arctan\frac{w}{U+u} \tag{7.18}$$

Where "U" is mean wind speed.

The relative wind velocity (V_R) to the vehicle is

$$V_R^2 = (U+u)^2 + w^2 + V_T^2 \quad , \qquad \beta = \arctan\frac{V_T}{U_R} \tag{7.19}$$

Since the speed fluctuations are small compared to the mean wind velocity, higher-order terms of "u" and "w" can be neglected.

$$U_R^2 = U^2 + 2Uu \quad , \qquad \alpha = \frac{w}{U} \tag{7.20}$$

$$V_R^2 = U^2 + 2Uu + V_T^2 \quad , \qquad \beta = \arctan\frac{V_T}{U} \tag{7.21}$$

Then, the aerodynamic force per unit length can be determined (Simiu 2011)

$$D = \frac{1}{2}\rho H C_D(\alpha,\beta) V_R^2 \tag{7.22}$$

$$L = \frac{1}{2}\rho B C_L(\alpha,\beta)V_R^2$$

$$M = \frac{1}{2}\rho B^2 C_M(\alpha,\beta)V_R^2$$

In which "D", "L" and "M" are drag, lift and moment due to wind effect. "ρ" is air density and "H" is the reference height which is the height of car body and "B" is the width of the car body.

"C_D", "C_L" and "C_M" are the coefficients of drag, lift and moment.

Using the Taylor series at $\alpha = 0$ and writing the above formula in vehicle coordinate system, wind forces take the following shape

$$D = \frac{1}{2}\rho H\bar{V}_R^2\left(C_D(\beta) + C_D(\beta)\frac{2Uu}{\bar{V}_R^2}\gamma_1 + \left[C_D'(\beta) - \frac{B}{H}C_L(\beta)\right]\frac{w}{U}\gamma_2\right)$$

$$L = \frac{1}{2}\rho B\bar{V}_R^2\left(C_L(\beta) + C_L(\beta)\frac{2Uu}{\bar{V}_R^2}\gamma_3 + \left[C_L'(\beta) - \frac{H}{B}C_D(\beta)\right]\frac{w}{U}\gamma_4\right) \qquad 7.23$$

$$M = \frac{1}{2}\rho B^2\bar{V}_R^2\left(C_M(\beta) + C_M(\beta)\frac{2Uu}{\bar{V}_R^2}\gamma_5 + C_M'(\beta)\frac{w}{U}\gamma_6\right)$$

where γ is the aerodynamic admittance and therefore, terms containing γ are buffet forces and the other terms show the static wind forces. Since there is no data available, the aerodynamic admittance are taken as 1 (Zhang et al. 2013).

Some researchers using data from the wind tunnel tests, provide forces and moment coefficients for vehicle subjected to wind loading (Han et al. 2014). For example, Baker (1991) proposed the following formula of force and moment coefficients for $0 \le \beta \le \frac{\pi}{2}$ (Baker 1991)

$$C_D = -a_1(1 + 2sin3\beta) \qquad 7.24$$

$$C_L = a_2(1 + sin3\beta)$$

$$C_M = a_3\beta^{1.77}$$

a_1 to a_3 are vehicle constants.

As it is explained in chapter 4, Power Spectral Density (PSD) is a widely used tool to model a random process. Wind is turbulent in nature and fluctuates occur in time and space. As a result, wind speed can be regarded as a random process (Simiu 2011).

There are some PSD functions proposed to simulate the wind fluctuations in vertical, lateral and longitudinal directions. Von Karman auto-spectra density equations are as follows

$$\frac{nS_w(n)}{\sigma_w^2} = \frac{4\frac{L_w n}{\bar{V}}}{\left[1 + 70.8\left(\frac{L_w n}{\bar{V}}\right)^2\right]^{5/6}} \quad 7.25$$

$$\frac{nS_u(n)}{\sigma_u^2} = \frac{4\frac{L_u n}{\bar{V}}\left[1 + 755\left(\frac{L_u n}{\bar{V}}\right)^2\right]}{\left[1 + 283\left(\frac{L_u n}{\bar{V}}\right)^2\right]^{11/6}} \quad 7.26$$

where σ_u and σ_v are standard deviations of fluctuations in vertical and longitudinal directions. These values are considered $0.075\bar{u}$ and $0.1\bar{u}$ and $\bar{V}(z)$ is the mean wind speed. The parameters L_w and L_u are length scales of fluctuations.

Other widely used PSD equations in wind engineering were proposed by Kaimal as follows (Simiu 2011)

Lateral wind spectrum

$$\frac{nS_u(f)}{u_*^2} = \frac{200f}{(1 + 50f)^{5/3}} \quad 7.27$$

Longitudinal wind spectrum

$$\frac{nS_w(f)}{u_*^2} = \frac{3.36f}{(1+10f)^{5/3}} \quad 7.28$$

Vertical wind spectrum

$$\frac{nS_v(f)}{u_*^2} = \frac{15f}{(1+10f)^{5/3}} \quad 7.29$$

In which, "u_*" is friction velocity.

$$u_* = \frac{\bar{V}(z)}{2.5ln\frac{z}{z_0}} = \frac{1}{\eta}\overline{u^2(z,t)}^{1/2} \quad 7.30$$

and $f = \frac{nz}{\bar{V}(z)}$

"n" is frequency and "$\bar{V}(z)$" denotes the mean wind speed at elevation "z".

$\overline{u^2(z,t)}^{1/2}$ is the R.M.S (Root Mean Square) of the longitudinal velocity fluctuations.

The values of "$\eta(z_0)$" in the empirical equation 7.30 have been tabulated as follows:

Table 7.1 Values of parameter $\eta(z_0)$ (Simiu 2011)

z_0 (m)	0.005	0.03	0.3	1.00
$\eta(z_0)$	2.55	2.45	2.30	2.20

"z_0" or roughness length is a reference elevation representing surface roughness. ASCE 7-10 Commentary suggested the values of Table 7.2 for different types of surfaces.

Table 7.2 Roughness lengths proposed in ASCE 7-10 Commentary (Simiu 2011)

Type of Surface	Roughness length, ft (m)
Water	0.016-0.03 (0.005-0.01)
Open terrain	0.05-.05 (0.015-0.15)
Urban and suburban terrain, wooded areas	0.5-2.3 (0.15-0.7)

The value of "z_0" is assumed 0.05 m which represents the areas with low vegetation and

isolated obstacles such as tress or buildings.

The procedure of calculating the time-history of wind fluctuations are similar to the process explained in chapter 4. Figure 7.3 shows the PSD function of wind speed fluctuations in longitudinal, vertical and lateral directions for 100 km/hr wind speed.

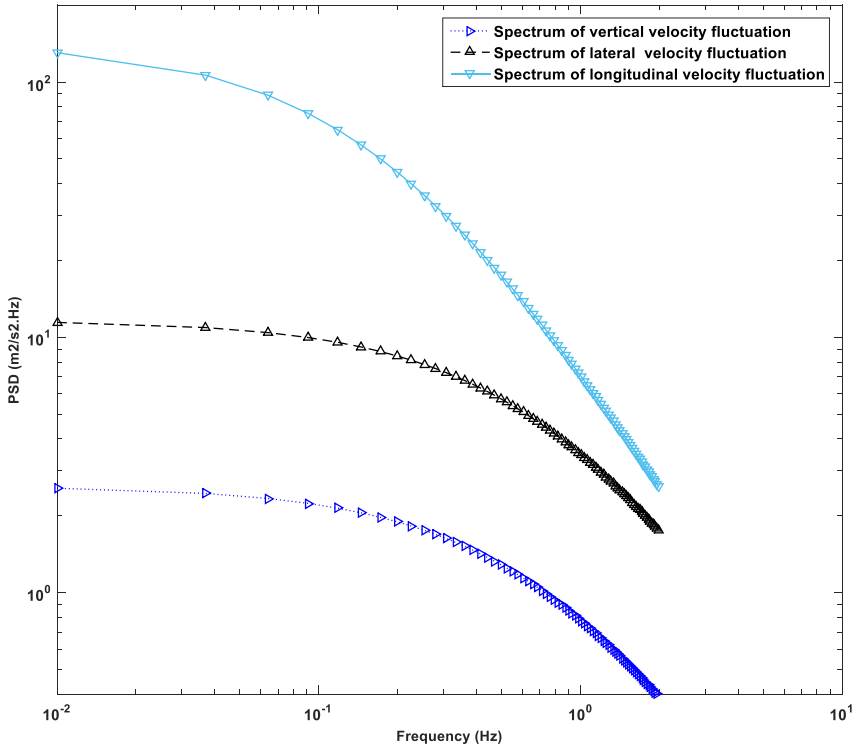

Figure 7.3 PSD functions of wind speed fluctuations in vertical, lateral and longitudinal directions for 100 km/hr wind speed

The procedure of calculating the time-history of wind fluctuations are similar to the process explained in chapter 4.

Figure 7.4 shows the horizontal wind speed fluctuations derived from PSD formula proposed by Kaimal. Figure 7.5 depicts the time history of horizontal wind forces applies on car body and Figure 7.6 demonstrates the horizontal displacements of wheel-rail interface due to applying wind loads. It should be noted that, the results are presented for track class 6 and no other defects are considered in track. Train speed is 100 km/hr and

other parameters are kept constant as mentioned in Table 5.1.

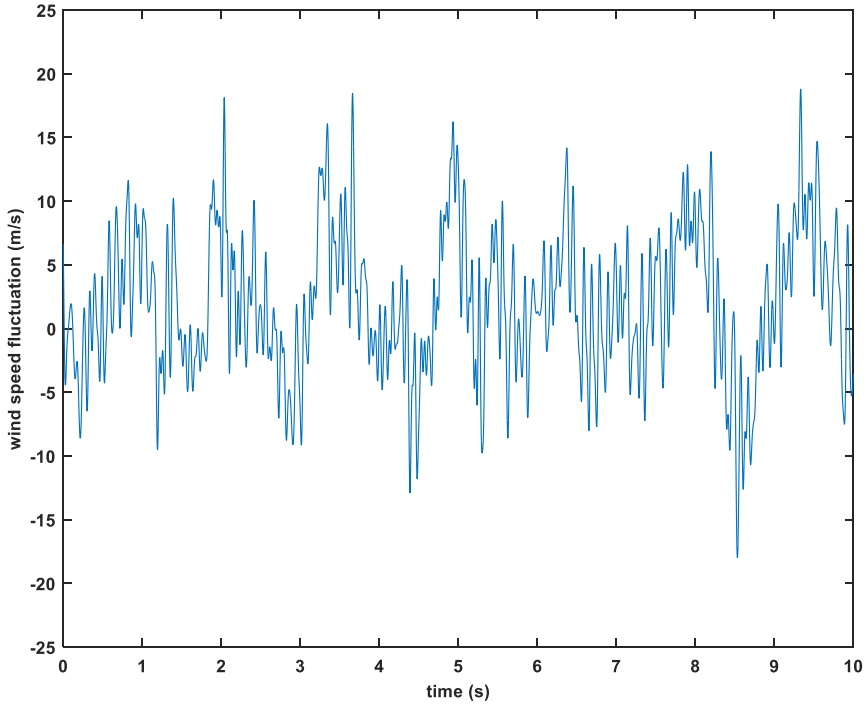

Figure 7.4 Horizontal wind speed fluctuations

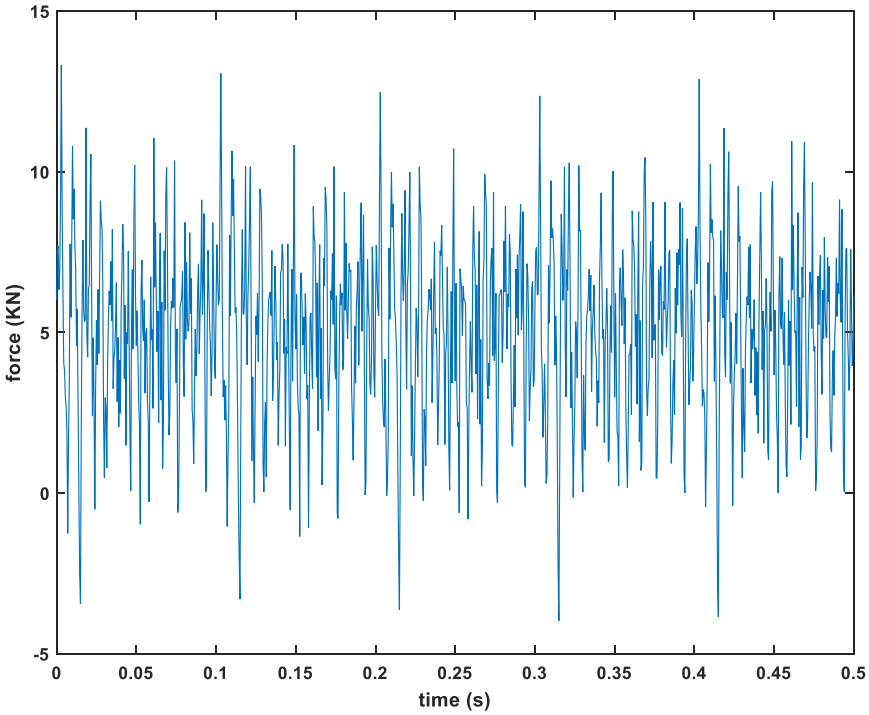

Figure 7.5 Wheel-rail horizontal contact forces

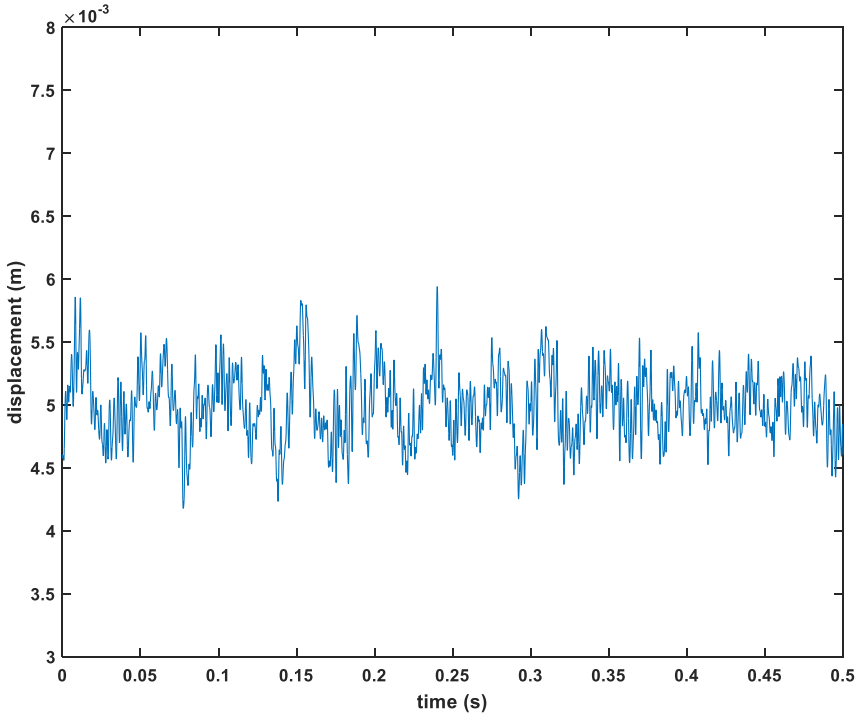

Figure 7.6 Wheel-rail displacements

7. 3. Vehicle stability

This section investigates the vehicle stability under lateral loading due to track defects and wind forces. There are a number of methods to evaluate the stability of vehicles or the risk of overturning. Three most popular criteria are: wheel loading, moment method and intercept method.

Wheel unloading criterion intends to limit the unloading of windward rail as a sign of vehicle overturning (Thomas 2009).

$$\frac{Q_{sta} - Q_{dyn}}{Q_{sta}} \leq 0.9 \qquad 7.31$$

Q_{sta} and Q_{dyn} are static and dynamic wheel loading.

Moment method uses the same idea of retaining structures design which states the equilibrium moment about the outer rail should be greater than the unbalanced moment

due to crosswind forces. The Author could not find any study on safety factors or the minimum ratio of balanced to unbalanced moment in the rail codes.

The third approach or intercept method considers the vertical contact force between wheel and rail to estimate the risk of vehicle overturning. As it is shown in Figure 7.7, the idea is to calculate the resultant contact forces between rail and wheel for both right and left rails and then calculate the difference between the forces. Obviously, the unloading or overloading of rails should be limited to avoid the risk of overturning.

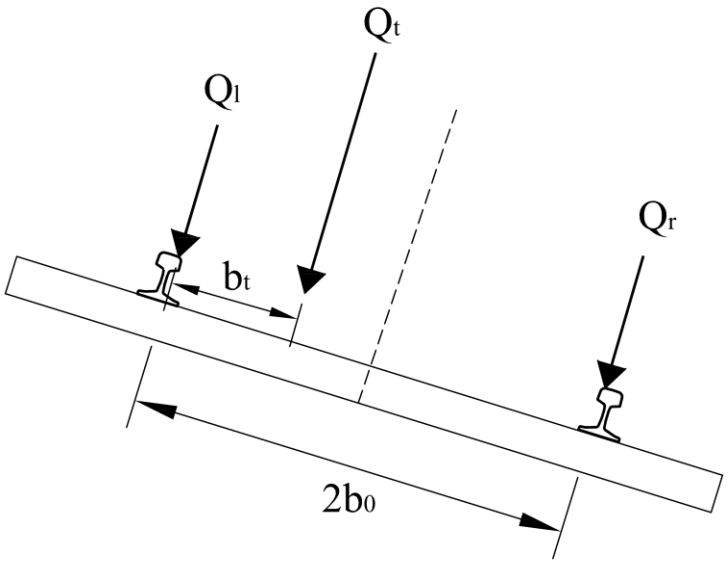

Figure 7.7 Wheel-rail forces used by intercept method to calculate the overturning risk

The risk of vehicle overturning is measured by the following formula

$$n_R = \frac{b_t}{b_0} = \frac{\sum|Q_l - Q_r|}{\sum(Q_l + Q_r)} \qquad 7.32$$

where Q_l and Q_r are vertical forces applied on left and right rail. As the formula implies, in the ideal situation, the resultant vertical force,Q_t, is in the centerline of track and n_R , risk factor, is equal to 1. Acceptable values of "n_R" usually lies bTetween 0.8 and 1. (Thomas 2009)

Table 7.3 shows the parameters used in the stability analysis of the rail vehicle. The coefficients of wind forces are taken from results of a study conducted by Han et al. (Han et al. 2013). Unless it is stated otherwise, the values shown in Table 7.3 will be used in this chapter.

Table 7.3. Parameters used in stability analysis of vehicles

Parameter	Value	Notation
Vehicle Axle Load	15	Ton
Vehicle Speed	200	Km/hr.
Wind Speed	50	Km/hr.
Curve radius	250	m
air density	1.225	Kg/m^3
Height of car body	3	m
Lift Force Coefficient	0.2602	-
Drag Force Coefficient	0.0669	-
Moment Coefficient	-0.0141	-

Figure 7.8 shows the results of an analysis with applying wind forces. The Kaimal PSD formula used to take into account the wind speed fluctuations. The results are presented for two cases of track qualities. As the figure shows, lateral displacements for track class 4 and class 6 vary considerably in time. This is because two random wind forces and forces due to rail irregularities have been applied to the car body. The range of car body lateral displacements for track class 4 is between 0 and 28 mm and for track class 6 is between -7 to 15 mm which shows greater range of displacement for track class 4. The results also suggest that considering the assumptions mentioned earlier, rail irregularities have bigger effects on vehicle lateral displacements. The figure also shows that the mean values of lateral displacements obtained from track class 4 are about 50% more than those of track class 6.

The results for wheel-rail lateral displacements are shown in Figure 7.9. The range of displacements is limited compared to the car body motion. The maximum displacements are 7 mm and 4 mm for track class 4 and class 6, respectively. The mean value of lateral displacements recorded for track class 4 is about 30% more than the displacements obtained from track class 6.

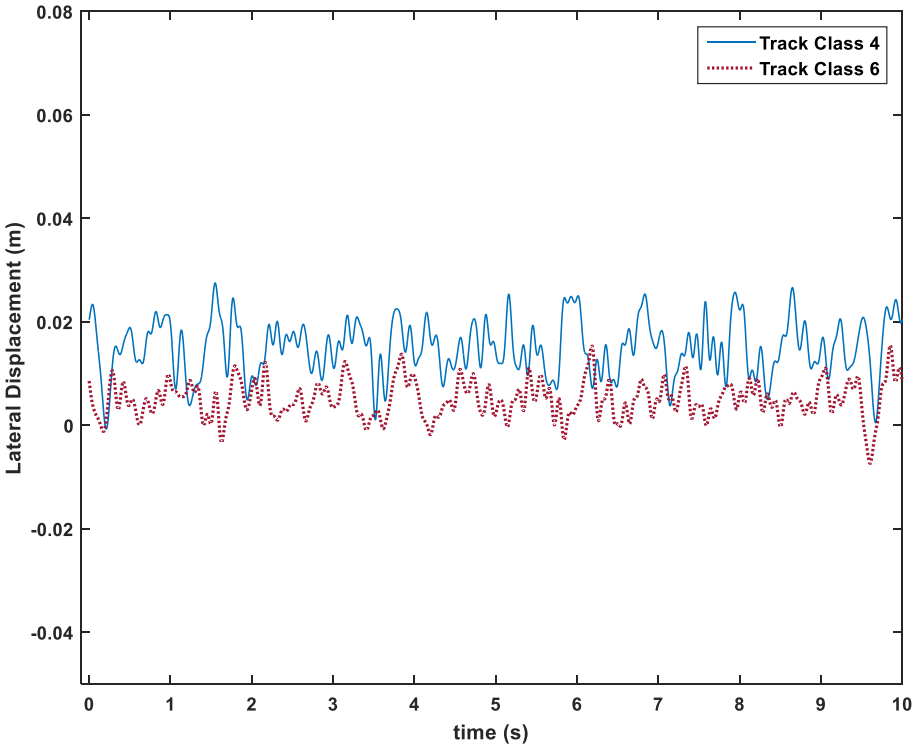

Figure 7.8 Car body lateral displacement for track classes 4 and 6

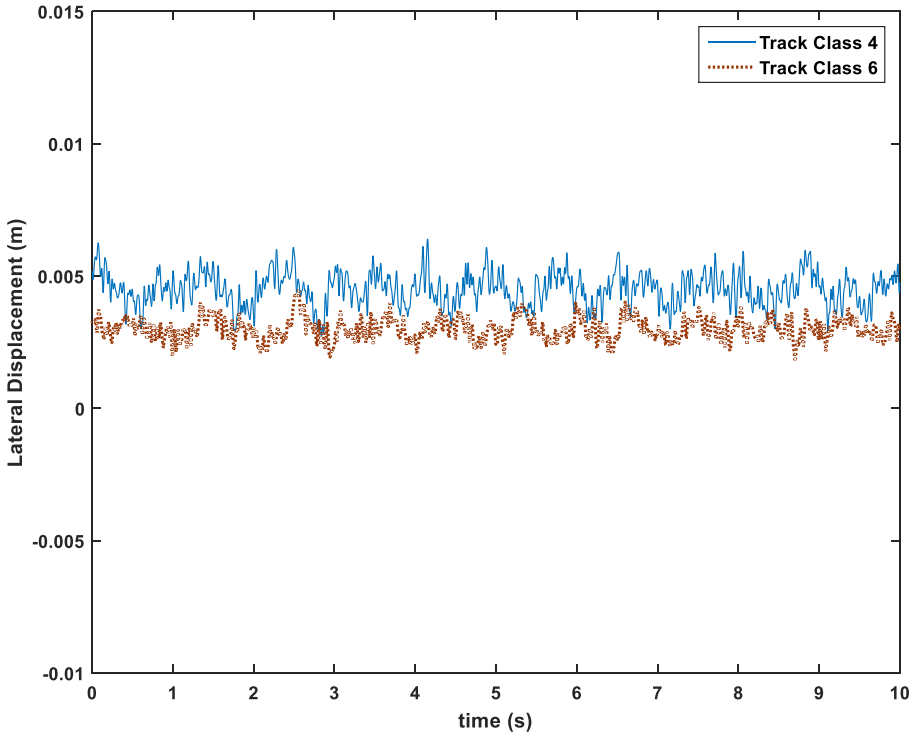

Figure 7.9 Wheel-rail lateral displacement for track classes 4 and 6

7. 3. 1. The effect of wind speed

To consider the influence of wind speed on the risk of vehicle overturning, this parameter has been changed in the range of 0 to 100 km/hr. The value of 0.8 is selected as the critical value for vehicle's risk of overturning. As a result, for each case, the vertical loads on inner and outer rail are calculated and then the criteria in equation 7.32 controls whether or not the vehicle is susceptible to overturning.

The results of analyses have been shown in Figure 7.10 for different wind speeds and track qualities. As a general trend, with increasing wind speed the risk of vehicle overturning increases, but the rate of increasing the risk is changed sharply in the range of 40 to 70 km/hr and after that it increases with lower rate. Another finding from the results is the importance of track quality in reducing the risk of overturning. If the rail quality is improved from class 4 to class 6, the risk of vehicle overturning decreases more than 23%.

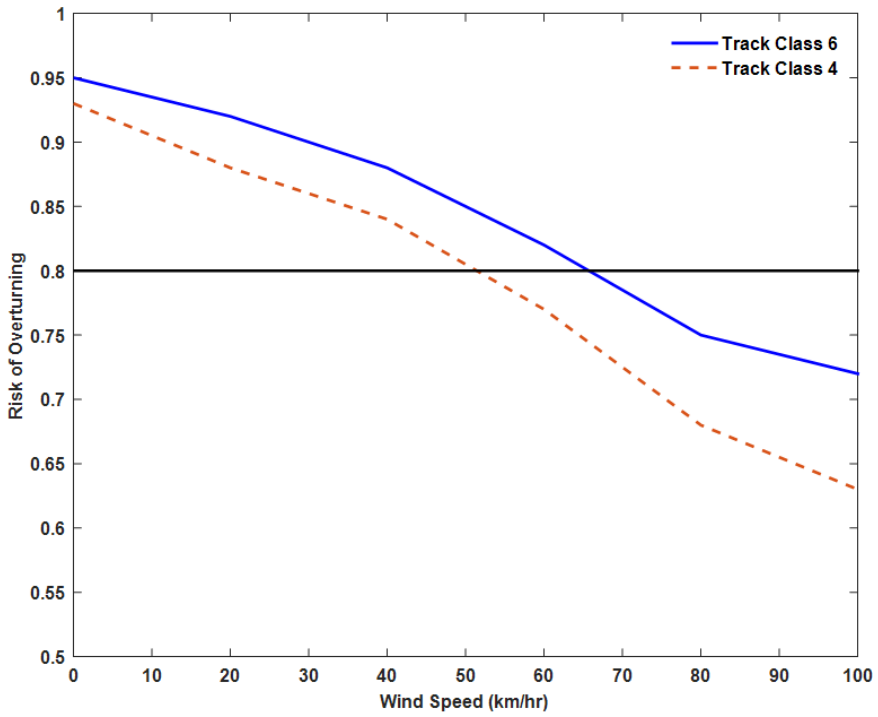

Figure 7.10. Risk of vehicle overturning for different wind speeds and track qualities

Figure 7.11 demonstrates the maximum lateral displacement vs mean wind speed. As it is expected, with increasing speed, the lateral displacement of wheels increases but there is a middle region where displacement increases with highest rate. For speeds lower than 20 km/hr and higher than 60 km/hr the maximum lateral displacements change slowly compared to the middle range.

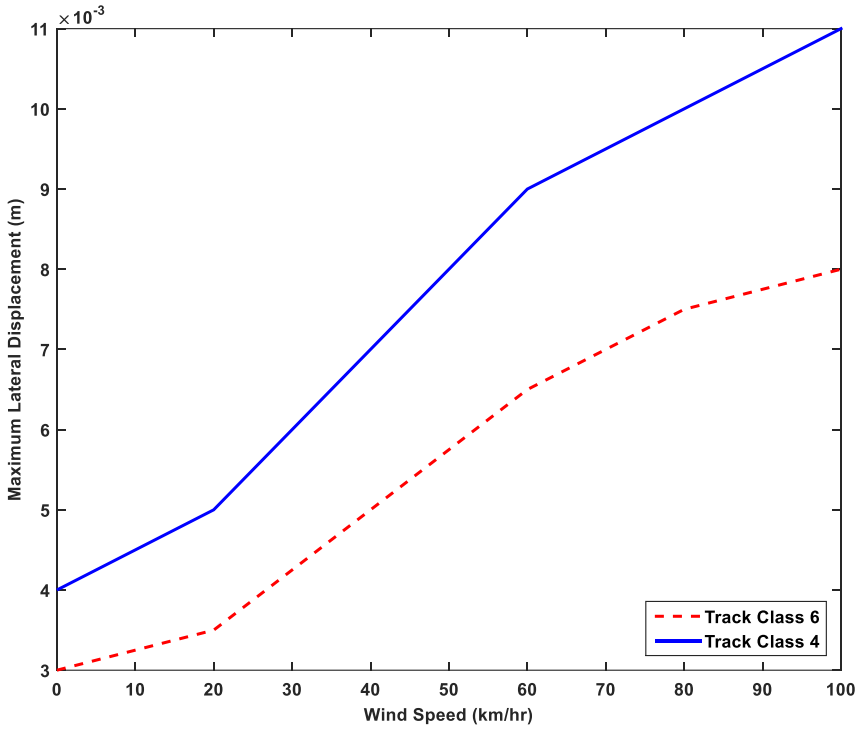

Figure 7.11. the effect of mean wind speed on maximum lateral displacement of wheels

7. 3. 2. The effect of cant deficiency

The effect of super-elevation (cross level or cant) irregularities on track and vehicle was discussed in previous chapters. In many instances, the defect in track geometry is due to track construction errors or subbase settlement. This section discusses the results of cant deficiencies on track response and vehicle overturning risk. Table 7.4 shows the maximum values of super-elevation proposed for California high-speed rail for different train speeds. This section shows the impact of cant deficiency on the vehicle's risk of overturning. Note that for the results derived in this section, it is assumed that the only track defect is cant deficiency and rail surface is in ideal condition.

Table 7.4 the maximum values of superelevation proposed for California high-speed rail (Brinckerhoff Parsons Consulting Co. 2009)

Design Speed		Applied Superelevation					
		Desirable		Maximum		Exceptional	
Mi/hr	Km/hr	inches	mm	inches	mm	inches	mm
<186	<300	4	100	6	150	7	180
>186	>300	4	100	6	150	7	180

The influence of cant deficiency on the risk of overturning depicted in Figure 7.12. It is shown that increasing cant deficiency causes an increase in the unbalanced forces, and therefore, the risk of vehicle overturning increases. The graph is composed of two parts. The slope of vehicle overturning risk in the first part for the cant values less than 20 mm is smaller than that in the second part which the cant values are more than 20 mm. The maximum out of balance super-elevation is 17 mm for track class 4 and train axle load of 15 ton. Other values of track parameters are shown in Table 7.3.

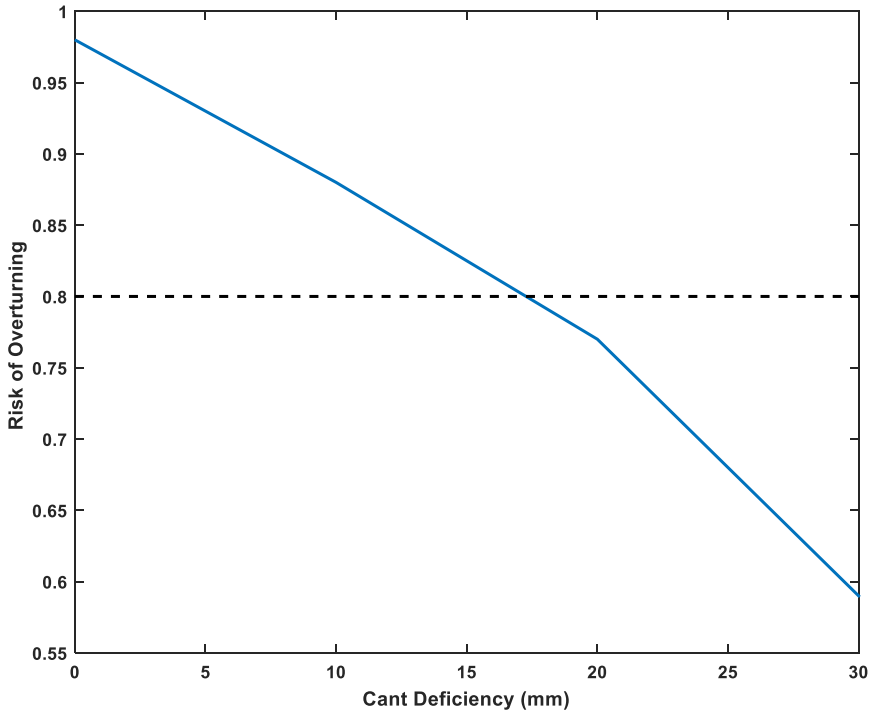

Figure 7.12. the effect of cant deficiency on the vehicle's risk of overturning

Figure 7.13 demonstrates the how cant deficiency affects the ratio of unbalanced force to balanced force. With increasing the deficiency, the unbalanced force increases. Note that the balanced force is constant and as mentioned before depends on vehicle speed and the radius of curve. Vehicle speed and the radius of the curve is assumed 100 km/hr and 200 m, respectively. Since rail is assumed to be in perfect condition and no defect except cant deficiency was considered in the analysis, the ratio of unbalanced to balanced force is almost linear. However, car body undergoes more unbalanced forces compared to wheels. Since car body is heavier than wheel, more centrifugal forces apply on it and so more overturning moment and unbalanced force produce with increasing cant deficiency.

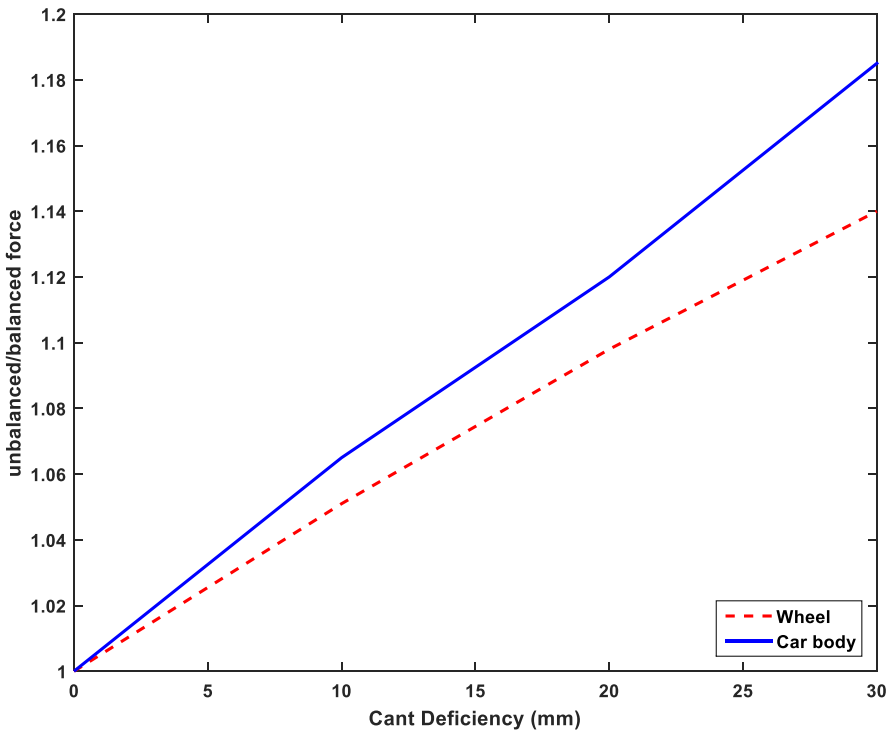

Figure 7.13. the effect of cant deficiency on the ratio of unbalanced to balanced force

7. 4. The effect of wind and rail irregularities on track and vehicle parameters

The aim of this section is to discuss the circumstances that cause unacceptable lateral forces which poses a threat to vehicle safety. As discussed, numerous factors may affect the lateral forces of vehicle. This section considers four parameters of vehicle speed, vehicle axle load, wind mean speed and track quality to discuss the conditions the running of vehicle is not safe. The wind speed selected for simulation lies in category 1 and 2 of Saffir-Simpson hurricane wind scale (Simiu 2011).

Figure 7.14, based on train speed and wind mean speed, shows the area where the allowable and not allowable parameters lie. It is assumed that train axle load is 12 ton. Increasing track quality from class 4 to class 6 causes allowable train speed increases about 9%. It can be observed that with increasing wind speed, the difference between allowable train speeds for two classes of track quality slightly increases. The maximum train speed for track class

6 is limited to 216 km/hr while the allowable speed is limited to 195 km/hr for track class 4. In the analyses, it was assumed that the vehicle is running on a curve with radius 250 m. Figure 7.15 demonstrates the same results for a 15 axle load train. All parameters were kept constant except for wind mean speed, train speed, and rail irregularities. Two important conclusion can be made from this figure; (1) for heavier trains, the track quality has more influence on maximum allowable speed compared to wind forces. In other words, the difference between the results obtained from different track qualities is larger for 15-ton vehicle; (2) as equation 7.23 shows, the wind force is proportional to the square wind speed($F \propto V^2$). For track class 6, the curves show that wind force is the dominant factor on determining safe train speed. However, for track class 4, the curve becomes more linear. This trend can be seen for both heavy and light trains.

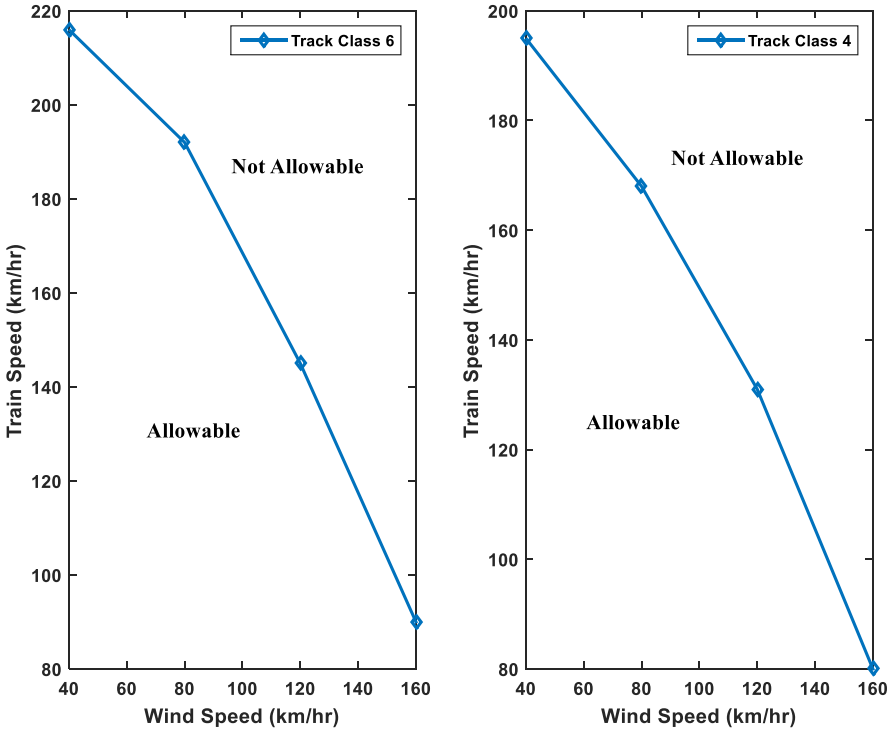

Figure 7.14. The area of allowable and not allowable parameters (left) track class 6, and (right)

track class 4, for 12-ton axle load train

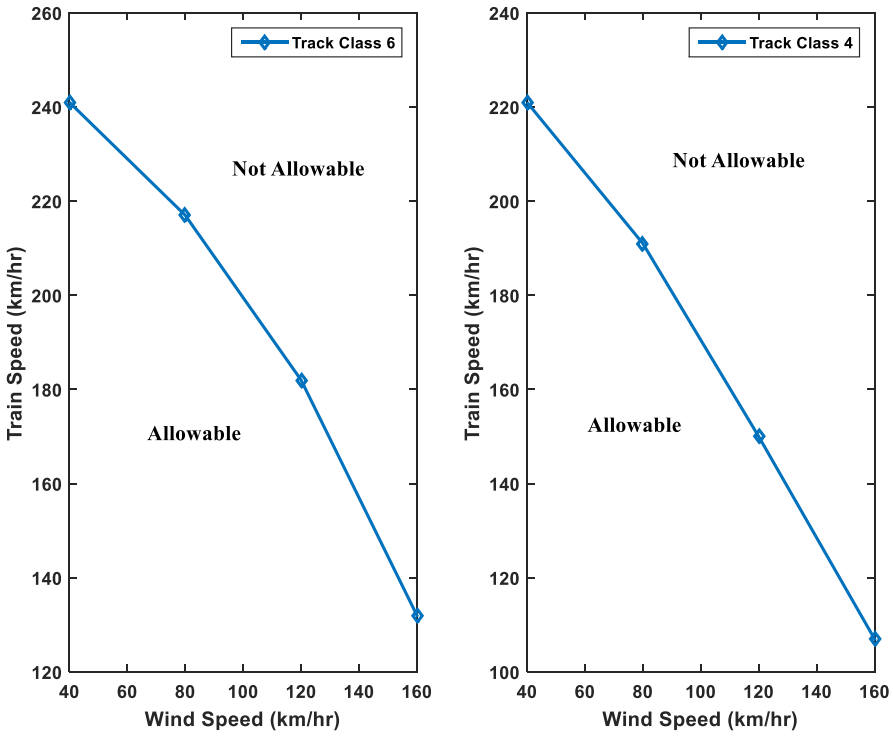

Figure 7.15. The area of allowable and not allowable parameters (left) track class 6, and (right) track class 4, for 15-ton axle load train

8. Summary and Conclusions

A comprehensive study on three-dimensional modeling of railroad track was conducted. Vehicle, track and substructure were modeled, and their interaction was considered in the calculations. The vehicle includes primary and secondary suspension systems and is able to simulate the vertical as well as, lateral displacements. Using the nonlinear Hertz springs, the wheels are connected to three-dimensional Euler-Bernoulli beams as rails. The mass and stiffness of the track substructure was derived from the ballast pyramid model and then the mass, damping and stiffness matrices of the whole system were formed and solved in time domain by the Newmark integration method. The model further developed to include the bridge and curved beams. Rail flaws and wind speed fluctuations as two sources of excitations in vertical and lateral directions were considered, and sensitivity analysis was performed to determine the influential factors to the track impact factor. The results obtained from this research can be divided into three groups as follows.

8. 1. Rail flaws

Rail flaws are the major source of dynamic forces in the track and vehicle. Three important rail flaws are: rail random irregularities, rail corrugation and rail dip and raise. In this study, their parameters were investigated under different operating conditions. Rail and vehicle impact factors were used to assess the influence of each parameter on track and vehicle dynamics. The results of analyses led to the following conclusions:

1- Rail random irregularities significantly affect rail dynamic forces. The amount of dynamic forces is a function of track quality and train speed. The impact factor generated from track class 4 is much larger than that due to track class 6, especially for high-speed trains. The results show that increasing vehicle speed does not

necessarily increase impact factors. It is especially valid for bogie and car body impact factors that the impact factor reduces when the train speed increases to 250 km/hr.

2- The joint in the railroad track causes an increase in rail impact factor, but in case of no defects, the train speed does not have considerable influence on the rail impact factors. However, a dip or a raise in the rail joint has a great influence on dynamic forces. For dipped rail, with increasing speed, impact factor increases from 18% to 62% when vehicle speed increases from 50 to 200 km/hr.

3- The depth and length of the rail joint raise or dip are important factors on the dynamic forces from the vehicle. The results of the study indicate that for defect lengths shorter than 0.3 m there is a large difference of the impact factors between rail joint dip and raise but with increasing the defect length, the difference decreases.

4- Among the rail flaws considered in this research, corrugation has the biggest influence on rail impact factor. Based on the results of the study, increasing corrugation depth generates a large impact factor. As it is expected, shorter wavelength causes greater impact factor.

8. 2. Stability of the vehicle

The stability of vehicles under lateral forces was investigated and the effect of different factors on track and vehicle lateral displacements and forces were determined. For this purpose, first, the equations of motions of curved beam were incorporated into the numerical model of the vehicle-track interactions, and then the wind forces considering wind speed fluctuations were determined. Based on the intercept method, used to assess

the risk of vehicle overturning, the following conclusions were made:

1- Higher wind speeds raise the risk of vehicle overturning and as a general trend, with increasing wind speed the rate of increasing in lateral forces increases. It is also concluded that track irregularities have more influence on the vehicle's risk of overturning for higher wind speeds.

2- Cant deficiency causes an unbalanced force that may pose a threat to vehicle stability. Based on the results, cant deficiency has the biggest effect on car body. The results indicate that there is a point at which the rate of vehicle risk of overturning increases by increasing cant deficiency.

3- Parameters of vehicle speed, vehicle axle load, wind mean speed, and track quality were studied to evaluate safe conditions of the running vehicle. Increasing track quality from class 4 to class 6 causes the allowable train speed to increase about 9%. It can be observed that with increasing wind speed, the difference between allowable train speeds for two classes of track quality slightly increases. The results show that for heavier trains, the track quality has more impact on maximum allowable speed compared to wind forces. For track class 4, the relation between wind speed and allowable train speed becomes more linear compared to track class 6.

8. 3. Suggestions for future work

As it is mentioned, railroad track dynamics is a complicated problem with numerous degrees of freedom, and all researchers disregarded some aspects of the problem to make it solvable. In this study, in order to produce precise results a detailed model of vehicle and track was considered. However, for conducting a comprehensive study, considering other track types and vehicle conditions, the following are suggested for the future work.

1- The focus of this study was on high-speed rail track. To investigate the response of other types of railroad track to dynamic excitations, data from experiments are required. Since the accuracy of the results completely depends on the choice of correct values for the vehicle, track and substructure parameters, the behavior of non-conventional tracks, such as slab tracks, which are widely used in urban and high-speed tracks, also need to be investigated. The double beam model used in this research provides a good estimate of the slab track response. However, more research on the effect of different track and vehicle parameters on slab track response is essential.

2- Few attempts have been made to understand the behavior of rail vehicles under wind forces. More wind tunnel tests are necessary to provide accurate aerodynamic data for numerical modeling. The reliable data obtained from the tunnel tests that can be used in numerical modeling is very limited, and it is very hard to find proper values for some parameters, such as aerodynamic admittance, vehicle (shape) parameters and the effect of changes in the direction of vehicle, as well as the effect of curvature on wind forces.

3- Investigation on the material properties of the track is also required to have a better understanding of the track behavior. It is well known that the behavior of the fastening system, ballast and track substructure becomes nonlinear with increasing the accumulative loads from vehicles. The author could not find any well-documented experiments or material models that can be utilized in numerical simulations. As a result, except for Hertz nonlinear springs between rails and

wheels, the behavior of other track parts is assumed to be linear. Using more accurate track and subgrade models, leads to more reliable results.

REFERENCES

Ahlbeck, D.R., Meacham, H.C. & Prause, R.H., 1978. The development of analytical models for railroad track dynamics. In A. D. Kerr, ed. *Railroad Track Mechanics & Technology*. Oxford: Pergamon Press.

Akin, J.E. & Mofid, M., 1989. Numerical solution for response of beams with moving mass. *Journal of Structural Engineering*, 115(1), pp.120–131.

American Railway Engineering and Maintenance-of-Way Association, 2010. *Manual for Railway Engineering, Vol.1, Track*,

Andersen, L. & Jones, C.J.C., 2006. Coupled boundary and finite element analysis of vibration from railway tunnels-a comparison of two- and three-dimensional models. *Journal of Sound and Vibration*, 293(3–5), pp.611–625.

Baker, C.J., 1991. Ground vehicles in high cross winds part I: Steady aerodynamic forces. *Journal of Fluids and Structures*, 5(1), pp.69–90.

Biggs, J.M., 1964. *Introduction to Structural Dynamics*, New York: McGraw-Hill.

Boresi, A.P. & Schmidt, R.J., 2003. *Advanced Mechanics of Materials* 6th Editio., New York: John Wiley & Sons.

Brien, J. & Rizos, D.C., 2005. A 3D BEM-FEM methodology for simulation of high speed train induced vibrations. *Soil Dynamics and Earthquake Engineering*, 25(4), pp.289–301.

Brinckerhoff Parsons Consulting Co., 2009. *TECHNICAL MEMORANDUM: Alignment Design Standards for High-Speed Train Operation*, California High-Speed Train Project.

Carl E. Hanson; David A. Towers; and Lance D. Meister, 2006. Transit Noise and Vibration Impact Assessment -FTA Federal Transit Administration. , (May), pp.1–261.

Carter F.W, 1926. On the action of a locomotive driving wheel. *Proceedings of the Royal Society of London A*, (112).

Chopra, A.K., 2011. *Dynamics of Structures* 4th ed., Prentice-Hall. Available at: 0132858037.

Connolly, D.P. et al., 2014. Assessment of railway vibrations using an efficient scoping model. *Soil Dynamics and Earthquake Engineering*, 58, pp.37–47. Available at: http://dx.doi.org/10.1016/j.soildyn.2013.12.003.

Connolly, D.P. et al., 2015. Benchmarking railway vibrations – Track, vehicle, ground and building effects. *Construction and Building Materials*, 92, pp.64–81. Available at: http://linkinghub.elsevier.com/retrieve/pii/S0950061814007661.

Dassault Systèmes Simulia Corp, 2012. *ABAQUS 6.12, user manual*,

Emil Simiu, 2011. *design of buildings for wind, a guide for ASCE 7-10 Standard users and designers of special structures* 2nd Editio., John Wiley & Sons, INC.

Esmaeili, M., Sadeghi, J. & Fesharaki, M., 2014. Vehicle dynamic interaction with railway track embankment. *Proceedings of the Institution of Civil Engineers - Transport*, 167(1), pp.15–26.

Esveld, C., 2001. *Modern Railway Track* 2nd ed., MRT Publications.

Frýba, L., 1996. *Dynamics of Railway Bridges* 2nd ed., Thomas Telford.

Frýba, L., 1999. *Vibration of Solid and Structures under Moving Loads*, Thomas Telford.

Fu, Q. & Zheng, C., 2014. Three-dimensional dynamic analyses of track-embankment-ground system subjected to high speed train loads. *The Scientific World Journal*, 2014.

Gupta, S. et al., 2007. A comparison of two numerical models for the prediction of vibrations from underground railway traffic. *Soil Dynamics and Earthquake Engineering*, 27(7), pp.608–624.

Hall, L., 2003. Simulations and analyses of train-induced ground vibrations in finite element models. *Soil Dynamics and Earthquake Engineering*, 23(5), pp.403–413.

Hamid, A. et al., 1983. *Analytical Descriptions of Track Geometry Variations*, Springfield, VA.

Han, Y. et al., 2014. Effects of aerodynamic parameters on the dynamic responses of road vehicles and bridges under cross winds. *Journal of Wind Engineering and Industrial Aerodynamics*, 134(April 2015), pp.78–95. Available at: http://dx.doi.org/10.1016/j.jweia.2014.08.013.

Han, Y., Hu, J. & Cai, C.S., 2013. Experimental and numerical studies of aerodynamic forces on vehicles and bridges. , 17(2), pp.163–184.

Hussein, M.F.M. & Hunt, H.E.M., 2006. Modeling of floating-slab tracks with continuous slabs under oscillating moving loads. *Journal of Sound and Vibration*, 297(1–2), pp.37–54.

International Union of Railways, 2002. Rail defects, UIC code 712R.

Johansson, C., 2013. *Simplified dynamic analysis of railway bridges under high-speed trains*. KTH School of ABE.

Kalker, J.J., 1991. Wheel-Rail Rolling Contact Theory. *Journal of Wear*, 8(No. 4), pp.243--261.

Kang, X., Liu, x B. & Li, H.Y., 2014. PSD of ballastless track irregularities of high-speed railway. *SCIENTIA SINICA Technologica*, 44, pp.687–696. Available at: http://engine.scichina.com/doi/10.1360/N092014-00088.

Kargarnovin, M.H. & Younesian, D., 2004. Dynamics of Timoshenko beams on Pasternak foundation under moving load. *Mechanics Research Communications*, 31(6), pp.713–723.

Katou, M. et al., 2008. Numerical simulation study of ground vibrations using forces from wheels of a running high-speed train. *Journal of Sound and Vibration*, 318(4–5), pp.830–849.

Kerr, A., 2003. *Fundamentals of railway track engineering*, Simmons Boardman Pub Co.

Krylov, V. ed., 2001. *Trains, Noise and Vibration from High-Speed*, Thomas Telford Publishing.

Krylov, V. V., 1995. Generation of ground vibrations by superfast trains. *Applied Acoustics*, 44(2), pp.149–164.

Kuo, C.M., Huang, C.H. & Chen, Y.Y., 2008. Vibration characteristics of floating slab track. *Journal of Sound and Vibration*, 317(3–5), pp.1017–1034.

Lei, X. & Noda, N.A., 2002. Analyses of Dynamic Response of Vehicle and Track Coupling System With Random Irregularity of Track Vertical Profile. , 258(May), pp.147–165.

Li, Y. et al., 2005. Dynamics of wind-rail vehicle-bridge systems. *Journal of Wind Engineering and Industrial Aerodynamics*, 93(6), pp.483–507.

Liu, X., Saat, M.R. & Barkan, C.P.L., 2012. Analysis of causes of major train derailment and their effect on accident rates. *Transportation Research Record*, 2289(2289), pp.154–163. Available at: http://www.scopus.com/inward/record.url?eid=2-s2.0-84869825050&partnerID=40&md5=22ee5a76acd96e168dc20a39023482fa.

Lombaert, G. et al., 2006. The control of ground-borne vibrations from railway traffic by means of continuous floating slabs. *Journal of Sound and Vibration*, 297(3–5), pp.946–961.

Lou, P., 2005. A vehicle-track-bridge interaction element considering vehicle's pitching effect. *Finite Elements in Analysis and Design*, 41(4), pp.397–427.

Lou, P. et al., 2006. Finite-element analysis of discretely supported rail subjected to multiple moving concentrated forces. *Journal of rail and rapid transit*, 220(3), pp.305–315.

Lou, P. & Zeng, Q., 2005. Formulation of equations of motion of finite element form for vehicle–track–bridge interaction system with two types of vehicle model. *International Journal for Numerical Methods in Engineering*, 62(3), pp.435–474.

Lou, P. & Zeng, Q.Y., 2006. Vertical vehicle-track coupling element. *Proceedings of the Institution of Mechanical Engineers Part F-Journal of Rail and Rapid Transit*, 220(3), pp.293–304.

Naeimi, M. et al., 2015. Influence of uneven rail irregularities on the dynamic response of the railway track using a three-dimensional model of the vehicle–track system. *Vehicle System Dynamics*, 53(1), pp.88–111.

Pesterev, A. V., Yang, B., Bergman, L. A., and Tan, C.A., 2001. Response of elastic continuum carrying multiple moving oscillators. , 127(March), pp.260–265.

Rizos, D.C. & Wang, Z., 2002. Coupled BEM-FEM solutions for direct time domain soil-structure interaction analysis. *Engineering Analysis with Boundary Elements*, 26(10), pp.877–888.

Sadeghi, J., 2009. *Fundamentals of analysis and design of railway ballasted track*, Tehran, Iran: IUST publication.

Sadeghi, J., Fesharaki, M. & Khajehdezfuly, A., 2015. Influences of train speed and axle loads on life cycle of rail fastening clips. *Transactions of the Canadian Society for Mechanical Engineering*, 39(1), pp.1–11.

Steenbergen, M.J.M.M. & Esveld, C., 2006. Relation between the geometry of rail welds and the dynamic wheel - rail response: numerical simulations for measured welds. *Proceedings of the Institution of Mechanical Engineers, Part F: Journal of Rail and Rapid Transit*, 220(4), pp.409–423. Available at: http://pif.sagepub.com/lookup/doi/10.1243/0954409JRRT87.

Steenbergen, M.J.M.M. & Metrikine, A. V., 2007. The effect of the interface conditions on the dynamic response of a beam on a half-space to a moving load. *European Journal of Mechanics, A/Solids*, 26(1), pp.33–54.

Straszak, A. & Tuch, R., 1977. The Shinkansen High-Speed Rail Network of Japan. In *IIASA Conference*. Pergamon Press.

Sun, Y.Q. & Dhanasekar, M., 2002. A dynamic model for the vertical interaction of the rail track and wagon system. *International Journal of Solids and Structures*, 39(5), pp.1337–1359.

Tarighi, A. & Wang, T., 2015. Dynamic Modeling of Long Combination Vehicles. *International Journal of Sciences: Basic and Applied Research*, 4531, pp.330–345.

Thomas, D., 2009. *Lateral Stability of High-Speed Trains at Unsteady Crosswind*. KTH Department of Aeronautical and Vehicle Engineering, Division of Rail Vehicles.

Thompson, D.J., 1990. *Wheel-rail noise: Theoretical modeling of the generation of vibrations*. University of Southampton.

Thornely-Taylor, R.M., 2004. The Prediction Of Vibration, Groundborne And Structure-Radiated Noise From Railways Using Finite Difference Methods – Part I - Theory. *Proceedings of the Institute of Acoustics*, 26, pp.1–11.

Vasilev, G. et al., 2015. Soil-structure interaction using BEM-FEM coupling through ANSYS software package. *Soil Dynamics and Earthquake Engineering*, 70, pp.104–117. Available at: http://dx.doi.org/10.1016/j.soildyn.2014.12.007.

Wang, T.-L., 1984. *Impact and Fatigue in Open Deck Steel Truss and Ballasted Prestressed Concrete Railway Bridges*. PhD dissertation, Illinois Institute of Technology.

Wang, T.L., Garg, V.K. & Chu, K.H., 1991. Railway bridge/vehicle interaction studies with new vehicle model. *Journal of Structural Engineering*, 117(7), pp.2099–2116.

Wu, T.X. & Thompson, D.J., 2003. On the impact noise generation due to a wheel passing over rail joints. *Journal of Sound and Vibration*, 267(3), pp.485–496.

Wu, T.X. & Thompson, D.J., 2002. Wheel/Rail Non-Linear Interaction with Coupling between Vertical and Lateral Directions. *International Journal of Vehicle Mechanics and Mobility*, 41(1), pp.27–49.

Y.C.Yang, 1986. *Random vibration of structures* 1st ed., John Willey & Sons.

Yang, Y. & Kuo, S., 1987. Effect of Curvature on Stability of Curved Beams. *Journal of Structural Engineering*, 113(6), pp.1185–1202.

Yoo, C.H., Kang, Y.J. & Davison, J.S., 1996. Buckling analysis of curved beams by finite-element discretization. *Journal of Engineering Mechanics*, 122(8), pp.762–770.

Younesian, D. & Kargarnovin, M.H., 2009. Response of the beams on random Pasternak foundations subjected to harmonic moving loads. *Journal of Mechanical Science and Technology*, 23(11), pp.3013–3023. Available at: http://link.springer.com/10.1007/s12206-009-0816-3.

Younesian, D. & Sadri, M., 2012. Effects of the trench geometry on vibration mitigation level in high-speed railway tracks. *Journal of Mechanical Science and Technology*, 26(8), pp.2469–2476.

Zhai, W.M., Wang, K.Y. & Lin, J.H., 2004. Modeling and experiment of railway ballast vibrations. *Journal of Sound and Vibration*, 270(4–5), pp.673–683.

Zhang, Q.L., Vrouwenvelder, A. & Wardenier, J., 2001. Numerical simulation of train-bridge interactive dynamics. *Computers and Structures*, 79(10), pp.1059–1075.

Zhang, T., Xia, H. & Guo, W.W., 2013. Analysis on running safety of train on bridge with wind barriers subjected to cross wind. *Wind and Structures, An International Journal*, 17(2), pp.203–225.

Zhao, X. & Li, Z., 2011. The solution of frictional wheel-rail rolling contact with a 3D transient finite element model: Validation and error analysis. *Wear*, 271(1–2), pp.444–452. Available at: http://dx.doi.org/10.1016/j.wear.2010.10.007.

VITA

MOHAMMAD FESHARAKI

Born, Tehran, Iran

2001-2005	B.Sc., Railway Track and Structures Engineering Iran University of Science and Technology Tehran, Iran
2006-2009	M.SC., Railway Track Engineering Iran University of Science and Technology Tehran, Iran
2014-2017	Ph.D., Structural Engineering Florida International University Miami, FL

PUBLICATIONS AND PRESENTATIONS

M. Fesharaki, T.L. Wang, "*The Effect of Rail Defects on Track Impact Factors*", Civil Engineering Journal, Vol. 2, Issue 9, 458-473, 2016.

M. Fesharaki, "*An Investigation on the Effect of Rail Corrugation on Track Response*", International Journal of Science and Engineering Applications, Volume 5 Issue 7, 2016.

J. Sadeghi, M. Fesharaki and A. Khajehdezfuly, “ Influences of Train Speed and Axle Loads on the Life Cycle of Rail Fastening Clips”, Transactions of the Canadian Society for Mechanical Engineering, Vol. 39, No. 1, 2015

J. Sadeghi, M. Fesharaki. "*Influence of Nonlinearity of Track Support System on Railway Track Dynamics*", International Journal of Structural Stability and Dynamics, Vol.13, No.1, 2013.

M. Esmaeili, M. Fesharaki, "*Vehicle Dynamic Interaction with Railway Track Embankment*", Proceedings of the Institution of Civil Engineers journal Transport, Vol.166, Issue 4, November 2013, DOI: 10.1680/tran.11.00024.

M. Fesharaki and A. Hamedi,” *Effects of High-Speed Rail substructure on ground-borne vibrations*”, ASCE Florida Section Annual Conference Proceedings, 38-47, 2016

M. Fesharaki, Wang, Ton.Lo, “*The Impact of Rail Defects on Track and Vehicle Response*” Railway Infrastructure & Vehicle Inspection Tech Conference, University of Illinois at Urbana Champaign, IL, 20-21 June 2017